Doctoral Thesis

New Perspective of Metal-Organic Frameworks for Advanced Molecular Separation and Sensing.

Jin Yeong Kim

Department of Chemistry

Graduate School of UNIST

2019

New Perspective of Metal-Organic Frameworks for Advanced Molecular Separation and Sensing.

Jin Yeong Kim

Department of Chemistry

Graduate School of UNIST

New Perspective of Metal-Organic Frameworks for Advanced Molecular Separation and Sensing.

A dissertation
submitted to the Graduate School of UNIST
in partial fulfillment of the
requirements for the degree of
Doctor of Philosophy

Jin Yeong Kim

11/21/2018

Approved by

Advisor
Hoi Ri Moon

New Perspective of Metal-Organic Frameworks for Advanced Molecular Separation and Sensing.

Jin Yeong Kim

This certifies that the dissertation of Jin Yeong Kim is approved.

11 / 21 / 2018

Advisor: Hoi Ri Moon

Myoung Soo Lah

Jong-Beom Baek

Hyunchul Oh

Nak Cheon Jeong

Abstract

Metal-organic frameworks (MOFs), with high porosity and high structural diversity, have attracted attention in applications requiring identification of target molecules and have triggered many studies on separation and sensing. Despite the various promising findings, most of well-designed multi-functional MOF systems practically useless due to the many barriers to practical use, such as poor performance in operating environments, stability issues, and processability problems. In this thesis, I report a series of separation of hydrogen isotope and sensing application studies based on various existing MOF system through a new perspective, which optimizes the performance and overcomes a variety of stability and processing issues required for the real-world application.

The isolation of deuterium from physico-chemically almost identical isotopic mixture is a seminal challenge in modern separation technology. One of our approach toward the development of a highly effective hydrogen isotope separation system is exploiting the dynamic pore aperture change during breathing propagation in flexible MOF system. For that, MIL-53(Al) is chosen for host material which has flexible 1D channel response to hydrogen adsorption as well as offer a large storage capacity through *lp* phase. This study shows that the selectivity for D_2 over H_2 is strongly related to the state of the pore structure of MIL-53(Al). Above all, breathing phenomenon can be systematically tuned by exposure temperature, pressure, and time, resulting in the highest selectivity ($S_{D2/H2}$ = 13.6) with high separation capacity of 2.9 mmol g^{-1}. Furthermore, we report a highly effective hydrogen isotope separation system based on metal-organic frameworks (MOFs) having the highest reported separation factor ($S_{D2/H2}$) as high as ~26 at 77 K by maximizing synergistic effects of the chemical affinity quantum sieving (CAQS) and kinetic quantum sieving (KQS). For this purpose, MOF-74-Ni, having a high density of strong adsorption sites, which provide the CAQS effect, was chosen as a host material. Simultaneously, imidazole molecules are introduced into the 1D channel of MOF-74-Ni as a diffusion barrier, effectively reducing the aperture size and repeatedly blocking H_2 diffusion, resulting in the KQS effect. To the best of our knowledge, this work is not only the first attempt to implement two quantum sieving effects, KQS and CAQS, in one system but also provides experimental validation of this system as a practical strategy for industrial applications.

Practical sensing applications of metal-organic frameworks (MOFs) have been hampered by processability and sensitivity to moisture and chemicals. Herein, we report a new class of MOF inks prepared by suspending various MOFs (HKUST-1, MIL-101(Cr), ZIF-67, ZIF-8, and MOF-74(Ni)) in a water-repellent, photocurable fluoropolymer (PFPE) up to 90 wt%. These MOF inks enables to form chemical- and moisture-resistant coatings, patterns and 3D structures using typical processing techniques such as spray coating, pen writing, stencil printing, and moulding at room temperature. Upon UV-curing, the hydrophobic PFPE matrix efficiently blocks water permeation but allows accessibility of chemicals into MOF pores, thereby freeing the MOF to perform its unique function. Moreover, two

types of MOF inks containing $Zn_2(bdc)_2(dpNDI)$ and $Tb_{0.99}Eu_{0.01}(hfa)_3(dpbp)$ demonstrated a water-tolerant chemosensor for volatile organic compounds (VOCs) in water and a chemical-resistant thermosensor for visualizing temperature image, respectively. This approach would open up innumerable opportunities for those MOFs that are otherwise dormant.

Contents

Abstract

Chapter I. General Introduction

References 5

Chapter II. Isotope Separation in Metal-Organic Frameworks

References 11

2.1 Fundamentals 13

2.1.1 Kinetic Qunatum Sieving 13

2.1.2 Chemical Affinity Quantum Sieving 14

2.1.3 Analytical Techniques for Isotopes Separation 15

2.1.4 Refereneces 21

2.2 Previous Researches of Hydrogen Isotope Separation in MOFs and COFs 23

2.2.1 Simulations 23

2.2.2 Framework with Rigid Structure 24

2.2.3 Local Flexibility and Breathing Effect 26

2.2.4 Unsaturated Open Metal Site 28

2.2.5 Refereneces 32

2.3 Selective Hydrogen Isotope Separation via Breathing Transition in MIL-53(Al) 35

2.3.1 Introduction 35

2.3.2 Experimental Section 37

2.3.3 Results and Discussion 39

2.3.4 Conclusion 49

2.3.5 References 50

2.4 Exploiting Diffusion Barrier and Chemical Affinity of Metal-Organic Frameworks for Efficient Hydrogen Isotope Separation 53

2.4.1 Introduction 53

2.4.2 Experimental Section 55

2.4.3 Results and Discussion 59

2.4.4 Conclusion 79

2.4.5 References 80

Chapter III. Versatile Processing of Metal-Organic Framework-Fluoropolymer Composite Inks with Chemical-Resistance and Sensor Applications

3.1 Introduction 83

3.2 Experimental Section 85

3.3 Results and Discussion 90

3.4 Conclusion 112

3.5 References 113

Appendix I. Hetero Core-Shell Metal-Organic Frameworks

1 Introduction 117

2 Experimental Section 119

3 Results and Discussion 121

4 Conclusion 132

5 References 133

Acknowledgements

List of Figures

Chapter I

Figure 1.1 Schematic illustration of MOFs for separation and sensing applications.

Figure 1.2 (a) Schematic images of swichable membrane separation. (b) The crystal structure of photoswitchable $Cu_2(AzoBPDC)_2(AzoBiPyB)$. (c) Tunnig H_2:CO_2 separation factor by adjusting the cis:trans azobenzene ratio. (e) Schematic image of melecular decoding. (e) The crystal structure of Zn_2BDC_2dpNDI in teh view along the main axes of bdc. (f) The resulting luminescence of Zn_2BDC_2dpNDI, suspended in various VOC solvent.

Chapter II

Figure 2.1 Timeline for the advances in hydrogen isotope separation in confined nanoporous spaces.

Figure 2.1.1 (a) Potential energy, V, and transverse motion energy levels, E_i, for a molecule in a channel with d-σ~λ (qualitative picture). (b) Behavior of well depth ε and zero point energy (E_0) of isotopes as functions of channel diameter d. Regions 1, 2, 3, and 4 can be attributed to classical geometrical potential (Regions 1, 2, and 4) and quantum sieving (Regions 3_{H2} and 3_{D2}), respectively.

Figure 2.1.2 Difference potential well depths that represent the strength of the binding energy. The red and blue marks indicate ZPEs of isotopes H_2 and D_2, respectively.

Figure 2.1.3 (a) Schematic diagram of advanced TDS and **(**b) experimental setup for ACTDS. c) Schematic diagram of breakthrough apparatus.

Figure 2.2.1 (a) Snapshot of Zn-TBIP with adsorbed T_2 and H_2 at 10^{-19} bar and 20 K and (b) zero pressure selectivity of MOFs as a function of temperature. (c) Snapshot of CPL-1 with adsorbed D_2 and H_2 at 0.01 Mpa and 77 K and (d) selectivity of D_2 over H_2 of nine channel-type MOFs as a function of the quantum effective pore size of MOFs at 0.001 MPa and 77 K.

Figure 2.2.2 (a) Schematic view of M′MOF 1 and H_2 and D_2 adsorption kinetic profiles of M'MOF for pressure increment 0.2-0.4 kPa at 77 K. (b) Snapshot of adsorption of H_2 and D_2 in CuBOTf and D_2 over H_2 selectivity of CuBOTf as function of pressure obtained from IAST and simulations at 40 and 77 K. (c) Schematic view of ZIF-8 and COF-102, and molar ratio of adsorbed D_2 over H_2 in ZIF-8 and COF-102 as a function of pressure in the range of 19.5 to 70 K.

Figure 2.2.3 (a) Crystal structure of MFU-4 and its alternatively interconnected large and small pore structure, and thermal desorption spectra after exposing 1:1 mixture at 60 K for 15, 30, and 60 min. (b) Schematic view of the pore channel of COF-1 incorporated pyridine molecules in the pore walls, and 1:1 mixture selectivity as a function of loading pressure for different exposure temperatures (T_{ex}). Reproduced with permission. (c) Schematic view of D_2 separation in 1D channel of MIL-53 (Al) during

the breathing propagation, and 1:1 mixture selectivity and D_2 uptake as a function of exposure temperature (T_{exp}).

Figure 2.2.4 (a) IAST selectivity (solid curve) and nD_2/nH_2 ratio (dashed line) of MOF-74 family at 77 (black), 87 (red), 100 (green), 120 (blue), and 150 K (brown). (b) Pure gas H_2 (open black circle) and D_2 (filled red circle) TDS spectra of CPO-27-Co. (c) TDS spectra of Cu(I)-MFU-4l after exposure to 10 mbar of 1:1 H_2/D_2 mixture at different exposure temperatures (T_{ex}) and showing the high-temperature range. (d) Selectivity of MOF-74-ac and MOF-74-IMs as a function of exposure temperature (T_{exp}) after exposing 1:1 H_2/D_2 mixture.

Figure 2.3.1 Schematic view of D_2 separation in breathing propagation along the 1D channel in MIL-53(Al).

Figure 2.3.2 XRPD patterns of MIL-53(Al) with the simulated XRPD patterns taken from reference 21.

Figure 2.3.3 FT-IR spectrum of MIL-53(Al).

Figure 2.3.4 Isotherm of H_2 sorption on MIL-53(Al) measured at 77 K.

Figure 2.3.5 (a) Isotherms of H_2 sorption on MIL-53(Al) measured at 20 K (black symbols), 40 K (red symbols), and 77 K (blue symbols), with the pressure shown in logarithmic scale. (b) Structural view of a large pore (*lp*) and a narrow pore (*np*) in MIL-53(Al) along the channel direction. Note: The H_2 sorption isotherms from 1 to 20 bar at 77 K were measured by a high-pressure sorption device (PCTPro-2000).

Figure 2.3.6 Thermal desorption spectra (TDS) of pure H_2 gas (black filled symbols) and D_2 (red open symbols) from MIL-53(Al) exposed at 10 mbar and an exposure temperature (T_{exp}) of 20 K

Figure 2.3.7 D_2 sorption sites of MIL-53(Al). Adapted with permission from reference 35. Copyright 2014 American Chemical Society.

Figure 2.3.8 (a) High pressure isotherm of H_2 sorption on MIL-53(Al) measured at 77 K (black) and 87 K (red), and (b) isosteric heat of adsorption of MIL-53(Al) obtained from high pressure H_2 sorption isotherm at 77K and 87K.

Figure 2.3.9 TDS of 1:1 D_2–H_2 mixed gas from MIL-53(Al) exposed at 10 mbar and T_{exp} of 25, 40, 60, and 77 K; the insets show close-ups of the spectra in the low-desorption rate region.

Figure 2.3.10 Isotherms of H_2 on MIL-53 at 20, 40, and 77 K. The green vertical dotted lines indicate the points at which the pressure was 10 mbar, which was the exposure-mixture pressure for the TDS measurements.

Figure 2.3.11 The selectivity (black symbols) and the corresponding amount of adsorbed D_2 (red symbols) as functions of (a) exposure temperature (T_{exp}), (b) exposure pressure (P_{exp}), and (c) exposure time (t_{exp}).

Figure 2.3.12 Thermal desorption spectra of mixture gas (1:1 H_2–D_2 mixture) at 40 K as a function of exposure pressure (a) 5 mbar, (b) 10 mbar, (c) 40 mbar, and (d) 80 mbar.

Figure 2.3.13 Thermal desorption spectra of mixture gas (1:1 H_2–D_2 mixture, 10 mbar) at 40 K as a function of exposure time (t_{exp}) (a) 10 min and (b) 120 min.

Figure 2.4.1 Schematic view of MOF-74-IM incorporating the OMS and imidazole. OMS and IM are employed for enhancing of the chemical affinity quantum sieving (CAQS) effect and the kinetic quantum sieving (KQS) effect, respectively.

Figure 2.4.2 XRPD patterns of MOF-74-ac (black), MOF-74-IM-10 (red), MOF-74-IM-38 (blue), and MOF-74-IM-70 (green) with the simulated XRPD patterns of MOF-74-Co.

Figure 2.4.3 FT-IR spectra of MOF-74-ac (black), MOF-74-IM-10 (red), MOF-74-IM-38 (blue), and MOF-74-IM-70 (green).

Figure 2.4.4 Diffuse reflectance UV-Vis-NIR spectra of MOF-74-ac (black), MOF-74-IM-10 (red), MOF-74-IM-38 (blue), and MOF-74-IM-70 (green).

Figure 2.4.5 Diffuse reflectance UV-Vis-NIR spectra of MOF-74-ac (black), MOF-74-IM-10 (red), MOF-74-IM-38 (blue), and MOF-74-IM-70 (green) after air exposure for 15 min. The peak intensity at ca. 5556 cm^{-1} of H_2O overtone decreases as increasing the amount of coordinated IM. For clarity, DR-UV-Vis-NIR spectra were shifted upward by 1.

Figure 2.4.6 Gas sorption isotherms on the MOF-74-ac and MOF-74-IMs. (**a**) N_2 sorption, and (**b**) H_2 sorption isotherms represented in linear and log scale at 77 K of MOF-74-ac (black), MOF-74-IM-10 (red), MOF-74-IM-38 (blue), and MOF-74-IM-70 (green). Filled and open symbols correspond to adsorption and desorption, respectively. The grey coloured graphs to the right are the enlargement of the low-pressure region in the sorption isotherms in log scale.

Figure 2.4.7 H_2 and D_2 sorption isotherms for (a) MOF-74-ac, and enlargement at (b) 20-23 K, (c) 40 K, and (d) 77 K. Filled and open symbols correspond to adsorption and desorption, respectively. The desorption isotherms for MOF-74-ac show the fully reversible desorption isotherm.

Figure 2.4.8 H_2 and D_2 sorption isotherms for (a) MOF-74-IM-10, and enlargement at (b) 20-23 K, (c) 40 K, and (d) 77 K. Filled and open symbols correspond to adsorption and desorption, respectively. The desorption isotherms for MOF-74-IM-10 show the large hysteresis.

Figure 2.4.9 H_2 and D_2 sorption isotherms for (a) MOF-74-IM-38, and enlargement at (b) 20-23 K, (c) 40 K, and (d) 77 K. Filled and open symbols correspond to adsorption and desorption, respectively. The desorption isotherms for MOF-74-IM-38 show the large hysteresis.

Figure 2.4.10 H_2 and D_2 sorption isotherms for (a) MOF-74-IM-70, and enlargement at (b) 20-23 K, (c) 40 K, and (d) 77 K. Filled and open symbols correspond to adsorption and desorption, respectively. The sorption isotherms for MOF-74-IM-70 show the nonporous nature.

Figure 2.4.11 Thermal desorption spectra of MOF-74-IM-10. (**a**) pure gas H_2 (black, filled circle) and D_2 (red, open circle) and (**b**) 1:1 D_2/H_2 mixture gas loading on MOF-74-IM-10 at an exposure temperature, T_{exp}, of 25 K. The site III clearly shows preferential adsorption of D_2 over H_2 from the isotope mixture.

Figure 2.4.12 H_2 (black, filled circle) and D_2 (red, open circle) desorption spectra of 10 mbar (1:1 D_2/H_2 mixture) loading on MOF-74-ac with a heating rate of 0.1 K/s. Exposure temperature (T_{exp}) at 25 K, 40 K, 60 K, and 77 K.

Figure 2.4.13 H_2 (black, filled circle) and D_2 (red, open circle) desorption spectra of 10 mbar (1:1 D_2/H_2 mixture) loading on MOF-74-IM-10 with a heating rate of 0.1 K/s. Exposure temperature (T_{exp}) at 25 K, 40 K, 60 K, and 77 K.

Figure 2.4.14 H_2 (black, filled circle) and D_2 (red, open circle) desorption spectra of 10 mbar (1:1 D_2/H_2 mixture) loading on MOF-74-IM-38 with a heating rate of 0.1 K/s. Exposure temperature (T_{exp}) at 25 K, 40 K, 60 K, and 77 K.

Figure 2.4.15 Adsorptive separation for an equimolar D_2/H_2 isotope mixture. (**a**) Selectivity for D_2 compared to H_2 and (**b**) D_2 uptake at strong binding sites (dashed line) and weak binding sites (dotted line) and total D_2 uptake (solid line) of MOF-74-ac (black), MOF-74-IM-10 (red), and MOF-74-IM-38 (blue) as a function of T_{exp}. At higher T_{exp} (above 60 K), D_2 adsorption only occurs at SBSs.

Figure 2.4.16 Kinetic effect of MOF-74-IM-38 at 60 K and 77 K. H_2 and D_2 desorption spectra of 10 mbar (1:1 D_2/H_2 mixture) loading on MOF-74-IM-38 with a different loading time (3 min and 120 min) at exposure temperature (T_{exp}) (a) 60 K and (b) 77 K and its corresponding (c) selectivity and (d) D_2 uptake.

Figure 2.4.17 Relaxed atomic position of the MOF-74 channel with incorporating imidazole (IM) molecules. Color scheme: Ni, turquoise; O, red; N, blue; C, grey; and H, white.

Figure 2.4.18 Graphical representation of the migration mechanisms of H_2 or D_2 considered in this study.

Figure 2.4.19 The migration profile of H_2/D_2 using classical method and zero point energy corrected migration energy of H_2/D_2 in kJ/mol.

Figure 2.4.20 Migration progress coordinates of hydrogen isotope molecule through MOF-74-IM. Seven figures show the initial (0) → transition (1-5) → final state (6) of hydrogen isotope (classical method).

Figure 2.4.21 Comparison of MOF-74-IM-10 with various porous frameworks for hydrogen isotope separation as a function of working temperature.[15] (Note: *1:1 D_2/H_2 mixture selectivity calculated from pure gas sorption isotherms using idealized adsorption solution theory (IAST) methods)

Chapter III

Figure 3.1 Schematic illustration of the preparation of MOF-fluoropolymer composite inks to form diverse structures via various processing techniques, and its use for sensor applications.

Figure 3.2 Characterization of $MOF_{HKUST\text{-}1(90)}$-ink with 90/10 wt% HKUST-1/PFPE. (a) Photograph of s-$MOF_{HKUST\text{-}1(90)}$-ink in a vial. (b) TEM images and EDS maps of Cu and F in photocured p-$MOF_{HKUST\text{-}1(90)}$-ink. The TEM image in the top-right is a magnified image of PFPE layer on HKUST-1 surface. (c) TEM image of hollow PFPE shell after selective etching of HKUST-1 in p-$MOF_{HKUST\text{-}1(90)}$-ink using piranha solution.

Figure 3.3 XRPD patterns of pristine HKUST-1 (middle) and p-$MOF_{HKSUT\text{-}1(90)}$-ink (top) compared with the simulated pattern of HKUST-1 (bottom).

Figure 3.4 SEM images of (a) pristine HKUST-1 and (b) p-$MOF_{HKSUT\text{-}1(90)}$-ink.

Figure 3.5 N_2 sorption isotherms of pristine HKUST-1 and p-$MOF_{HKSUT\text{-}1(90)}$-ink at 77 K.

Figure 3.6 Contact angle measurements of (a) HKUST-1 and (b) p-$MOF_{HKUST\text{-}1(70)}$-ink. The inset images are the photographs of each sample after dropping water droplets. (c) XRPD profiles of HKUST-1 and p-$MOF_{HKUST\text{-}1(70)}$-ink after immersion in water for 1 day.

Figure 3.7 SEM images of (a) pristine HKUST-1 and b) p-$MOF_{HKUST\text{-}1(90)}$-ink, after immersing in water for 1 day.

Figure 3.8 Processability of various MOF inks containing MIL-101 (Cr), ZIF-67, ZIF-8, and MOF-74 (Ni). (a) Photographs of five types of p-MOF(70)-ink thin films fabricated on glass plates by spray coating technique. (b) Photographs of writings using a pen filled with p-MOFHKUST-1(70)-ink on various substrates (paper, glass vial, cloth, and polyethylene film). (c) Photograph (left), optical

microscopy image (middle), and SEM image (right) of p-MOFHKUST-1(70)-ink dot array (200 μm diameter) patterned on a PDMS thin film by stencil printing technique.

Figure 3.9 (a) Photographic image of fiber-based tip of board marker. SEM images of fiber-based tip for (b) side view and (c) cross-sectional view. s-MOF-ink can be processed on the substrate along the pen movement by wetting the fiber-based tip of the pen. SEM images of (d) p-$MOF_{HKUST-1(70)}$-ink line written on the paper, and (e) enlargement of p-$MOF_{HKUST-1(70)}$-ink line.

Figure 3.10 Photographic images of 3-dimensional shaped p-$MOF_{HKUST-1(30)}$-ink *via* molding process; hemisphere, square pyramid, and cuboid.

Figure 3.11 SEM image of the p-$MOF_{HKUST-1(30)}$-ink.

Figure 3.12 No normalized luminescent spectra of pristine MOF_{chemo} immersed in pure VOC solvent upon excitation at 365 nm. The emission changes upon detection of VOCs from 430 nm to 445 nm for benzene, 475 nm for toluene, 504 nm for *p*-xylene, and 528 nm for styrene, respectively.

Figure 3.13 VOCs sensing with MOFchemo(70)-ink containing Zn2(bdc)2(dpNDI). (a) Photograph of 3D printed chameleon feature spray-coated with MOF-fluoropolymer ink as a VOC sensor under UV irradiation at 365 nm and SEM image of the chameleon surface. Scale bar: 2 μm. (b) Photographs of chameleon sensors under UV irradiation at 365 nm and (c) Normalized photoluminescence (PL) spectra of p-MOFchemo(70)-ink obtained after immersion in neat VOC solvent upon excitation at 365 nm. The emission peak changes upon detection of VOCs from 434 nm to 440 nm for benzene, 478 nm for toluene, 502 nm for p-xylene, and 528 nm for styrene, respectively. (d) Photographs of VOC molecule-patterned sensors on glass slides after immersion in aqueous VOC (0.2 vol%) solution under UV irradiation at 365 nm.

Figure 3.14 Optical images of (a) bare chameleon surface and (b) p-$MOF_{chemo(70)}$-ink coated chameleon surface.

Figure 3.15 SEM images of (a) bare chameleon surface and (b) p-$MOF_{chemo(70)}$-ink attached chameleon surface.

Figure 3.16 PXRD patterns of (a) pristine MOF_{chemo} and (b) p-$MOF_{chemo(70)}$-ink, compared with the simulated pattern from single crystal X-ray diffraction data of MOF_{chemo}.

Figure 3.17 Photographs of pristine MOF_{chemo} and p-$MOF_{chemo(70)}$-ink taken after soaking in water for 1 min under (a) room light and (b) UV irradiation at 365 nm.

Figure 3.18 A series of photographic images of a VOC-molecule patterned sensor on a slide glass under excitation at 365 nm, after soaking for different times in the emulsion of 0.2 vol% of benzene in water.

Figure 3.19 A series of photographic images a VOC-molecule patterned sensor on a slide glass under excitation at 365 nm, after soaking in the emulsion of 0.2 vol% of toluene in water.

Figure 3.20 A series of photographic images of a VOC-molecule patterned sensor on a slide glass under excitation at 365 nm, after soaking in the emulsion of 0.2 vol% of *p*-xylene in water.

Figure 3.21 A series of photographic images of a VOC-molecule patterned sensor on a slide glass under excitation at 365 nm, after soaking in the emulsion of 0.2 vol% of styrene in water.

Figure 3.22 XRPD patterns of pristine MOF_{thermo} and p-$MOF_{thermos(10)}$-ink, compared with the simulated pattern from single crystal X-ray diffraction data of $Eu(hfa)_3(dpbp)$[7].

Figure 3.23 Photographic images of various forms of p-$MOF_{thermo(10)}$-ink under a) room light and b) excitation at 365 nm.

Figure 3.24 SEM images of (a) bare stirring bar and (b) p-$MOF_{thermo(10)}$-ink on the stirring bar.

Figure 3.25 Photographic images of the p-$MOF_{thermo(10)}$-ink coated stirring bar stirred in (a) ice water (0 ^{o}C) and (b) boiling water (100 ^{o}C) under excitation at 365 nm. The inserted images of p-$MOF_{thermo(10)}$-ink coated stirring bar were taken after stirring for 3 hr in each bath.

Figure 3.26 Temperature sensing with a p-$MOF_{thermo(10)}$-ink containing $Tb_{0.99}Eu_{0.01}(hfa)_3(dpbp)$. (a) Photographs of a stirring bar coated with p-$MOF_{thermo(10)}$-ink that was placed in concentrated HCl, concentrated NaOH, and DMF for 5 min, respectively, under UV irradiation at 365 nm. (b) Photograph of temperature-visualizable ink-coated glass rod, the ends of which are placed on a cooling bath (−20 °C) and an oil bath (120 °C) under UV irradiation at 365 nm.

Figure 3.27 Photographic images of (a) pristine MOF_{thermo} powder and (b) square-shaped slices of p-MOF_{thermo}-ink were immersed in 11 different solvents for 5 min under excitation at 365 nm. The free standing p-$MOF_{thermo(10)}$-ink slices were obtained by cutting and detaching from the coated film on a slide glass.

Figure 3.28 Photographic images of rapid change in luminescence color of the p-$MOF_{thermo(10)}$-ink depending on the temperature of water poured into the cup; (a) 100 ^{o}C water and (b) 0 ^{o}C water. Yellow arrow indicates the surface of water.

Appendix

Figure 1 Simulation results of hetero core-shell structures from KAIST and cell parameter difference of HKUST-1 and MOF-5

Figure 2 Optical microscope image of products synthesized in (a) DMA, (b) DMF, and (c) DEF. inset images are the enlargement image of products. SEM images of products synthesized in (d) DMA, (e) DMF, and (f) DEF.

Figure 3 XPRD patterns of products from DMA, DMF, and DEF and compared with simulated patterns of HKUST-1. Yellow circle indicates the unknown crystalline phases.

Figure 4 Schematic and optical microscope images of core-shell products synthesized using different amounts of HKUST-1 (core).

Figure 5 Optical microscope images of core-shell products synthesized from (a) different amount of 2^{nd} MOF precursor solution and (b) different concentration of 20 mL of 2^{nd} MOF precursor solutions.

Figure 6 Optical microscope images of HKUST-1 with different size and corresponding core-shell crystals. The crystal sizes of HKUST-1 are (a) ca. 10μm, (b) ca. 70 μm, and (c) ca. 100-300 μm, respectively.

Figure 7 Optical images of HKUST-1@MOF-5 with different synthesis time (from 0 h to 24 h). Inset images are enlargement images of HKUST-1@MOF-5.

Figure 8 (a) Proposed mechanism in which (111) faces of MOF-5 grow upwards aligned on the surface of HKUST-1. (b) Schematic images of an epitaxially grown core-shell crystal structure and an optical microscope images of the corresponding core-shell crystal.

Figure 9 Schematic images of epitaxial growth and interpenetration.

Figure 10 Photo image of as synthesized core-shell and DCM exchanged core-shell.

Figure 11 (a) N_2 sorption isotherms of core-shell and ground core-shell. (b) Optical microscope images of core-shell and ground core-shell crystals.

Figure 12 Optical images of HKUST-1@IRMOF-18.

Figure 13 XPRD patterns of HKUST-1, IRMOF-18, HKUST-1@IRMOF-18 and compared with simulated patterns of HKUST-1 and IRMOF-18.

List of Tables

Chapter II

Table 2.3.1 Separation performance of the 1:1 D_2–H_2 mixture gas depended on exposure temperature (T_{exp}).

Table 2.3.2 Separation performance of the 1:1 D_2–H_2 mixture gas depended on exposure pressure (P_{exp}).

Table 2.3.3 Separation performance of the 1:1 D_2–H_2 mixture gas depended on exposure time (t_{exp}).

Table 2.4.1. Summary of experiment conditions with different molar ratio of imidazole to Ni^{2+} and elemental compositions of the resultant materials.

Table 2.4.2 Summary of N_2 sorption of MOF-74-ac, MOF-74-IM-10, MOF-74-IM-38, and MOF-74-IM-70.

Table 2.4.3 Summary of hydrogen isotope separation factors for various porous frameworks as a function of working temperature.

Chapter I. General Introduction

Metal-organic frameworks (MOFs), also called porous coordination polymers, are a rapidly expanding family of crystalline porous materials built from metal ion/clusters and ligands with specific and directional coordination bonding motif. Its high porosity and high structural diversity have captured widespread interest, allowing material scientists as well as inorganic chemists to dive into this research area[1-8]. As a result, so far, over 6,000 crystal structures have been deposited to the CSD (Cambridge structural database) and 29,700 SCI papers have been published.[8] In the early days of MOF research, establishing synthetic methods and understanding its physical and chemical properties were mainstream[9,10]. The efforts have shifted to find its applications and consequently, a variety of MOF uses have been studied, such as gas storage[11-14], separation[15,16], sensing[17,18], catalysis[19,20], luminescence[21,22], drug deliverer[23], proton/electron conduction[24-26], and energy conversion[27-29].

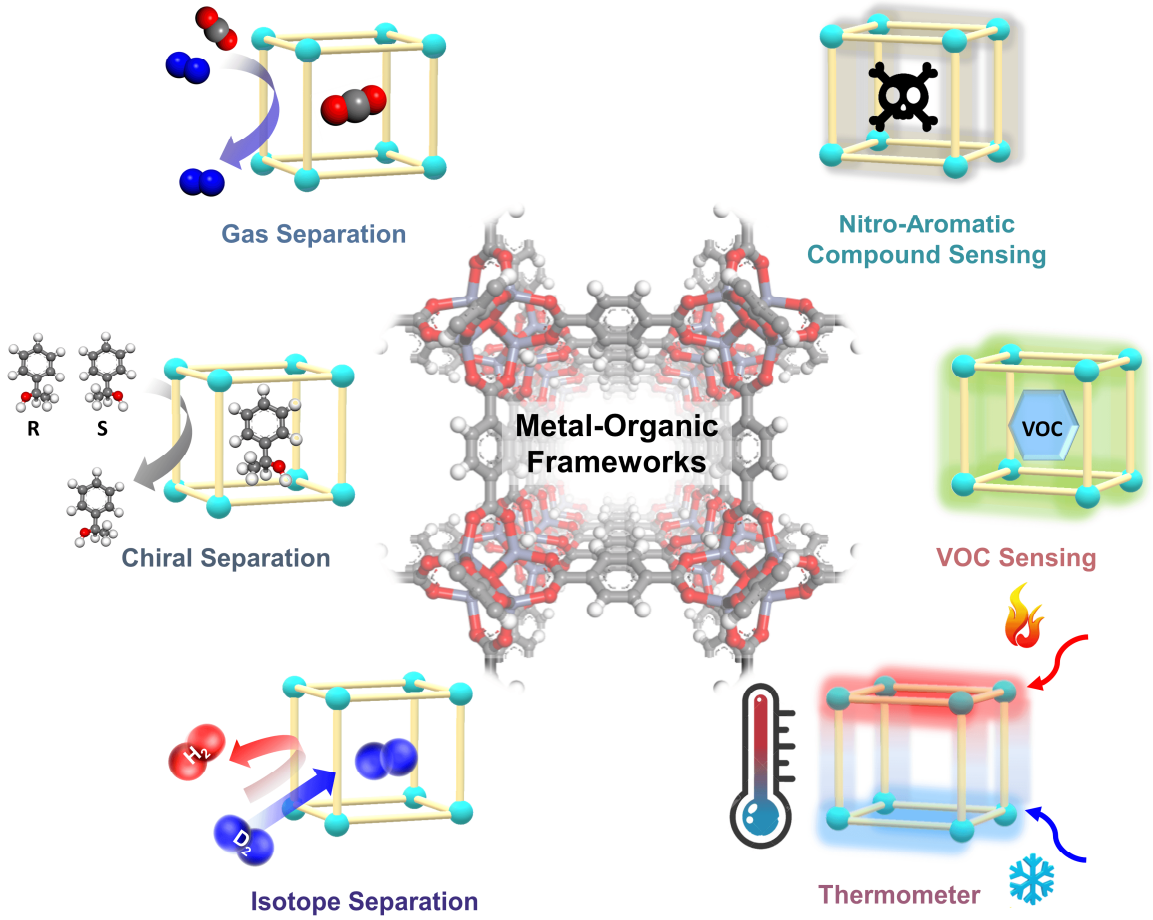

Figure 1.1 Schematic illustration of MOFs for separation and sensing applications.

Among the various application topics, separation and sensing studies have always been an important mainstream of MOF research, not only because of their importance in the industry but also because of the inherent characteristics of MOF which make these materials particularly suitable for this challenging task. The merging of crystal engineering and MOFs, in particular, has created a new and promising material platforms, with significant potential for separation and sensing. Compared to traditional polymeric or inorganic materials in these fields, crystal engineering of MOF using various directional coordination motifs of metal clusters and ligands not only enables the design of porous structures with desired size and shape but also gives MOFs diverse chemical properties and functionality through the introduction of functional sites[30-32]. Therefore, MOFs attracted attention in the application field requiring identification of target molecules, and structural and chemical diversification of MOFs triggered many studies on separation and sensing.

In separation, MOF not only can maximize the difference between the molecules in the mixture by crystal engineering resulting in high separation efficiency, but also has superior permeance than polymer due to permanent porosity. Thus, MOF-based separation studies cover a wide range of applications ranging from traditional separation such as gas or liquid phase separation to separation of isotopic mixtures that are one of the grandest challenge of modern separation technology[33]. Peng *et al.* reported that $Zn_2(bim)_4$ (bim : benzimidazole) nanosheet-membrane can have both high H_2/CO_2 selectivity and permeance simultaneously which is far beyond the Robeson upper bound, unlike conventional dense polymer membranes, demonstrating the potential of MOF as an efficient separation membrane[34]. Wang *et al.* reported photoswitchable MOF membrane with azobenzene moieties that can switch configuration according to light, showing that the smart membrane can be implemented that can control the selectivity and permeability by external stimuli (Figures 1.2a-c)[35]. Recently, separation studies using MOF have been extended to the separation of isotope mixtures, by maximizing the minute quantum differences of isotopes through controlled pore structure[36, 37]. In sensing application, Li group showed that porous MOF, $Zn_2(bpdc)_2(bpee)$ (bpdc=4,4'-biphenyldicarboxylate; bpee=1,2-bipyridylethene), is capable of very fast and fully reversible detection with very low detection limit (ca 0.18 ppm for 2,4-Dinitrotoluene (DNT) and ca. 2.7 ppm for 2,3-dimethyl-2,3-dinitrobutane (DMNB)), demonstrating the promising potential of crystalline porous MOF[38]. Furthermore, unlike traditional VOC sensors based on electrochemical sensor or gas chromatographs, Kitagawa group reported $Zn_2(bdc)_2(dpNDI)$ (bdc=terephthalate, dpNDI= *N*,*N*′-di(4-pyridyl)-1,4,5,8-naphthalenediimide) which can decode the various chemical substitution information of VOC molecules with the simple fluorescence change of the MOF without a complex analyzer (Figures 1.2d-f)[39]. This result demonstrated the feasibility of an inexpensive and portable miniaturized sensor based on MOF system.

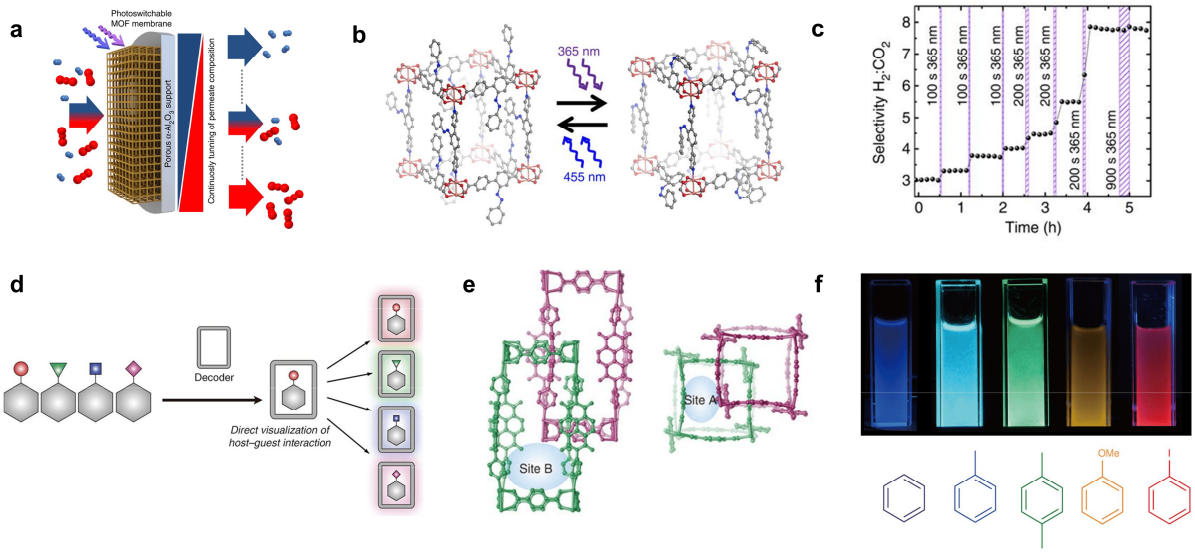

Figure 1.2 (a) Schematic images of swichable membrane separation. (b) The crystal structure of photoswitchable $Cu_2(AzoBPDC)_2(AzoBiPyB)$. (c) Tunnig H_2:CO_2 separation factor by adjusting the cis:trans azobenzene ratio. (d) Schematic image of melecular decoding. (e) The crystal structure of $Zn_2(bdc)_2(dpNDI)$ in the view along the main axes of bdc. (f) The resulting luminescence of $Zn_2(bdc)_2(dpNDI)$ suspended in various VOC solvents.

Despite the various promising findings of the MOFs, some are still under investigation, but some are over because many barriers to practical use have frustrated the researchers. These are mainly attributed to: i) hydrolytic, chemical, and thermal instability, ii) poor processability, and iii) degradation in performance due to differences between ideal measurement conditions and practical environment[40-42]. These limits have made well-designed multi-functional MOFs practically useless. Studies are underway to develop new MOFs showing better performance to meet the requirements in the application field, but designing and synthesizing new MOF structures are difficult and laborious. Therefore, a new perspective is needed to utilize various existing MOFs that have already been verified in performance so that they can be used in a real environment.

In this thesis, I report a series of separation and sensing application studies based on existing MOF through a new perspective, which optimizes the performance and overcomes a variety of stability and processing issues required for the real-world application. Chapter I is the general introduction part of MOF. Chapter II deals with the state of the art of hydrogen isotope separation system based on MOF. First, I discuss recent advances of hydrogen isotope separation in MOF based on separation mechanisms of quantum effects, analytical techniques, as well as computational and experimental studies. Further, based on previous findings, I discuss the ideal hydrogen isotope separation systems with the experimental results along with flexible MIL-53 (Al) having dynamic pore changes during breathing propagation (Chapter 2.3), and MOF-74-IM having both strong binding sites and kinetic barrier,

simultaneously (Chapter 2.4). Chapter III focuses on the research to improve the stability and processability of MOF for practical sensor applications by introducing photocurable and hydrophobic ‘F-rich’ polymer. Additionally, in the appendix, I propose and discuss a new type of core-shell structure composed of hetero-MOF pairs under study in collaboration with Professor Jihan Kim in KAIST.

References

1. Zhou, H.-C.; Long, J. R.; Yaghi, O. M. *Chem. Rev.* **2012**, *112*, 673.
2. Eddaoudi, M.; Kim, J.; Rosi, N.; Voda, D.; Wachter, J.; O'keeffe, M.; Yaghi, O. M. *Science* **2002**, *295*, 469.
3. Li, H.; Eddaoudi, M.; O'Keffe, M.; Yaghi, O. M. *Nature* **1999**, *402*, 276.
4. Chen, B.; Eddaudi, M.; Hyde, S. T.; O'Keeffe, M.; Yaghi, O. M. *Science* **2001**, *291*, 1021.
5. Rowsell, J. L. C.; Yaghi, O. M. *Microporous and Mesoporous Materials* **2004**, *73*, 3.
6. Lu, W.; Wei, Z.; Gu, Z.; Liu, T.; Park, J.;Park, J.; Tian, J.; Zhang, M.; Zhang, Q.; Gentle, T., III; B osch, M.; Zhou, H.-C. *Chem. Soc. Rev.* **2014**, *43*, 5561.
7. Falcaro, P.; Ricco, R.; Doherty, C. M.; Liang, K.; Hill, A. J.; Styles, M. J. *Chem. Soc. Rev.* **2014**, *43*, 5513.
8. Furukawa, H.; Cordova, K. E.; O'Keeffe, M.; Yaghi, O. M. *Science* **2013**, *341*, 1230444.
9. Yaghi, O. M.; O'Keeffe, M.; Ockwig, N. W.; Chae, H. K.; Eddaoudi, M.; Kim, J. *Nature* **2003**, *423*, 705.
10. Zhao, D.; Timmons, D. J.; Yuan, D.; Zhou, H.-C. *Acc. Chem. Res.* **2001**, *44*, 123.
11. Rosi, N. L.; Eckert, J.; Eddaoudi, M.; Vodak, D. T.; Kim, J.; O'Keeffe, M.; Yaghi, O. M. *Science* **2003**, *300*, 1127.
12. Suh, M. P.; Park, H. J.; Prasad, T. K.; Lim, D.-W. *Chem. Rev.* **2012**, *112*, 782.
13. Millward, A. R.; Yaghi, O. M. *J. Am. Chem. Soc.* **2005**, *127*, 17998.
14. He, Y.; Zhou, W.; Qian, G. Chen, B. *Chem. Soc. Rev.* **2014**, *43*, 5657.
15. Qiu, S.; Xue, M.; Zhu, G. *Chem. Soc. Rev.* **2014**, *43*, 6116.
16. Denny, M. S.; Moreton, J. C.; Benz, L.; Cohen, S. M. *Nat. Rev. Mater.* **2016**, *1*, 16078.
17. Kreno, L. E.; Leong, K.; Farha, O. K.; Allendorf, M.; Van Duyne, R. P.; Hupp, J. T. *Chem. Rev.* **2012**, *112*, 1105.
18. Yi, F.-Y.; Chen, D.; Wu, M.-K.; Han, L.; Jiang, H.-L. *ChemPlusChem* **2016**, *81*, 675.
19. Lee, J.; Farha, L. K.; Roberts, J.; Scheidt, K. A.; Nguyen, S. T.; Hupp, J. T. *Chem. Soc. Rev.* **2009**, *338*, 1450.

20. Huang, Y.-B.; Liang, J.; Wang, X.-S.; Cao, R. *Chem. Soc. Rev.* **2017**, *46*, 126.

21. Cui, Y.; Yue, Y.; Qian, G.; Chen, B. *Chem. Rev.* **2011**, *112*, 1126.

22. Allendorf, M.; Bauer, C.; Bhakta, R.; Houk, R. *Chem. Soc. Rev.* **2009**, *38*, 1330.

23. Wu, M.-X.; Yang, Y.-W. *Adv. Mater.* **2017**, *29*, 1606134.

24. Ramaswamy, P.; Wong, N. E.; Shimizu, G. K. *Chem. Soc. Rev.* **2014**, *43*, 5913.

25. Talin, A. A.; Centrone, A.; Ford, A. C.; Foster, M. E.; Stavila, V.; Haney, P.; Kinney, R. A.; Szalai, V.; El Gabaly, F.; Yoon, H. P. *Science* **2014**, *343*, 66.

26. Yang, F.; Xu, G.; Dou, Y.; Wang, B.; Zhang, H.; Wu, H.; Zhou, W.; Li, J.-R.; Chen, B. *Nat. Energy* **2017**, *2*, 877.

27. Zhang, T.; Lin, W. *Chem. Soc. Rev.* **2014**, *43*, 5982.

28. Kent, C. A.; Mehl, B. P.; Ma, L.; Papanikolas, J. M.; Meyer, T. J.; Lin, W. *J. Am. Chem. Soc.* **2010**, *132*, 12767.

29. Wang, J.-L.; Wang, C.; Lin, W. *ACS Catal.* **2012**, *2*, 2630.

30. Cook, T. R.; Zheng, Y.-R.; Stang, P. J. *Chem. Rev.* **2013**, *113*, 734

31. Bai, Y.; Dou, Y.; Xie, L.-H.; Rutledge, W.; Li, J.-R.; Zhou, H.-C. *Chem. Soc. Rev.* **2016**, *45*, 2327.

32. Lu, W.; Wei, Z.; Gu, Z. Y.; Liu, T. F.; Park, J.; Park, J.; Tian, J.; Zhang, M.; Zhang, Q.; Gentle, T., III; Bosch, M.; Zhou, H. C. *Chem. Soc. Rev.* **2014**, *43*, 5561.

33. Zhao, X.; Wang, Y.; Li, D.-S.; Bu, X.; Feng, P. *Adv. Mater.* **2018**, *30*, 1705189.

34. Peng, Y.; Li, Y.; Ban, Y.; Jin, H.; Jiao, W.; Liu, X.; Yang, W. *Science* **2014**, *346*, 1356.

35. Wang, Z.; Knebel, A.; Grosjean, S.; Wagner, D.; Bräse, S.; Wöll, C.; Caro, J.; Heinke, L. *Nat. Commun.* **2016**, *7*, 13872.

36. Oh, H.; Hirscher, M. *Eur. J. Inorg. Chem.* **2016**, 4278.

37. Weinrauch, I.; Savchenko, I.; Denysenko, D.; Souliou, S. M.; Kim, H.-H.; Tacon, M. L.; Daemen, L. L.;Cheng, Y.; Mavrandonakis, A.; Ramirez-Cuesta, A. J.; Volkmer, D.; Schütz, G.; Hirscher, M.; Heine, T. *Nat. Commun.* **2017**, *8*, 14496

38. Lan, A.; Li, K.; Wu, H.; Olson, D. H.; Emge, T. J.; Ki, W.; Hong, M.; Li, J. *Angew. Chem., Int. Ed.* **2009**, 48,2334

39. Takashima, Y.; Martinez, V.M.; Furukawa, S.; Kondo, M.; Shimomura, S.; Uehara, H.; Nakahama,

M.;Sugimoto, K.; Kitagawa, S. *Nat. Commun.* **2011**, 2, 168

40. Yuan, S.; Feng, L.; Wang, K.; Pang, J.;Bosch, M.; Lollar, C.; Sun, Y.; Qin, J.; Yang, X.; Zhang, P.; Wang, Q.; Zou, L.; Zhang, Y.; Zhang, L.; Fang, Y.;Li, J.; Zhou, H.-C. *Adv. Mater.* **2018**, *30*, 1704303.

41. Burtch, N. C.; Heinen, J.; Bennett, T. D.; Dubbeldam, D.; Allendorf, M. D. *Adv. Mater.* **2017**, 30, 1704124.

42. Howarth, A. J.; Liu, Y.; Li, P.; Li, Z.; Wang, T. C.; Hupp, J. T.; Farha, O. K. *Nat. Rev. Mater.* **2016**, *1*, 15018.

Chapter II. Isotope Separation in Metal-Organic Frameworks

The separation of a target molecule from isotopic mixtures is one of the most difficult challengings in the current separation industry because indistinguishable physicochemical properties of the isotopes render their efficient separation by conventional molecular sieving techniques difficult. Specifically, deuterium (D = ^{2}H) and tritium (T = ^{3}H) are stable isotopes of hydrogen that have an additional neutrons in the nucleus of hydrogen. Deuterium and tritium have similar chemical properties to hydrogen, but show completely different nuclear reactions due to the added neutrons. Therefore, in the nuclear science and nuclear energy industry, a technology for separating hydrogen isotopes at high purity is very important[1-3]. Furthermore, heavy hydrogen isotopes are irreplaceable raw material widely used in various applications such as medicine and health application such as imaging and cancel therapy[4], proton nuclear magnetic resonance spectroscopy[5], isotope tracing[6-8], and neutron scattering[9-11]. As global demand increases, therefore, it is urgently necessary to develop a method for efficiently separating hydrogen isotopes showing the extremely low content naturally.

Currently, feasible hydrogen isotope separation technologies on industrial plant scale are the Girdler sulfide process and H_2 distillation technique.[12] The Girdler sulfide process is a chemical exchange technique based on the difference between the chemical reaction rates of isotopes depending on temperature.[12] For instance, H_2S circulates in the closed loop and react with ordinary water to produce D_2S in the water of the cold tower (30 °C) and subsequently, D_2S is fed back to the water in the hot tower (130 °C) to enrich D_2O. Finally, deuterium can be obtained via the electrolysis of D_2O. H_2 distillation technique is based on the difference between the boiling temperatures of isotopes. This technique discriminates the isotope molecules by utilizing the minor difference between the boiling temperatures of the isotopes: 20.3 K for H_2 and 23.7 K for D_2, resulting in a separation factor of 1.5 at 24 K.[12] However, these techniques are highly energy- and time-intensive; nonetheless, they provide only a low separation factor, which stimulates the exploration of an alternative separation system.

As a promising alternative, kinetic quantum sieving (KQS) based on nanoconfined space was first proposed in 1995 by Beenakker et al.,[13] where a lighter isotope with a smaller de Broglie wavelength than a heavier isotope create an higher energy barrier at the entrance of the pores, leading to the difference between isotopic molecular transport. In this regards, the pore structure of the adsorbent is the key to enhancing the quantum separation effect. To verify the quantum separation mechanism and develop an ideal adsorbent, complementary studies between computational simulations and experimental studies using various porous materials have been carried out.[14-26] Consequently, the best separation factor of 13.6 at 40 K, [16] which is far superior to the separation efficiency of cryogenic distillation (~ 1.5 at 24 K), [12] was obtained by utilizing the KQS effect. However, the separation mechanism based on KQS exhibits significant selectivity only at cryogenic temperatures, which still

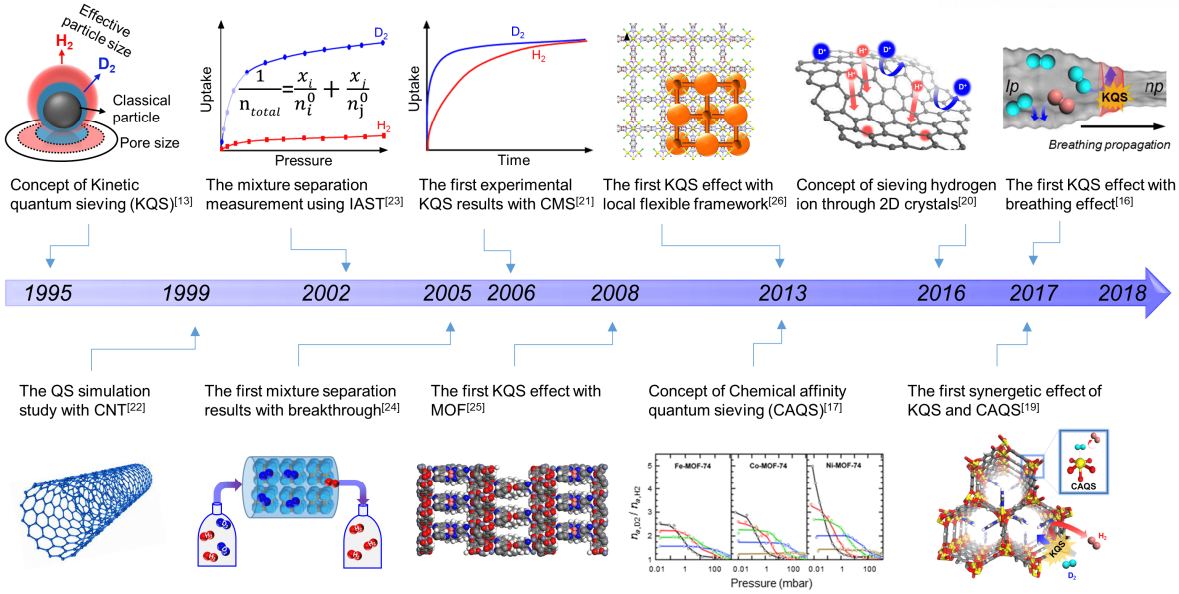

Figure 2.1 Timeline for the advances in hydrogen isotope separation in confined nanoporous spaces.

requires the huge energy consumption, rendering practical application difficult. In order to increase the operating temperature, the chemical affinity quantum sieving (CAQS) effect has been reported in 2013,[17] where heavier isotopes are selectively adsorbed at strong binding sites due to different zero-point energy; recently, it has been experimentally demonstrated that a high selectivity of 11 can be obtained even at a high temperature of 100 K.[18] Further isotope separation method using porous material has been recently developed by incorporating two quantum effects (KQS and CAQS) in internal porous frameworks, achieving the best separation factor of 26 at 77 K.[19] Another attempt to separate ionic isotope mixture has been also reported in 2016.[20] For instance, the selective separation of H^+ from an isotopic ion mixture has been published by utilizing a two-dimensional (2D) crystal as an ion separation membrane at room temperature. This allows selective separation of a trace amount of hydrogen contained in the resulting products after the separation of the isotope mixture using quantum sieving effects, so that higher-purity isotopes can be obtained. Figure 2.1 shows recent developments of advanced adsorbents including carbons, zeolites, metal-organic frameworks (MOFs), and covalent organic frameworks (COFs), as well as the evolution of analytical techniques from simulation to breakthrough measurement close to those used in the separation industry.

In this chapter, I discuss the state of the art of hydrogen isotope separation based on MOFs and COFs. First, I introduce recent advances of hydrogen isotope separation in MOFs and COFs based on separation mechanisms of quantum effects, analytical techniques, as well as computational and experimental studies. Further, based on previous findings, I discuss the ideal hydrogen isotope separation systems with the experimental results with two strategies as follows; first flexible MIL-53

(Al) system, which experiences dynamic pore change during the breathing transition, is introduced to optimize pore structure for maximizing the kinetic quantum sieving effect. Second, MOF-74-IM systems with diffusion barriers and strong binding sites were implemented by simple postmodification to obtain synergy of two quantum sieving effects, kinetic quantum sieving and chemical affinity quantum sieving.

References

1. Miller, A.I. *Can. Nucl. Soc. Bull.* **2001**, *22*, 1.
2. Glugla, M.; Lässer, R.; Dörr, L.; Murdoch, D.; Haange, R.; Yoshida, H. *Fusion Eng. Des.* **2003**, *69*, 39.
3. Souers, P. C. *Hydrogen properties for fusion energy*, University of California Press, Berkely, California **1986**.
4. Sanderson, K. *Nature* **2009**, *458*, 269.
5. Shi, C.; Fricke, P.; Lin, L.; Chevelkov, V.; Wegstroth, M.; Giller, K.; Becker, S.; Thanbichler, M.; Lange, A. *Sci. Adv.* **2015**, *1*, e1501087.
6. I. V. Stiopkin, C. Weeraman, P. A. Pieniazek, F. Y. Shalhout. J. L. Skinner, A. V. Benderskii, *Nature* **2011**, *474*, 192.
7. Povinec, P. P.; Bokuniewicz, H.; Burnett, W. C.; Cable, J.; Charette, M.; Comanducci, J. -F.; Kontar, E. A.; Moore, W. S.; Oberdorfer, J. A.; Oliveira, J. de.; Peterson, R.; Stieglitz, T.; Taniguchi, M. *J. Environ. Radioactiv.* **2008**, *99*, 1596.
8. Keppler, F.; Hamilton, J. T. G.; McRoberts, W. C.; Vigano, I.; Braß, M.; Röckmann, T. *New Phytol.* **2008**, *178*, 808.
9. Zaccai, G. *Science* **2002**, *288*, 1604.
10. Büldt, G.; Gally, H. U.; Seelig, A.; Seelig, J.; Zaccai, G. *Nature* **1978**, *271*, 182.
11. Machida, A.; Saitoh, H.; Sugimoto, H.; Hattori, T.; Sano-Furukawa, A.; Endo, N.; Katayama, Y.; Lizuka, R.; Sato, T.; Matsuo, M.; Orimo, S-i.; Aoki, K. *Nat. Commun.* **2014**, *5*, 5063
12. Rae, H. K. *Separation of Hydrogen Isotopes*, American Chemical Society, Washington DC, USA 1978, pp. 1-26.

13. Beenakker, J. J. M.; Borman,V. D.; Krylov, S. Y. *Chem. Phys. Lett.* **1995**, *232*, 379.

14. Cai, J.; Xing, Y.; Zhao, X. *RSC Adv.* **2012**, *2*, 8579.

15. Oh, H.; Hirscher, M. *Eur. J. Inorg. Chem.* **2016**, 4278.

16. Kim, J. Y.; Zhang, L.; Balderas-Xicohténcatl, R.; Park, J.; Hirscher, M.; Moon, H. R.; Oh, H. *J. Am. Chem. Soc.* **2017**, *139*, 17743.

17. FitzGerald, A.; Pierce, C. J.; Rowsell, J. L. C.; Bloch, E. D.; Mason, J. A. *J. Am. Chem. Soc.* **2013**, *135*, 9458.

18. Weinrauch, I.; Savchenko, I.; Denysenko, D.; Souliou, S. M.; Kim, H.-H.; Le Tacon, M.; Daemen, L. L.; Cheng, Y.; Mavrandonakis, A.; Ramirez-Cuesta, A. J.; Volkmer, D.; Schütz, G.; Hirscher, M.; Heine, T. *Nat. Commun.* **2017**, *8*, 14496.

19. Kim, J. Y.; Balderas-Xicohténcatl, R.; Zhang, L.; Kang, S. G.; Hirscher, M.; Oh, H.; Moon, H. R. *J. Am. Chem. Soc.* **2017**, *139*, 15135.

20. Lozada-Hidalgo, M.; Hu, S.; Marshall, O.; Mishchenko, A.; Grigorenko, A. N.; Dryfe, R. A. W.; Radha, B.; Grigorieva, I. V.; Geim, A. K. *Science* **2016**, *351*, 68.

21. Zhao, X.; Villar-Rodil, S.; Fletcher, A. J.; Thomas, K. M. *J. Phys. Chem. B* **2006**, *110*, 9947.

22. Wang, Q.; Challa, S. R.; Sholl, D. S.; Johnson, J. K. *Phys. Rev. Lett.* **1999**, *82*, 956.

23. Kotoh, K.; Nishikawa, T.; Kashio, Y. *J. Nucl. Sci. Technol.* **2002**, *39*, 435.

24. Sugiyama, T.; Asakura, Y.; Uda, T.; Kotoh, K. *Fusion Sci. Technol.* **2005**, *48*, 163.

25. Chen, B.; Zhao, X.; Putkham, A.; Hong, K.; Lobkovsky, E. B.; Hurtado, E. J.; Fletcher, A. J.; Thomas, K. M. *J. Am. Chem. Soc.* **2008**, *130*, 6411.

26. Teufel, J.; Oh, H.; Hirscher, M.; Wahiduzzaman, M.; Zhechkov, L.; Kuc, A.; Heine, T.; Denysenko, D.; Volkmer, D. *Adv. Mater.* **2013**, *25*, 635.

2.1 Fundamentals

Conventional gas separation by porous materials is usually achieved through three different mechanisms[1-5]: 1) molecular sieving by size and/or shape exclusion, 2) kinetic separation through different diffusing rates, and 3) thermodynamic equilibrium separation through different adsorbate–adsorbent interactions. Alternatively, exploiting the quantum effect in the kinetic separation or the thermodynamic equilibrium separation can realize isotope separation, which is also known as quantum sieving.

The following section presents a brief discussion of the fundamentals of isotope separation using porous materials and its characterization methods, in order to provide the necessary background information to understand the quantum sieving mechanism.

2.1.1 Kinetic Quantum Sieving

In classical mechanics, the diffusion rate of light gas molecules inside a porous material is faster than that of heavier ones, which is well suitable for the separation of a mixture of gases with a large mass difference. Light (e.g., helium or hydrogen) isotopes cannot be separated using this conventional kinetic separation as their diffusion rates are almost identical to each other in classical mechanics. Recently, a novel concept of exploiting quantum effect in a confinement system for isotope separation has been proposed by Beenakker et al.[6] When an aperture diameter in a porous material becomes comparable to the de Broglie wavelength of a light isotope, the quantum effect allows the isolation of heavier molecular species based on the differences in diffusion rate (the diffusivity of heavier isotope is faster than that of the lighter one). Note that this quantum effect is particularly prominent at cryogenic condition where the difference of de Broglie wavelengths is larger.

As shown in Figure 2.1.1, the quantum effect on molecular adsorption in a confined system can be explained by the zero-point energy (ZPE) of the free gas molecule and the potential depth of the adsorbed gas molecule[6]. By assuming very low density of gas at pore (hence neglecting the gas-phased molecule–molecule interaction) with no stronger interaction than van der Waals type, the molecule will interact only with the surface. Accordingly, the motion of the molecules in a confined pore is independently separated into the axial and radial directions. While the axial motion is free between two consecutive collisions with phonons or surface defects, the radial direction is restricted by a potential well created by the interaction with the pore walls. This interaction potential has been further approximated for radial motion by a circular square well with the depth ε (Figure 2a). Note that the well depth ε depends on the pore diameter d because of the potential overlap of different sizes of the wells (Figure 2b). The ZPE level (E_0) in a circular square well is expressed as follows:[6]

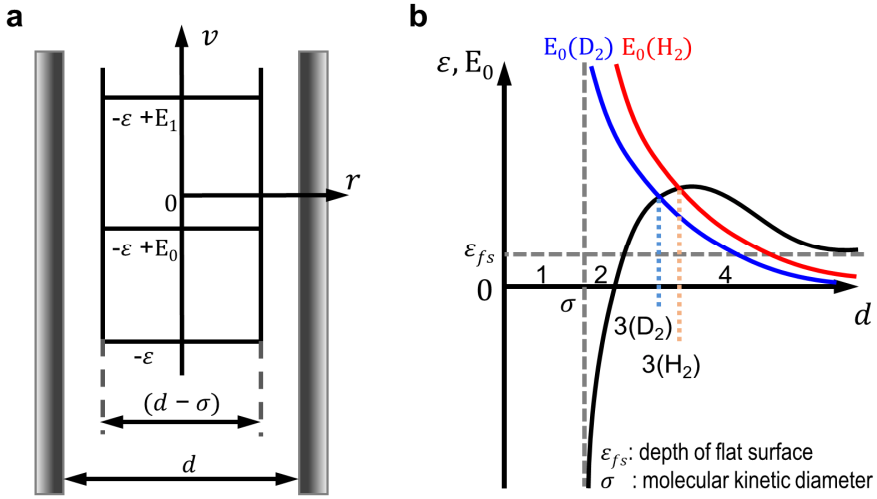

Figure 2.1.1 (a) Potential energy, *V*, and transverse motion energy levels, E_i, for a molecule in a channel with d-σ~λ (qualitative picture). (b) Behavior of well depth ε and zero point energy (E_0) of isotopes as functions of channel diameter *d*. Regions 1, 2, 3, and 4 can be attributed to classical geometrical potential (Regions 1, 2, and 4) and quantum sieving (Regions 3_{H2} and 3_{D2}), respectively.

$$E_i = \frac{2r_i^2\hbar^2}{(d-\sigma)^2 m}, \text{with } i = 0, 1, 2, ... \quad (1)$$

where E_i are counted with respect to the well bottom, r_i are simply related to the zeros of Bessel functions, $\hbar$ is a reduced Plank constant, σ is the molecular kinetic diameter, and *m* is the particle mass. Therefore, when i = 0, ZPE (E_0) exponentially increases with the decrease in *d* and *m* (Figure 2b).[13] In Figure 2b, which shows the behavior of well depth ε and E_0 of isotopes as functions of the channel diameter *d*, four regions exist; Region 1: gas molecules do not exist at the pore owing to the smaller size of the pore than that of the gas molecule. Region 2: steric repulsion still exists although the pore is slightly larger than the molecular size, resulting in the lack of adsorption at the pore surface. Region 4: as the potential well depth is larger than ZPE ($E_0 < \varepsilon$), gas adsorption at the pore or gas penetration through the pore is possible. Region 3: the ZPE overcompensates the interaction potential ($E_0 > \varepsilon$) at a pore larger than a molecule. While the potential well is still attractive for the molecules, gas molecule faces some sorption (or penetrating) barrier at the pore owing to the stronger ZPE (i.e., motion of gas molecules). In Region 3, this barrier is strongly influenced by the different ZPEs of molecules, which are caused by the mass difference between their isotopes (see Region 3 for H_2 and D_2).

Hence, as the aperture size approaches the gas molecule size, the ZPE of the isotope gas becomes larger than the adsorption potential energy, resulting in an increase in the penetration barrier, leading to lower equilibrium densities of the isotopes in the channel. Consequently, as heavy isotopes have lower ZPE than light isotopes, the equilibrium adsorption amount of heavy isotope is larger than that of light

isotopes under the same adsorption condition. According to this effect, heavy isotopes diffuse faster through a confined porous material than lighter isotopes, resulting in effective isotope separation under the given condition. This is the so-called “KQS.” Many related experimental studies of isotope separation utilizing the difference between the quantum effects of isotopes are in progress.

2.1.2 Chemical Affinity Quantum Sieving

Along with KQS, thermodynamic effects can be used to separate hydrogen isotope mixtures. When a stronger interaction than van der Waals type exists, the molecule–solid interaction of isotopes is no longer negligible. In general, the different strengths of adsorbate–adsorbent interactions cause preferential adsorption of certain components over others on the specific sorption site, leading to the thermodynamic equilibrium separation. Furthermore, this selective adsorption mechanism is not limited by the pore size. This mechanism can be applied to isotope separation. Typically, a diatomic molecule in gas-phase possesses six degrees of freedom (three translations, two rotations, and one vibration) and a monatomic molecule possesses three degrees of freedom (only x, y, z translation). Once this molecule is adsorbed on the surface with the affinity strength of the sorption site, almost all the degrees of freedom might be hindered except the vibrational energy levels normal to the surface, which is strongly influenced by the ZPE. Figure 2.1.2 shows a schematized physisorption potential for adsorption sites with different sorption strengths. The interaction strength of each sorption site is expressed as the depth of the potential well, and the steeper the well depth, the larger the difference in the ZPE of isotopes. Hence, the heavier isotopes have lower ZPEs when adsorbed, which leads to a difference in the adsorption enthalpies, allowing for predominant adsorption on heavy isotopes. The separation mechanism using this phenomenon—where ΔZPEs increase as Δmass increases on a strong sorption site, leading to an increment in ΔH and consequently selectivity enhancement, which is called CAQS. Notably, as the deeper adsorption potential leads to higher molecular desorption temperature, the isotope separation via CAQS can be realized even at high temperature.

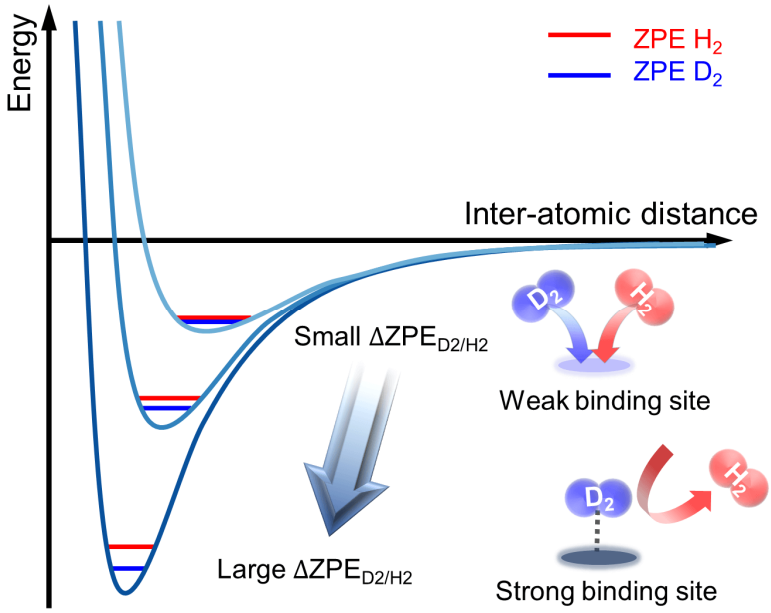

Figure 2.1.2 Difference potential well depths that represent the strength of the binding energy. The red and blue marks indicate ZPEs of isotopes H_2 and D_2, respectively.

2.1.3 Analytical Techniques for Isotope Separation

Molecular Simulation : As the chemical properties of isotopes are almost identical, very few analytical techniques are feasible for evaluating the separation performance. The theoretical approach and computational calculations are complementary methods widely used for predicting the performance of the isotope separation in porous media. Hence, various simulation methods have been used to evaluate the isotope separation performance of adsorbents from the early days of the separation study when there was no proper experimental setup for isotope separation.

Among these techniques, molecular dynamics is often used to investigate the dynamic diffusion process of hydrogen molecules, and grand canonical Monte Carlo (GCMC) simulation is used to simulate the equilibrium adsorption state of gas molecules in the adsorbent[7,8]. In particular, GCMC simulation has been widely used as a reliable method for determining the equilibrium physisorption state of hydrogen isotope gas molecules in an adsorbent exposed in a container containing a hydrogen isotope mixture. The temperature and chemical potential of the adsorbed gases at equilibrium state are equal to those of the remaining gas molecules in the container. Therefore, using the temperature and chemical potential in the container and adsorbent structure as essential parameters in GCMC simulations, the adsorbed gas amount of each isotope can be obtained.

In order to accurately predict the separation results of a real system through simulation, it is very important to precisely calculate the interactions between the adsorbent–gas molecules or between gas molecules. Typically, the adsorption properties of hydrogen were simulated using GCMC with quantum corrected interaction potentials. Feynman-Hibbs (FH)-GCMC adapts the Feynman and Hibbs effective potential approximation, which is developed from the Lennard-Jones (LJ) potential with additional terms of quantum corrections[9-11]. The interaction potential between two classical particles is modeled *via* the LJ potential described as follows;

$$\phi(\mathrm{r}) = 4\varepsilon\left[\left(\frac{\sigma}{\mathrm{r}}\right)^{12} - \left(\frac{\sigma}{\mathrm{r}}\right)^{6}\right] \quad (2)$$

where ε is the depth of depth of an attractive well, and σ is a size parameter. Since quantum effects become more important when adsorbing in the confined space, the quantum effects should be considered in interaction potential model to obtain accurate adsorption prediction. To do so, FH formalism is usually adapted to model the quantum interaction potential between particle-solid atoms (in adsorbate), in which the quantum particle is expressed by a Gaussian wave packet with width (w)

$$\mathrm{w} = \frac{\hbar}{\sqrt{12\mu \mathrm{k_B T}}} \quad (3)$$

where μ is the reduced mass, $\hbar$ is Planck's constant divided by 2π, and k_B is Boltzmann's constant. This Gaussian wave packet is applied and averaged over the LJ potential to obtain the effective FH potential as follows:

$$\phi_{\mathrm{FH}}(\mathrm{r}) = \phi(\mathrm{r}) + \left(\frac{\hbar^2}{24\mu \mathrm{k_B T}}\right)\nabla^2\phi(\mathrm{r}) \quad (4)$$

In GCMC with Feynman's path-integral formalism (PI-GCMC), the statistical properties of quantum fluids are explored by correcting the classical thermodynamic and kinetic quantities by quantum fluctuations. When adsorption occurs in a confined space at low temperature, the adsorbed gas molecules are accelerated due to quantum kinetic contributions, and at this point, lighter isotope molecules have a higher velocity. These quantum kinetic properties also affect the adsorption of molecules in terms of thermodynamics and the kinetics. From a thermodynamic point of view, the light isotope molecules are less likely to stick the adsorption surface and their adsorption enthalpy is decreased. Note that this method is particularly effective for adsorption studies in large pores, but it is known to be relatively ineffective for adsorption studies in small pores.

To conveniently compare the simulation data obtained from GCMC simulation with the experimental data as a function of the pressure at an identical temperature, the chemical potential is usually converted

to the corresponding partial pressure using the following formulas in case of an ideal gas system:[32,33]

$$\mu = \frac{1}{\beta}\ln\left(\Lambda^3 \beta P\right) \quad (5)$$

where μ denotes the chemical potential, $1/\beta = k_B T$, Λ is the thermal de Broglie wavelength, and P is the reservoir pressure. However, in a real gas system, where the interaction between gas molecules cannot be ignored, the corrected pressure, fugacity, is used instead of the ideal gas pressure.

$$\mu = \frac{1}{\beta}\ln(\Lambda^3 \beta \phi P) \quad (6)$$

where $\phi \equiv f/P$ is a fugacity coefficient, f is fugacity of a non-ideal gas, and P is the ideal gas pressure. Furthermore, as the processing power of computers has been significantly improved recently, a high-performance computer can be employed for the simulations (e.g., first principles, density functional theory calculation, etc.) of isotope mixture separation[12-16]. These quantum mechanical calculations can immerse the various quantum energy terms including vibrational energy by an analytical solution of the Schrödinger equation, providing more accurate results for isotope separation.

Ideal Adsorbed Solution Theory (IAST) based on Single-Component Gas Sorption Isotherm : Pure- and single-component sorption isotherms are routinely obtained accurately using commercial devices, but the measurement of the specific gas sorption in the presence of a mixture gas component is very complicated and time-consuming, and requires sophisticated home-built instruments. Therefore, numerous studies have been conducted on the methods to predict multi-component sorption behavior based on the experimental isotherms of pure components, and among these methods, thermodynamic approaches (best known as ideal adsorbed solution theory, IAST) are especially useful.[17] Thus, at first, the pure component experimental isotherm data are fitted to the adsorption model equation, and subsequently, the binary equilibria can be studied using IAST. Consequently, in the early stages of the isotope separation studies, most studies have been conducted using IAST methods based on the fitting of single-isotope isotherm data, owing to the absence of a direct method to measure the selective sorption in the multi-component isotope mixture.

From the fitting results of the equilibrium isotherm of each isotope, the spreading pressure of the adsorption phase can be obtained according to the pressure. The spreading pressures of each component in the equilibrium adsorption state of an isotopic mixture should be the same, and thus, the adsorption amounts of each component can be calculated. Note that a suitable adsorption model (e.g., single-/dual-site Langmuir or Langmuir–Freundlich adsorption model) is required to obtain reliable IAST selectivity and IAST is not applicable to adsorbents with strong interaction sites sufficient to break H-H or D-D bonds. Although IAST can predict the isotope mixture selectivity from a set of pure components of

isotope adsorption isotherms alone by assuming the mixed adsorbate as an ideal solution in equilibrium with the gas phase, the mixture selectivity obtained through the IAST is strongly dependent on the fitting isotherms, and small erroneous fitting could lead to a large difference in selectivity, especially at the low-pressure region. This has been proven via comparison with the experimental results of a multi-component gas system measured using home-built instrumentations[18,19].

Advanced Cryogenic Thermal Desorption Spectroscopy (ACTDS) for Direct Mixture Selectivity : To elucidate the quantum sieving effect, a direct mixture analysis at the cryogenic condition where quantum effects are pronounced, is required. As mentioned in the previous chapter, earlier, almost all the studies on isotope selectivity were limited to the theoretical calculation based on the pure components, and thus, an advanced analytical technique for the direct measurement of mixture selectivity was necessary. Thermal desorption spectroscopy (TDS), also known as temperature programmable desorption (TPD), is a method of observing gases desorbed from the surface while elevating the surface temperature after exposing the sample to a target gas pressure at a preset temperature. TDS has a typical operating temperature range from room temperature to 1000 °C and provides information on the binding energy of adsorbed atoms and molecular species. However, with a combination of cryocooler system or cryostat with liquid He in the TDS, advanced cryogenic thermal desorption spectroscopy (ACTDS), which can lower temperatures down to 20 K, can be developed, and can even resolve the very weak binding strength of gas physisorption[20.21]. The ACTDS can directly control the exposed isotopic mixture ratio and systematically adjusted exposure times and pressures at cryogenic condition (Figure 2.1.3)[22]. By employing a mass spectrometer, in addition, the detection of species and quantity of the desorbed molecules can be analyzed in real time, and the separation factor is directly determined by the ratio of desorbed isotope amounts, as shown in a recent isotope separation study using TDS[22].

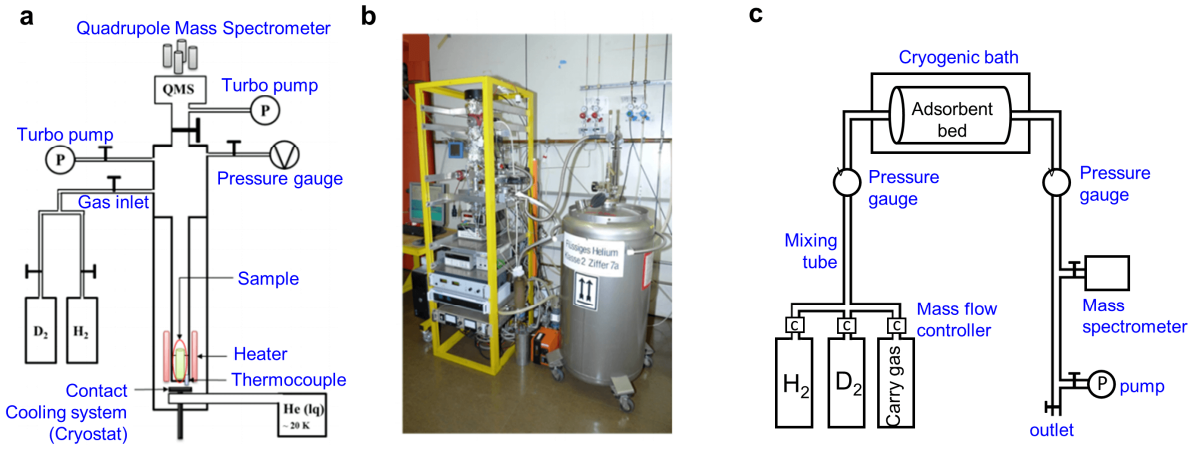

Figure 2.1.3 (a) Schematic diagram of advanced TDS and **(**b) experimental setup for ACTDS. (c) Schematic diagram of breakthrough apparatus.

Breakthrough Curve Analysis : Most industrial separation processes using porous materials are in the dynamic condition such as a flow environment. As separation processes are performed with mixtures of different multi-components, a breakthrough experiment is a very useful method to measure the performance of the selective adsorbent in a dynamic condition[23-25]. The analysis of the effluent gas flow through a fixed bed filled with an adsorbent provides important information on the separation performance, adsorption capacity, sorption kinetic, and selectivity of each gas component under dynamic flow.

In isotope separation research, breakthrough experiments are required to measure the separation performance in environments close to those used in the separation industry. Upon exposing the adsorbent to the flow environment of the isotope gas mixture directly, the real-time monitoring of the effluent gas reveals the adsorption capacity (or concentration) for each gas component of the adsorbent, and the separation factor of each component can be directly determined by the ratio of the adsorbed amounts (Figure 4c). Similar to the ACTDS, the breakthrough test requires low-temperature control in order to evaluate the quantum sieving effect for isotope separation. Recently, only a few groups have briefly performed the cryogenic breakthrough measurement[26-29], and therefore, it is further required to develop a real-time low-temperature breakthrough device in order to satisfy the industry demands.

2.1.4 References

1. Do, D. D. *Adsorption Analysis: Equilibria and Kinetics*, Imperial College Press, London, UK 1998.
2. Ismail, A. F.; David, L. I. B. *J. Membr. Sci.* **2001**, *193*, 1.
3. Kosinov, N.; Gascon, J.; Kapteijn, F.; Hensen, E. J. M. *J. Memb. Sci.* **2016**, *499*, 65.
4. Li, J.-R.; Kuppler, R. J.; Zhou, H.-C. *Chem. Soc. Rev.* **2009**, *38*, 1477.
5. Bae, Y.-S.; Snurr, R. Q. *Angew. Chem., Int. Ed.* **2011**, *50*, 11586.
6. Beenakker, J. J. M.; Borman, V. D.; Krylov, S. Y. *Chem. Phys. Lett.* **1995**, *232*, 379.
7. Frenkel, D.; Smit, B. *Understanding Molecular Simulation from Algorithms to Applications*; Academic Press: San Diego, CA, USA 2002.
8. Luo, T. Lloyd, J. R. *Inter. J. Energy Clean Environ.* **2009**, *10*, 37.
9. Feynman, R.P. *Statistical Mechanics: a Set of Lectures*, Benjamin, New York, 1972.
10. Feynman, R.P.; Hibbs, A.R. *Quantum Mechanics and Path Integrals*, McGraw-Hill, New York, 1965.
11. Tanaka, H.; Kanoh, H.; Yudasaka, M.; Iijima, S.; Kaneko, K. *J. Am. Chem. Soc.* **2005**, *127*, 7511
12. Cai, J.; Xing, Y.; Zhao, X. *RSC Adv.* **2012**, *2*, 8579.
13. Li, F.; Qu, Y.; Zhao, M. *Carbon* **2015**, *95*, 51.
14. Qu, Y.; Li, F.; Zhou, H.; Zhao, M. *Sci. Rep.* **2016**, *6*, 19952.
15. Qu, Y.; Li, F.; Zhao, M. *Sci. Rep.* **2017**, 7, 1483.
16. Hankel. M.; Jiao, Y.; Du, A.; Gray, S. K.; Smith, S. C. *J. Phys. Chem. C* **2012**, *116*, 6672.
17. Myers, A. L.; Prausnitz, J. M. *AlChE J.* **1965**, *11*, 121.
18. FitzGerald, A.; Pierce, C. J.; Rowsell, J. L. C.; Bloch, E. D.; Mason, J. A. *J. Am. Chem. Soc.* **2013**, *135*, 9458.
19. Kim, J. Y.; Balderas-Xicohténcatl, R.; Zhang, L.; Kang, S. G.; Hirscher, M.; Oh, H.; Moon, H. R. *J. Am. Chem. Soc.* **2017**, *139*, 15135.
20. Panella, B.; Hirscher, M.; Ludescher, B. *Microporous Mesoporous Mater.* **2007**, *103*, 230.
21. Panella, B.; Hones, K.; Muller, U.; Trukhan, N.; Schubert, M.; Putter, H.; Hirscher, M. *Angew. Chem., Int. Ed.* 2008, **47**, 2138.

22. Oh, H.; Hirscher, M. *Eur. J. Inorg. Chem.* **2016**, 4278.

23. Nugent, P.; Belmabkhout, Y.; Burd, S. D.; Cairns, A. J.; Luebke, R.; Forrest, K.; Pham, T.; Ma, S.; Space, B.; Wojtas, L.; Eddaoudi, M.; Zaworotko, M. J. *Nature*, **2013**, *495*, 80.

24. Liao, P.-Q.; Zhang, W.-X.; Zhang, J.-P.; Chen, X.-M. *Nat. Commun.* **2015**, *6*, 8697.

25. Liao, P.-Q.; Huang, N.-Y.; Zhang, W.-X.; Zhang, J.-P.; Chen, X.-M. *Science* **2017**, *356*, 1193.

26. Chu, X.-Z.; Cheng, Z.-P.; Zhao, Y.-J.; Xu, J.-M.; Li, M.-S.; Zhou, L.; Lee, C.-H.*Sep. Purif. Technol.* **2015**, *146*, 168.

27. Kotoh, K.; Tanaka, M.; Nakamura, Y.; Sakamoto, T.; Asakura, Y.; Uda, T.; Sugiyama, T. *Fusion Eng. Des.* **2008**, *54*, 411.

28. Kotoh, K.; Tanaka, M.; Sakamoto, T.; Nakamura, Y.; Asakura, Y.; Uda, T.; Sugiyama, T. *Fusion Eng. Des.* **2008**, *54*, 415.

29. Chu, X.; Zhao, Y.; Kan, Y.; Zhang, W.; Zhou, S.; Zhou, Y.; Zhou, L. *Chem. Eng. J.* **2009**, *152*, 428.

2.2 Previous Researches of Hydrogen Isotope Separation in MOFs and COFs

Recently, new classes of crystalline nanoporous materials, MOF and COF, have received immense attention for novel separation such as that of an isotope mixture[1]. The pore structure of these nanoporous materials can be precisely adjusted by proper selection of building blocks and further optimization is available by introducing new functional groups or molecules via the post modification strategy. In addition, the highly crystalline nature of MOF and COF enables direct structure identification by single crystal X-ray diffraction and allows investigation of the interaction sites and separation process between frameworks and molecules. Therefore, considering the separation mechanism of isotope mixtures through very small quantum property differences, MOF and COF, which are capable of precisely controlling the structure and studying the separation process, are very attractive materials for isotope separation, and research using these nanoporous materials have been intensively conducted recently.

2.2.1 Simulations

Garberoglio first reported the simulation studies using PI-GCMC for quantum sieving in various types of MOFs and COFs: IRMOF-1, IRMOF-14, COF-6, COF-102, ZIF-68, ZIF-74, Zn-TBIP (H_2tbip=5-tert-butyl isophthalic acid), and CuBOTf ($[Cu(4,4'\text{-bipy})_2]CF_3SO_3$, bipy=4,4'-bipyridyl).[2] The results showed that the selectivity is strongly dependent on the temperature and less affected by the external pressure. The largest quantum sieving effect occurs in the adsorbent with the narrowest pore structure (i.e., Zn-TBIP), resulting in the highest T_2/H_2 zero-pressure selectivity of 31.7 at 20 K (Figure 2.2.1a, b). Above 150 K, however, the quantum sieving effect is almost vanished, leading to no separation of isotopes. Liu et al. further performed the computational studies on the quantum sieving behavior of nine MOFs with different channel sizes in the range 2.9 to 6.2 Å.[3] Their simulation results indicated that selectivity through quantum sieving did not correlate well with the conventional pore size. Thus, the new concept of "quantum effective pore size (QEPS)" was introduced considering the swelling of the potential size parameter of the adsorbate–adsorbent owing to the quantum effect. Owing to this new concept, QEPS, the authors could correlate between the pore size and selectivity (Figure 2.2.1c, d), which is consistent with other simulation results.

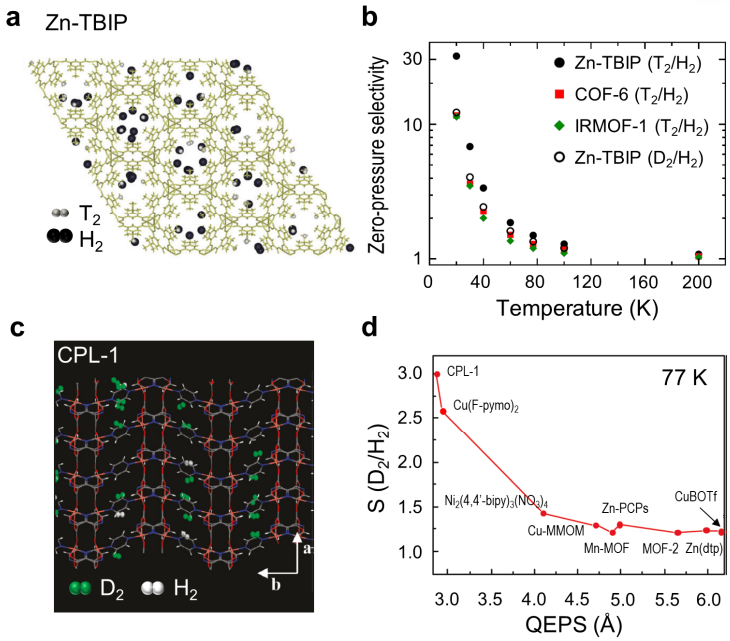

Figure 2.2.1 (a) Snapshot of Zn-TBIP with adsorbed T_2 and H_2 at 10^{-19} bar and 20 K and (b) zero pressure selectivity of MOFs as a function of temperature. (c) Snapshot of CPL-1 with adsorbed D_2 and H_2 at 0.01 Mpa and 77 K and (d) selectivity of D_2 over H_2 of nine channel-type MOFs as a function of the quantum effective pore size of MOFs at 0.001 MPa and 77 K.

2.2.2 Framework with Rigid Structure

One of the earliest studies reported the KQS effect for hydrogen isotope separation using a bimodal porous framework, $Zn_3(BDC)_3[Cu(Pyen)]$ (M′MOF 1) (H_2BDC = 1,4-benzenedicarboxylic acid, $PyenH_2$ = 5-methyl-4-oxo-1,4-dihydro-pyridine-3-carbaldehyde), which has large pores of size 5.6 × 12.0 $Å^2$ and small irregular ultramicropores (Figure 2.2.2a)[4]. The H_2 and D_2 adsorption isotherms at 77 and 87 K showed nD_2/nH_2 ratios in the range 1.09–1.11, which did not change significantly within the pressure range 0.5–100 kPa. However, the H_2 and D_2 adsorption kinetic profiles clearly indicated that the adsorption kinetics of D_2 were faster than those of H_2 in both types of pores. Around the same time, Kaneko's group also addressed the quantum sieving effect on the sorption isotherms of Cu(4,4'-bipyridine)$_2$(CF_3SO_3)$_2$(CuBOTf) having two types of 1D channels by combining experimental and quantum-simulated isotherms[5]. As the dimension of the small channel (2.0 × 2.0 $Å^2$) is smaller than the size of the hydrogen molecule (2.8–2.9 Å), the authors assumed that adsorption occurred only on the large channel (8.7 × 8.7 $Å^2$) (Figure 2.2.2b). The experimental H_2 and D_2 adsorption isotherms of CuBOTf at 77 K showed that D_2 adsorption amounts exceeded those of H_2 by approximately 13% over the entire pressure range, which was consistent with the GCMC simulated isotherms considering the quantum effect, showing direct evidence of the quantum sieving effect on CuBOTf. The selectivity of

the 1:1 D_2/H_2 mixture was estimated by applying IAST to the pure gas isotherms. The IAST selectivity of 1:1 H_2/D_2 mixed gas was 1.3 at 77 K but increased up to the range 2.6 to 5.8 at 40 K, owing to the enhanced quantum effect with the decrease in temperature.

To design and develop a porous adsorbent with an optimized pore system capable of efficient isotope separation, fundamental studies on the correlation between pore size and quantum selectivity are essential. Oh et al. systematically investigated the dependence of quantum sieving selectivity on the aperture diameters of porous structure[6]. Four kinds of frameworks, ZIF-7, ZIF-8, COF-1, and COF-102, with different pore aperture sizes of 3.0, 3.4, 9.0, and 12 Å, respectively, were selected for the study (Figure 2.2.2c). The adsorption isotherms of H_2 and D_2 in the porous structures were type I isotherms, except for ZIF-7, which showed negligible adsorption amount as its aperture size (3.0 Å) was comparable to the kinetic diameter of gas molecules (2.9 Å). At various temperatures ranging from 19.5 to 70 K, the D_2 uptake was higher than that of H_2 over the entire pressure range, and this trend was more evident with the decrease in temperature and pore aperture size. The nD_2/nH_2 molar ratio of COF-102 with a large pore size of 12 Å was slightly larger than 1, indicating an insignificant effect of quantum sieving. However, with the decrease in pore size to 9 and 3.4 Å, the quantum sieving effect became stronger at near zero coverage pressure and the maximum molar ratio reached 11 at 19.5 K. This systematic experimental study revealed that the optimum aperture may be larger than 3.0 Å but smaller than 3.4 Å. Although optimum aperture size is proposed, unfortunately, significant selectivity was only observed at cryogenic temperature with near vacuum condition, which are not suitable for practical separation processes.

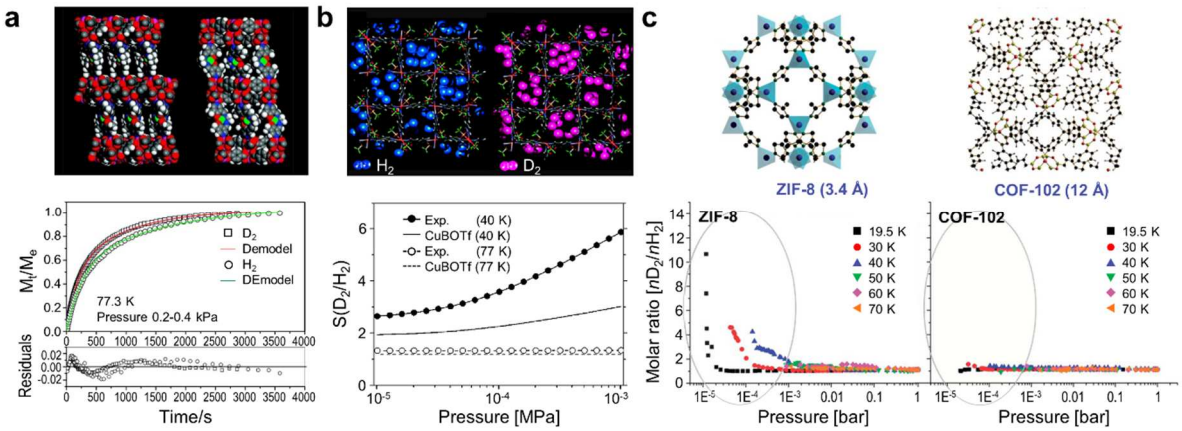

Figure 2.2.2 (a) Schematic view of M′MOF 1 and H_2 and D_2 adsorption kinetic profiles of M'MOF for pressure increment 0.2-0.4 kPa at 77 K. (b) Snapshot of adsorption of H_2 and D_2 in CuBOTf and D_2 over H_2 selectivity of CuBOTf as function of pressure obtained from IAST and simulations at 40 and 77 K. (c) Schematic view of ZIF-8 and COF-102, and molar ratio of adsorbed D_2 over H_2 in ZIF-8 and COF-102 as a function of pressure in the range of 19.5 to 70 K.

2.2.3 Local Flexibility and Breathing Effect

The MOF and COF with flexible nature exhibit different aperture geometry depending on the exposed temperature and pressure, which can lead to relatively high operating temperatures and pressures unlike a conventional rigid porous framework[7-9]. As the KQS effect is very sensitive to the pore structure, not only a change in the entire pore structure, called breathing, but also microscopic changes in atoms or molecules decorated inside the pore can affect the separation performance. Therefore, instead of expending efforts to define the precise pore diameter, it may be better if quantum sieving can exploit easily controllable parameters such as pressure or temperature when structurally flexible materials are applied.

Teufel et al. first reported deuterium separation by exploiting the locally flexible nature of Cl atoms included in MFU-4[10]. MFU-4 has bimodal pore structure in which small and large pores are connected by a square aperture of diameter 2.52 Å formed by four Cl atoms (Figure 2.2.3a). Owing to the gating behavior of the aperture caused by the phonon excitation of Cl atoms at aperture depending on the temperature, relatively large hydrogen and deuterium molecules (~2.82 Å) can diffuse into the MFU-4 and the quantum sieving separation occurred repeatedly at these narrow apertures during diffusion. The mixture selectivity of MFU-4 was directly measured by applying a 1:1 D_2/H_2 mixture to an ACTDS apparatus capable of controlling the exposure temperature, pressure, and time. Compared with the typical rigid porous frameworks with the highest selectivity at zero coverage pressure, the temperature-triggered aperture opening in MFU-4 resulted in a practical maximum selectivity of up to 7.5 at a relatively high pressure of 10 mbar at 60 K for an exposure time of 15 min.

Oh et al. also assessed the isotope separation ability by exploiting the flexible nature of pyridine molecules decorated in a 1D channel of COF-1[11]. They successfully incorporated pyridine molecules as flexible gates into the large channel (9 Å) of COF-1 through a post-synthetic modification and obtained a dense structure, py@COF-1 (Figure 2.2.3b). Interestingly, in the sorption isotherm measurements at low temperatures, the dense structure of Py@COF-1 showed large hysteresis owing to the slow diffusion of gas molecules through the dense pore, indicating the presence of a large diffusion barrier. Varying degrees of hysteresis with the change in exposure temperature implied the existence of a cryogenically flexible aperture, which was further supported by Raman studies of comparison between Py@COF-1 and pristine COF-1. As a result, the cryogenically flexible aperture enables highly selective quantum sieving of D_2 from a 1:1 H_2 /D_2 isotope mixture reaching a maximum selectivity of 9.7 at 26 mbar and 22 K. Studies using py@COF-1 with cryogenically flexible pyridine molecules demonstrated that the operating pressure can be further enhanced owing to the flexible nature of the porous frameworks.

In a recent study, Kim et al. reported an effective hydrogen isotope separation system by utilizing the large structure transition along the 1D channel triggered by molecular adsorption[12]. Accordingly, MIL-53(Al) was chosen as the host material, which shows reversible structure changes from narrow pore (*np*, 2.6 × 13.6 Å^2) to large pore (*lp*, 8.5 × 8.5 Å^2) in response to hydrogen adsorption. Considering the dynamic phase transition during the propagation of the phase transition from *np* to *lp*, the MIL-53(Al) can generate an intermediate pore size where the effective quantum sieving effect may occur (Figure 2.2.3c). When the pore structure of MIL-53(Al) was systematically tuned by the exposure temperatures (25, 40, 60, and 77 K) and exposed to 10 mbar of 1:1 D_2/H_2 mixture for 10 min, the highest selectivity ($S_{D2/H2}$ = 10.5) was observed at 40 K where the phase transition occurred. Further enhancement of separation performance was achieved when the structure was systematically tuned by pressure and time, resulting in the highest selectivity ($S_{D2/H2}$ = 13.6) with a large separation capacity of 2.9 mmol g^{-1}. This study showed that a flexible MOF could provide high separation efficiency at cryogenic condition and the additionally growing *lp* phase could store large amounts of isolated deuterium, rendering it suitable as a high-efficiency isotope separation system.

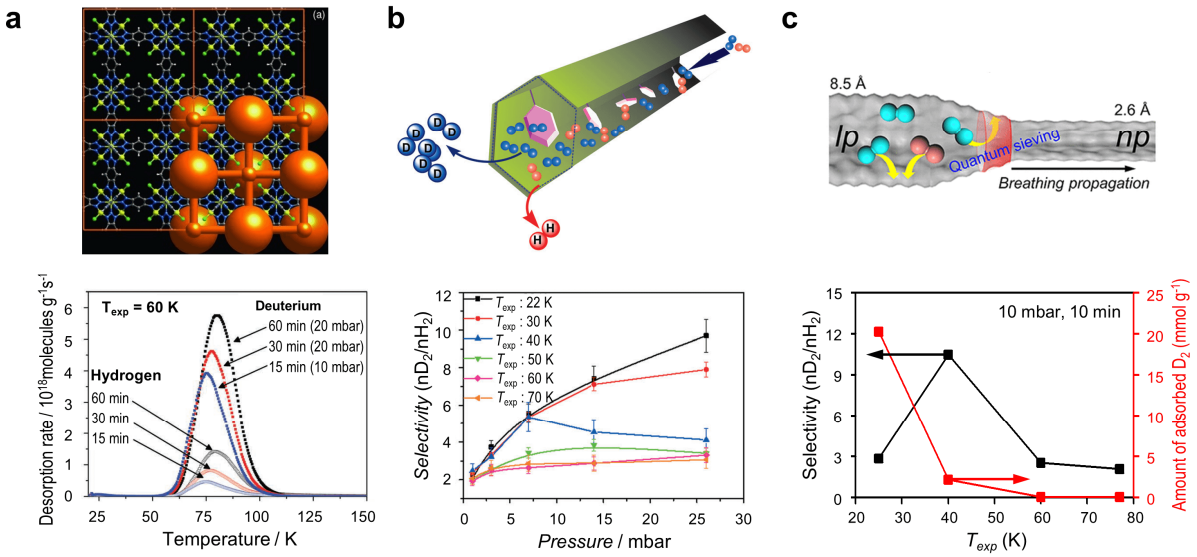

Figure 2.2.3 (a) Crystal structure of MFU-4 and its alternatively interconnected large and small pore structure, and thermal desorption spectra after exposing 1:1 mixture at 60 K for 15, 30, and 60 min. (b) Schematic view of the pore channel of COF-1 incorporated pyridine molecules in the pore walls, and 1:1 mixture selectivity as a function of loading pressure for different exposure temperatures (T_{ex}). Reproduced with permission. (c) Schematic view of D_2 separation in 1D channel of MIL-53 (Al) during the breathing propagation, and 1:1 mixture selectivity and D_2 uptake as a function of exposure temperature (T_{exp}).

2.2.4 Unsaturated Open Metal Site

To complement the limitation of KQS (superior separation performance only at cryogenic condition), CAQS was suggested, which can be implemented by introducing strong interactive sites into nanoporous materials. The different molecular masses of isotopes induce different adsorption enthalpies of the isotopes, resulting in preferential adsorption of heavier isotopes at stronger interaction sites. Several early hydrogen isotope separation studies have reported that heavy isotopes have stronger binding strength than light isotope molecules at binding sites[13,14]. In particular, FitzGerald et al. predicted for the first time that strong binding sites could be used for isotope separation because heavier isotope has a slightly larger adsorption enthalpy than hydrogen in the study of the interaction between H_2 and strong binding sites of the MOF-74 family[14].

FitzGerald's research group first investigated quantum sieving effects of strong binding sites in the series of MOF-74s, Fe-MOF-74, Co-MOF-74, and Ni-MOF-74, which have high-density exposed open metal sites on the 1D channel (10 Å)[15]. In all three cases, the isosteric heat of adsorption for D_2 at low loading, which represents the interaction at the open metal site, is greater than that of H_2, and the difference is enhanced as the metal sites exhibit stronger adsorption strengths. The difference is attributed to the ZPE of adsorbed isotope, confirmed via infrared measurement of H_2 adsorption on the metal center. Consequently, the IAST selectivities of 1:1 H_2/D_2 mixed gas were enhanced according to the adsorption strength of metal sites and they increased up to 5 at 77 K in the case of Ni-MOF-74; the IAST selectivities were maintained at a higher pressure compared with the calculated conventional nD_2/nH_2 ratio (Figure 2.2.4a). This not only reflects that D_2 selective adsorption at the strong binding sites is effective even at high temperatures, but also extends the separation pressure range so that MOF could be considered an attractive material in real separation systems.

Similarly, Oh et al. also studied hydrogen isotope separation on strong adsorption sites in a porous framework, CPO-27-Co (Co-MOF-74), while investigated the additional direct mixture selectivity by TDS even at much lower temperature between 20~70 K[16]. In pure gas H_2 and D_2 TDS measurements, the sequential desorption from a weak to strong adsorption site was observed; especially, at the open metal site, the high-temperature shift of the desorption maxima of D_2 compared with that of H_2 near 80 K indicated stronger interaction of D_2 over H_2 (Figure 2.2.4b). CPO-27-Co was systematically exposed to 1:1 H_2/D_2 mixture at 30 mbar over the temperature range 20–80 K to determine the effect of CAQS on the isotope separation at the strong binding sites. Below 50 K, the selectivity was less than 4 because adsorption occurred both at weak and strong binding sites. In contrast, the selectivity increased drastically at high temperatures, where adsorption occurred predominantly at strong binding sites, and the maximum selectivity was 11.8 at 60 K. The selectivity decreased to 6.3 at 80 K but still showed the high reported separation value at higher temperatures than that of liquid nitrogen (77 K). Furthermore,

CPO-27-Co showed very efficient enrichment performance—i.e., the D_2 content in the D_2/H_2 mixture increased from 5% to 95% within only 3 cycles at 80 K.

Savchenko et al. reported a sizeable CAQS effect in MFU-4*l*, a system free of open metal sites[17]. The MFU-4*l* is an extended structure of the MFU-4 type and has a large pore size of 9.1 Å, which renders it difficult to exhibit the KQS effect. The TDS results of MFU-4*l* exposed to a 1:1 H_2/D_2 mixture at 40 K and 10 mbar showed a high selectivity of 17 based on integrating the TDS signal from 50 to 75 K. Its selectivity is due to the small difference of ZPE of 0.6 kJ-mol between the adsorbed H_2 and D_2 at a temperature of approximately 50 K, i.e., the CAQS effect.

Based on previous findings, stronger binding energy sites, which selectively adsorb D_2 and further increase the separation temperature, result in a pronounced CAQS effect. Weinrauch et al. reported the capture of heavy isotopes from an isotropic mixture even at 100 K, via selective adsorption in Cu(I)-MFU-4l, which has strong Cu(I) sites with remarkably high binding energy (32 kJ mol^{-1})[18]. In such extremely strong binding sites in large pore MFU-4l, the adsorption mechanism at the Cu(I) sites is

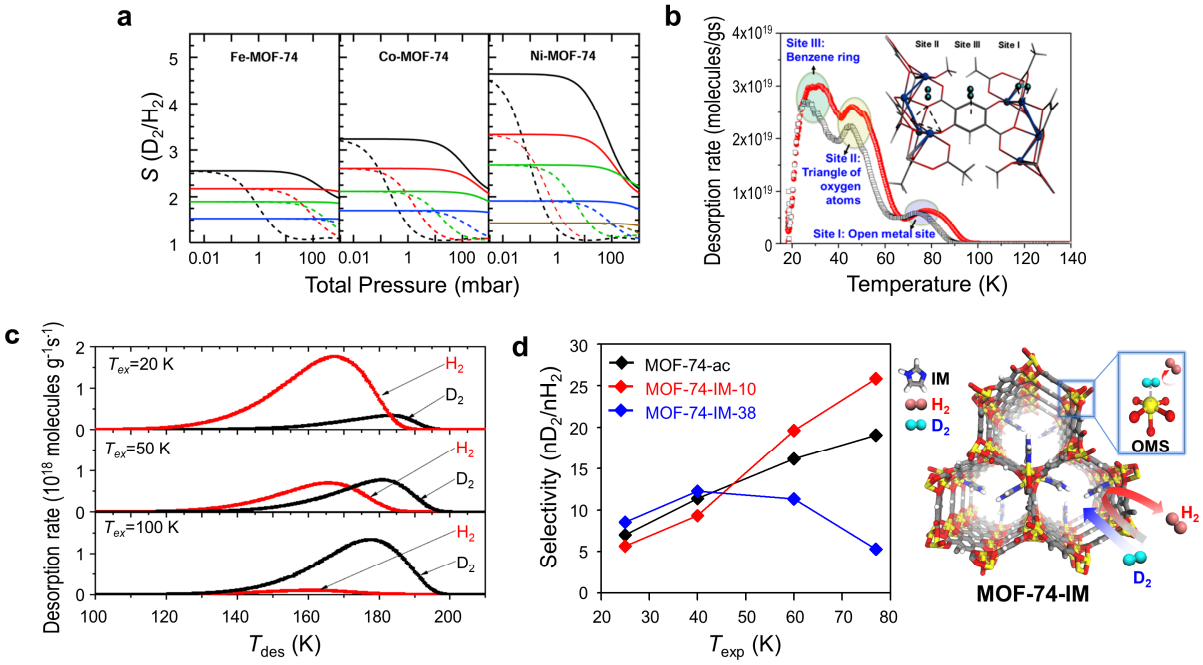

Figure 2.2.4 a) IAST selectivity (solid curve) and nD_2/nH_2 ratio (dashed line) of MOF-74 family at 77 (black), 87 (red), 100 (green), 120 (blue), and 150 K (brown). (b) Pure gas H_2 (open black circle) and D_2 (filled red circle) TDS spectra of CPO-27-Co. (c) TDS spectra of Cu(I)-MFU-4l after exposure to 10 mbar of 1:1 H_2/D_2 mixture at different exposure temperatures (T_{ex}) and showing the high-temperature range. (d) Selectivity of MOF-74-ac and MOF-74-IMs as a function of exposure temperature (T_{exp}) after exposing 1:1 H_2/D_2 mixture.

kinetically controlled at low temperature of 20 K so that the rapidly diffused H_2 (due to the absence of diffusion barrier under large pore) arrives first and binds firmly to the sites. Thus, such strong H_2-host interaction is preventing exchange with the slowly arriving D_2, resulting in low D_2 selectivity (Figure 2.2.4c). However, when the temperature rises above 90 K, the adsorption at Cu(I) sites is thermodynamically controlled to allow the selective capture of D_2, even though Cu(I) sites was already occupied by H_2. This exchange mechanism was observed in both TDS and inelastic neutron scattering (INS) measurements. At the Cu(I) site, D_2 and H_2 showed a large difference of adsorption enthalpy of 2.5 kJ mol^{-1}, and thus a remarkably high selective factor of 11 even at high temperature (100 K). In addition, a simulation study predicting the selectivity of various hydrogen isotopes (D_2/H_2, HD/H_2, DT/D_2, and T_2/D_2) at the Cu(I) sites suggests that MFU-4l is promising for the capture and purification of various isotope mixtures. Subsequently, Sharma et al. experimentally demonstrated that a large difference of heat of adsorption of VSB-15 between H_2 and D_2 (2 kJ mol^{-1}) could provide experimental selectivities above 4 even at the higher temperature of 140 K[19].

TDS (also called TPD) spectra have been widely used in isotope separation studies because they provide important information on specific adsorbate–adsorbent interactions such as the binding energy of the site and the adsorbed amount. Recently, FitzGerald et al. published TDS studies for isotope separation by combining simulations and experiments[20]. Their simulation result on D_2 enrichment factor showed a drastic increase in the separation factor by increasing the fractional difference in the binding energy rather than increasing the absolute binding energy. This is consistent with the results of Cu (I)-MFU-4l[18], and because the interaction strength between the strong binding site and the isotopes are absolutely high at cryogenic condition, possibly vanishing the fractional difference in the binding energy between two isotopes. By adjusting the temperature adaptably, hence, the fractional difference in binding energy between isotopes may be maximized, resulting in the efficient isotope separation at the strong binding site in the high-temperature environment.

Very recently, Kim et al. introduce a synergetic effects of two (kinetic and thermodynamic) quantum sieving merged in one system, namely an imidazole-coordinated MOF-74[21]. For this purpose, MOF-74-Ni was selected as a host material, in which open metal sites (OMSs) as strong adsorption sites are densely distributed in the 1D channels and potentially induce the strong CAQS effect. Simultaneously, a systematically controlled amount of imidazole molecules was bound to those Ni^{2+} OMSs (10, 38, and 70% of all OMSs, respectively) to reduce the effective aperture size and hinder H_2 diffusion through the channel repeatedly, which resulted in the KQS effect. The gas adsorption/desorption experiments on the MOF-74-IMs showed weak hysteresis loops, indicating the existence of KQS effect over the entire measured temperature range. However, increasing the imidazole amount diminishes the CAQS effect owing to the reduction of open metal sites. Thus, the optimization of the amount of imidazole was important to maximize the synergy of the two quantum effect, eventually showing highest

selectivity (ca. 26) even at high temperature (77 K) as well as high D_2 uptake (2.84 mmol g^{-1}) (Figure 2.2.4d). This study demonstrated the utility and effectiveness of the implementation of the two quantum sieving effects and provided experimental validation of this system as a practical strategy for industrial applications.

2.2.5 Reference

1. Oh, H.; Hirscher, M. *Eur. J. Inorg. Chem.* **2016**, 4278.
2. Garberoglio, G. *Chem. Phys. Lett.* **2009**, *467*, 270.
3. Liu, D.; Wang, W.; Mi, J.; Zhong, C.; Yang, Q.; Wu, D. *Ind. Eng. Chem. Res.* **2012**, *51*, 434.
4. Chen, B.; Zhao, X.; Putkham, A.; Hong, K.; Lobkovsky, E. B.; Hurtado, E. J.; Fletcher, A. J.; Thomas, K. M. *J. Am. Chem. Soc.* **2008**, *130*, 6411
5. Noguchi, D.; Tanaka, H.; Kondo, A.; Kajiro, H.; Noguchi, H.; Ohba, T.; Kanoh, H.; Kaneko, K. *J. Am. Chem. Soc.* **2008**, *130*, 6367.
6. Oh, H.; Park, K. S.; Kalidindi, S. B.; Fischer, R. A.; Hirscher, M. *J. Mater. Chem. A* **2013**, *1*, 3244.
7. Schneemann, A.; Bon, V.; Schwedler, I.; Senkovska, I.; Kaskel, S.; Fischer, R. A. *Chem. Soc. Rev.* **2014**, *43*, 6062.
8. Horike, S.; Shmomura, S.; Kitagawa, S. *Nat. Commun.* **2009**, *23*, 695.
9. Férey, G. *Chem. Soc. Rev.* **2008**, *37*, 191.
10. Teufel, J.; Oh, H.; Hirscher, M.; Wahiduzzaman, M.; Zhechkov, L.; Kuc, A.; Heine, T.; Denysenko, D.; Volkmer, D. *Adv. Mater.* **2013**, *25*, 635.
11. Oh, H.; Kalidindi, S. B.; Um, Y.; Bureekaew, S.; Schmid, R.; Fischer, R. A.; Hirscher, M. *Angew. Chem.* **2013**, *125*, 13461; *Angew. Chem., Int. Ed.* **2013**, *52*, 13219.
12. Kim, J. Y.; Zhang, L.; Balderas-Xicohténcatl, R.; Park, J.; Hirscher, M.; Moon, H. R.; Oh, H. *J. Am. Chem. Soc.* **2017**, *139*, 17743.
13. Chen, B.; Zhao, X.; Putkham, A.; Hong, K.; Lobkovsky, E. B.; Hurtado, E. J.; Fletcher, A. J.; Thomas, K. M. *J. Am. Chem. Soc.* **2008**, *130*, 6411.
14. FitzGerald, S. A.; Burkholder, B.; Friedman, M.; Hopkins, J. B.; Pierce, C. J.; Schloss, J. M.; Thompson, B.; Rowsell, J. L. C. *J. Am. Chem. Soc.* **2011**, *133*, 20310.
15. FitzGerald, A.; Pierce, C. J.; Rowsell, J. L. C.; Bloch, E. D.; Mason, J. A. *J. Am. Chem. Soc.* **2013**, *135*, 9458.
16. Oh, H.; Savchenko, I.; Mavrandonakis, A.; Heine, T.; Hirscher, M. *ACS Nano* **2014**, *8*, 761.
17. Savchenko, I.; Mavrandonakis, A.; Heine, T.; Oh, H.; Teufel, J.; Hirscher, M. *Microporous Mesoporous Mater.* **2015**, *216*, 133.

18. Weinrauch, I.; Savchenko, I.; Denysenko, D.; Souliou, S. M.; Kim, H.-H.; Le Tacon, M.; Daemen, L. L.; Cheng, Y.; Mavrandonakis, A.; Ramirez-Cuesta, A. J.; Volkmer, D.; Schütz, G.; Hirscher, M.; Heine, T. *Nat. Commun.* **2017**, *8*, 14496

19. Sharma, A.; Lawler, K. V.; Wolffis, J. J.; Eckdahl, C. T.; McDonald, C. S.; Rowsell, J. L. C.; FitzGerald, S. A.; Forster, P. M. *Langmuir* **2017**, *33*, 14586.

20. Fitzgerald, S. A.; Shinbrough, K.; Rigdon, K. H.; Rowsell, J. L. C.; Kapelewski, M. T.; Pang, S. H.; Lawler, K. V.; Forster, P. M. *J. Phys. Chem. C* **2018**, *122*, 1995.

21. Kim, J. Y.; Balderas-Xicohténcatl, R.; Zhang, L.; Kang, S. G.; Hirscher, M.; Oh, H.; Moon, H. R. *J. Am. Chem. Soc.* **2017**, *139*, 15135.

2.3 Selective Hydrogen Isotope Separation via Breathing Transition in MIL-53(Al)

2.3.1 Introduction

Structural flexibility is a unique property of some metal–organic frameworks (MOFs) that clearly distinguishes them from other inorganic porous materials such as zeolite and porous silica.[1-3] This interesting property is the result of the detectable changes in local or overall structural properties in response to external stimuli (e.g., heat, pressure, and presence of guest molecules).[4-6] The smart response enables many possible applications in various fields for flexible MOFs.[7-9] In particular, upon exposure of a MOF to specific adsorbates, large changes in the unit cell parameters are manifested as expansion and contraction, an effect called breathing, and this effect has attracted the attention of many researchers in the field of separation and sorption.[10,11] For example, MIL-53 family, the most studied flexible MOFs, has demonstrated selective separation of specific molecules such as CO_2 over that of N_2 or CH_4, *o*-xylene over xylene isomers, and acidic gases over CH_4.[12-15] In these cases, the efficient separation can be attributed to the chemical affinity between the inner surface of MIL-53 and the adsorbates, as well as the size selectivity of adsorbates through the aperture of narrow pore (*np*) or large pore (*lp*). This observation initiated many theoretical and experimental investigations to gain a deeper understanding of the breathing mechanism between the *np* and *lp* phases of the MIL-53 system.[16-24] However, these studies overlooked the dynamic pore changes, which ought to occur during the *np*-to-*lp* phase transition. Even though there is not enough direct structural information on this transitional state, it has been generally agreed that molecular adsorption on the pore surfaces triggers breathing along the one-dimensional (1D) channel, resulting in dynamic changes in the pore diameter during the transitional state between two structural phases. This phenomenon of dynamic change in pore aperture can be applied to the separation of gas mixtures containing molecules of similar size and shape, which means it would entail fine pore-tuning, as required for the separation of hydrogen isotopes.

Hydrogen isotope separation through the use of porous materials was previously studied based on a quantum sieving (QS) effect, in which D_2, which has a shorter de Broglie wavelength than H_2, can diffuse faster through the confined pore at a cryogenic temperature.[25-30] Chen *et al*. suggested the sorption of H_2 and D_2 within <6 Å pores at 77 K involve quantum effects, and experimentally observed the optimal pore diameter was around 3.0–3.4 Å for rigid structures.[29,30] According to previously studied separation strategies, the MIL-53 system may not appear to be suitable for hydrogen isotope separation because the aperture of the *lp* phase (8.5 × 8.5 $Å^2$) is too large for selective QS, while the narrow aperture of the *np* phase (2.6 × 13.6 $Å^2$) can only accommodate a negligible amount of adsorbed particles. Taking into account the dynamic pore change, however, MIL-53(Al) certainly generate an intermediate pore size during the propagation of the phase transition from *np* to *lp*, i.e., breathing along the 1D channel. This intermediate pore size by working at given temperature and pressure may create an optimal

energetic interaction between D_2 and the framework while for H_2 the interaction is still weak. The dynamically moving aperture will maximize the QS effect and additionally the growing *lp* phase will offer a large storage capacity (Figure 2.3.1). Thus, the dynamic pore system and large increase in storage volume make flexible MOF systems excellent candidates for effective hydrogen isotope separation.

Herein, we report a novel strategy for efficient separation of hydrogen isotopes, exploiting the dynamic pore change during the breathing of a flexible MOF, MIL-53(Al). We evaluated the effect of the breathing phenomenon on QS as a function of the exposure temperature, pressure, and time. To the best of our knowledge, this is the first attempt to exploit the structural flexibility of MOFs caused by the breathing phenomenon for hydrogen isotope separation. In order to evaluate the separation efficiency, we utilized a laboratory-designed advanced cryogenic thermal-desorption spectroscope (TDS) for direct measurement of the selectivity for the hydrogen isotope mixture. On the basis of our results, we demonstrated the potential of the dynamic flexibility of MIL-53(Al) for efficient isotope separation.

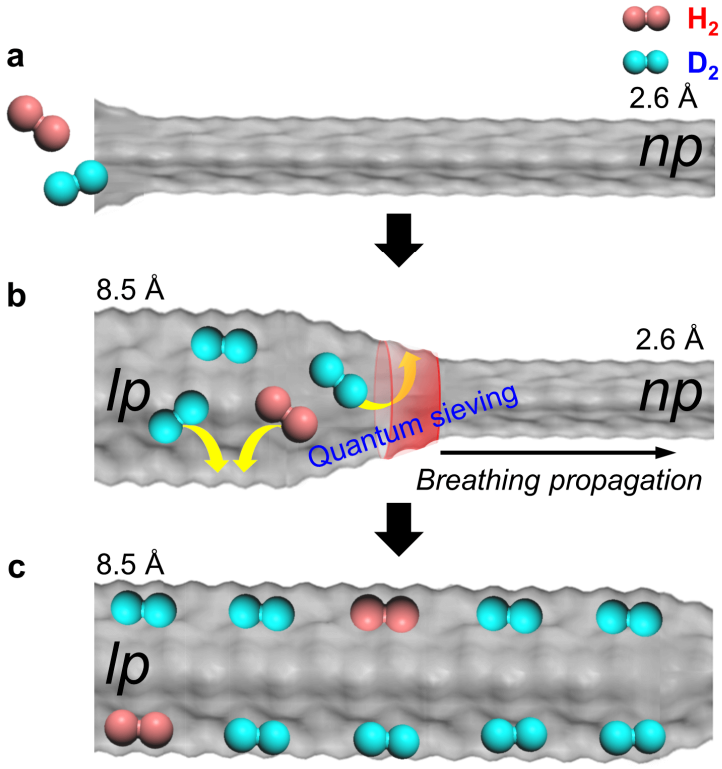

Figure 2.3.1 Schematic view of D_2 separation in breathing propagation along the 1D channel in MIL-53(Al).

2.3.2 Experimental Section

All chemicals and solvents were of reagent grade and used without further purification.

Synthesis of MIL-53(Al). MIL-53(Al) was prepared according to the previously reported method.[31] To aqueous solution (5 mL) of $Al(NO_3)_3 \cdot 9H_2O$ (1.30 g, 3.47 mmol), terephthalic acid (0.29 g, 1.73 mmol) was added. The white suspension was heated to 220 ^oC for 3 days. The white powder was collected by centrifugation and washed with H_2O and dimethylformamide (DMF), respectively. The terephthalic acid trapped in the pore was exchanged by DMF at 150 ^oC for 15 h. The DMF was removed by heating at 280 ^oC in air for 12 h in muffle furnace. FT-IR (ATR, cm^{-1}): ν_{O-H} = 3604(s), $\nu_{O-H(H2O)}$ = 3425, $\nu_{O-C=O(carboxylate,\ asym)}$ = 1574(s), $\nu_{O-C=O(carboxylate,\ sym)}$ = 1406(s)

Materials and characterization. Infrared (IR) spectra were recorded with a ThermoFisher Scientific Nicolet 6700 FT-IR spectrometer. X-ray powder diffraction data were collected on a Bruker D8 advance diffractometer at 40 kV and 40 mA for Cu Kα (λ = 1.54050 Å), with a step size of 0.02° in 2θ. The nitrogen adsorption-desorption isotherm was obtained using a BELSORP-max at 77 K. Prior to the adsorption measurements, the sample (ca. 100 mg) was evacuated ($p < 10^{-5}$ mbar) at 403 K for 12 h. The low pressure hydrogen adsorption isotherms of MIL-53(Al) were measured at 20 K, 40 K and 77 K by full automated Quantachrome Autosorb-iQ with controlled cryocooler. MIL-53(Al) (ca. 70 mg) were activated under ultra-high vacuum at 403 K for 12 h prior to each measurement. The high pressure hydrogen isotherm of MIL-53(Al) was measured at 77 K and 87 K by the automated Sievert's type apparatus (PCTPro-2000). Before the hydrogen-uptake measurements, the samples were heated at 403 K in vacuum (4.5×10^{-9} bar) for 12 h in order to remove any guest molecules in frameworks.

TDS studies for H_2 and D_2. A set up of laboratory-designed advanced cryogenic thermal desorption spectroscopy (TDS) is previously described in details.[32,33] MIL-53(Al) activated at 403 K, 12 h. For the pure gas thermal desorption experiment, the sample is exposed to pure D_2 or H_2 atmosphere (10 mbar) at RT. Afterwards, the sample is rapidly cooled to the boiling temperature of the adsorbed gas, and the gas molecules that had not been adsorbed were pumped off. Finally, a linear heating ramp (0.1 K s^{-1}) is applied. In case of the D_2–H_2 mixture thermal desorption experiments, the sample was exposed to a 10 mbar 1:1 D_2–H_2 mixture at the given exposure temperatures at 25 K, 40 K, 60 K and 77 K for 10 min. After 10 min, the gas molecules that had not been adsorbed were mildly pumped off until HV is reached again. Afterwards, the sample chamber was cooled quickly down to below 20 K. For desorption, the sample was heated with a rate of 0.1 K s^{-1} from 20 K to 150 K and the desorbing gas was continuously detected by a quadrupole mass spectrometer. In order to quantify the mass spectrometer signal, the TDS device had been calibrated by a hydrogen/deuterium loaded $Pd_{95}Ce_5$ alloy.

The calibration procedure was performed as follows;

(1) The $Pd_{95}Ce_5$ alloy was etched prior to the calibration procedure by aqua regia (nitric acid hydrochloride: HNO_3+3HCl). (2) To remove any hydrogen introduced during the acid treatment and to avoid any oxidation, the $Pd_{95}Ce_5$ alloy was annealed by ramping from RT to 600 K, 0.1 K/s under UHV. (3) Weigh the $Pd_{95}Ce_5$ alloy and then be loaded it in the TDS sample chamber (4) Expose to pure H_2 or D_2 atmosphere (150 mbar) at 350 K for 2 h. (5) After 2 h gas loading, cool the sample to RT by using either air-cooled or liquid N_2. (6) Take out the $Pd_{95}Ce_5$ alloy from the chamber and weigh again. After weighing, the alloy is loaded in the chamber again. The mass difference before and after loading is equal to the amount of gas that was taken up by the alloy. (7) Subsequently a desorption spectrum from RT to 600 K was recorded with a heating rate of 0.1 K. (8) In order to obtain reliable data, the step 3 to 7 should be repeated at least 5 times. The area under the desorption peak is directly proportional to the amount of gas, which has been determined by the weight change due to gas loading. The average of several runs with H_2 and D_2 yields calibration constants for the mass spectrometer channels *m/z* = 2 and *m/z* = 4, respectively.

Heat of adsorption calculation. The hydrogen heat of adsorption of MIL-53(Al) can be determined by an integration of the Clausius-Clapeyron equation as function of the surface coverage. Carrying out the integration, the Claudius-Clapeyron relation is now commonly rearranged in the Van't Hoff form for calculating physisorption enthalpy.

$$\Delta H = R \cdot \left(\frac{\partial \ln(P)}{\partial \frac{1}{T}} \right)_{\theta}$$

where P is the equilibrium gas pressure, ΔH the reaction enthalpy and θ is the surface coverage.

From the 'absolute adsorption isotherms' for 77 K and 87 K, the logarithm of the pressures values at a fixed surface coverage θ can be plotted versus the reciprocal temperature 1/T yielding a linear correlation with a slope proportional to the enthalpy of adsorption.

2.3.3 Results and Discussion

The MIL-53(Al) sample was successfully synthesized by following the procedures for previously reported methods, as illustrated in Figures 2.3.2-2.3.4.[31] The X-ray powder diffraction (XRPD) pattern of MIL-53(Al) matches the simulated pattern, indicating the formation of pure-phase MIL-53(Al), and the Fourier transform infrared (FT-IR) spectrum of MIL-53(Al) confirms the complete removal of unreacted terephthalic acid within the pores (Figures 2.3.2 and 2.3.3). The Brunauer–Emmett–Teller (BET) surface area calculated from N_2 sorption measurement is 1424 m^2 g^{-1} (Figure 2.3.4), which is good agreement with values reported in the literature.[5,34]

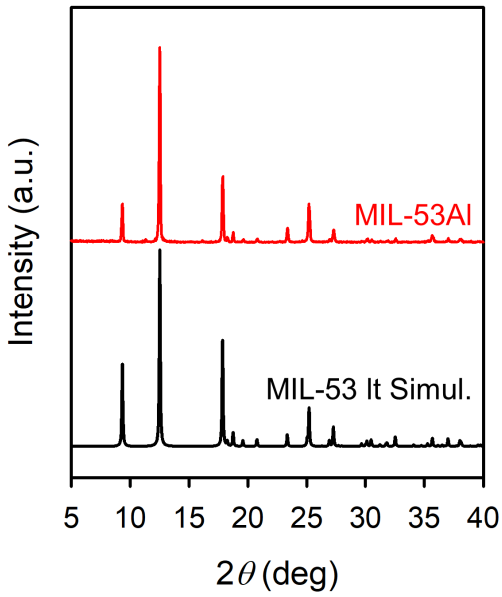

Figure 2.3.2 XRPD patterns of MIL-53(Al) with the simulated XRPD patterns taken from reference 21.

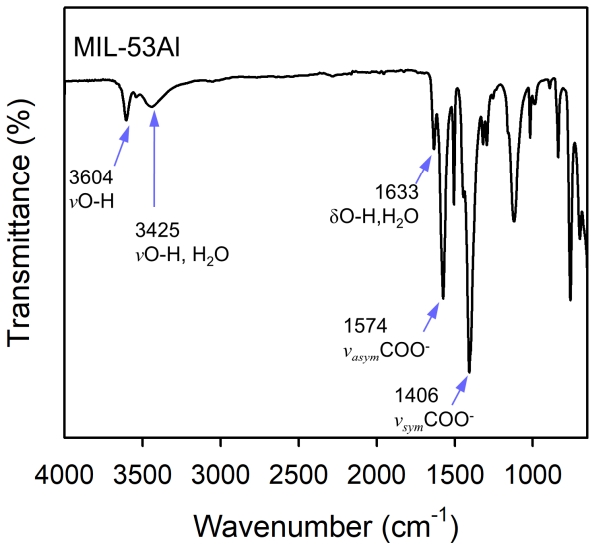

Figure 2.3.3 FT-IR spectrum of MIL-53(Al).

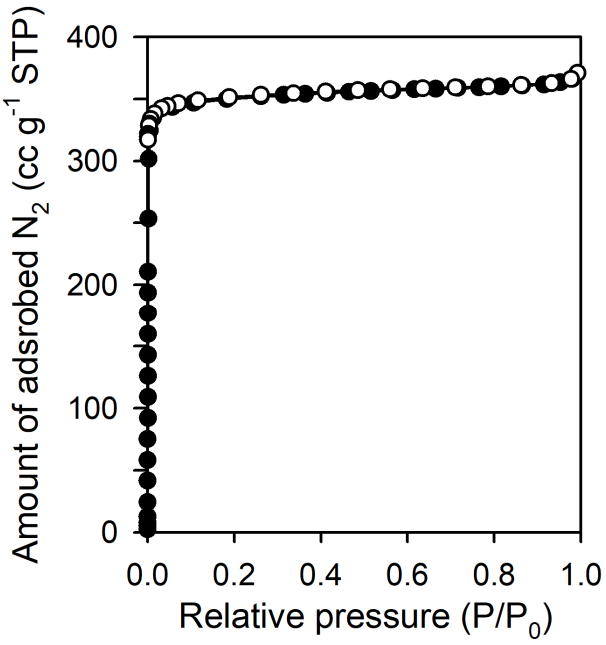

Figure 2.3.4 Isotherm of N_2 sorption on MIL-53(Al) measured at 77 K.

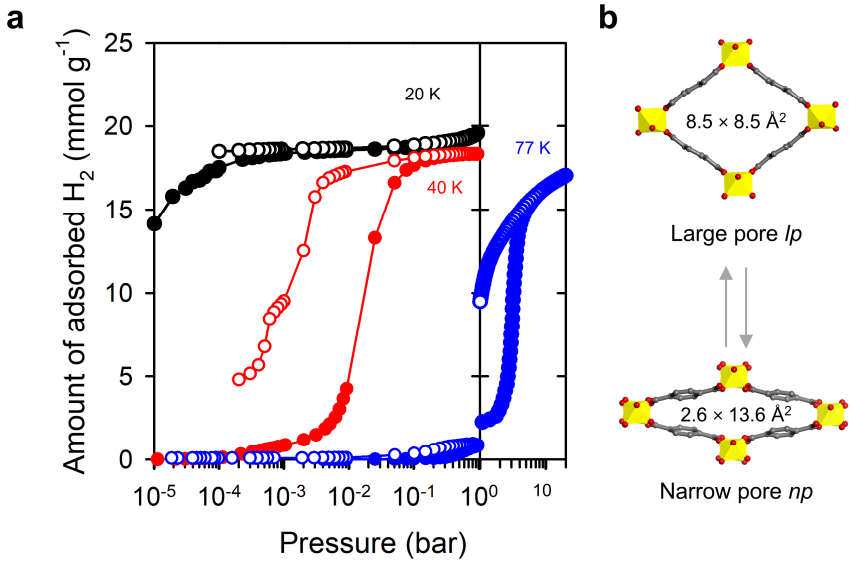

Figure 2.3.5 (a) Isotherms of H_2 sorption on MIL-53(Al) measured at 20 K (black symbols), 40 K (red symbols), and 77 K (blue symbols), with the pressure shown in logarithmic scale. (b) Structural view of a large pore (*lp*) and a narrow pore (*np*) in MIL-53(Al) along the channel direction. Note: The H_2 sorption isotherms from 1 to 20 bar at 77 K were measured by a high-pressure sorption device (PCTPro-2000).

In Figure 2.3.5, the H_2 sorption isotherms obtained at 20, 40, and 77 K clearly show the flexibility of MIL-53(Al). Under vacuum and cryogenic conditions, the activated MIL-53(Al) formed *np*,[5] resulting in no H_2 adsorption, as shown in the initial portion of the H_2 sorption isotherms. However, as the pressure increased, H_2 adsorption induced the breathing phenomenon, leading to continuous phase changing to *lp* structure[35] that could adsorb a large amount of H_2 (maximum capacity: 20 mmol g^{-1}). The large increase in the amount of adsorbed H_2 due to breathing proves that MIL-53(Al) is an excellent system that can provide a large storage capacity with flexibility. Owing to the structural flexibility, the breathing pressure changed with exposure temperature: ~3 bar at 77 K, ~10^{-2} bar at 40 K, and <10^{-5} bar at 20 K. This phenomenon is related to the simple thermodynamic effect explained using P-T phase diagrams of pure gas (e.g. N_2, H_2, Xe) adsorption on flexible MOFs. A very similar model has been used already by Springuel-Huet *et al.*.[16] to explain the Xe adsorption behaviour in MIL-53 observed by ^{129}Xe NMR spectroscopy. These results suggest that the breathing phenomenon of MIL-53(Al) can be systematically tuned by controlling the applied gas pressure or the exposure temperature.

In order to identify the preferred H_2 and D_2 adsorption sites in breathing MOFs, the advanced cryogenic TDS measurements were made after exposure to a pure H_2 and D_2 atmosphere, respectively, under identical conditions (Figure 2.3.6). The MIL-53(Al) sample was exposed to 10 mbar of pure H_2 or D_2 at 20 K for 10 min. Afterwards, the remaining gas molecules in the sample chamber were evacuated until a high vacuum was reached, before the sample was heated to 180 K at a linear ramp rate of 0.1 K s^{-1} and the desorbed gas molecules were continuously monitored by a quadrupole mass spectrometer. During the TDS measurements, the desorption maxima of adsorbed gas occur typically moved from weak to strong adsorption sites with increasing temperature. MIL-53(Al) possesses four energetically different sorption sites, where site I is the benzene ring, and sites II, III, and IV are close to the AlO_6 cluster (Figure 2.3.7), as reported in the literature.[35] However, only one desorption maximum appears at *ca.* 40 K in both H_2 and D_2 desorption spectra (Figure 2.3.6), which can be explained by one of three possible scenarios: (1) the very similar binding strengths of sites I to IV led to an overlap of the desorption peaks; (2) there was only one continuous process of gas release because the pore apertures contracted from both ends of the channels during desorption and the simultaneous phase transition[16]; (3) a combination of (1) and (2). Almost all gas was desorbed at temperatures below 60 K for both H_2 and D_2, indicating the absence of any strong binding sites. This also coincided with the low isosteric heat of adsorption (4–6 kJ mol^{-1}) of MIL-53(Al) (Figure 2.3.8), which clearly implies that the isotope separation may have been mainly governed by the flexible aperture, rather than the difference in chemical affinity between the hydrogen isotopes and host material. It should be noted that as shown in Figure 2.3.6, a trace amount of gas desorption still occurred at temperatures above 60 K owing to the kinetically trapped gas in closed channels, which confirms the earlier results of neutron diffraction and DFT calculations.[35] To ascertain the ability of the flexible MOF to separate D_2 in isotope mixtures, we

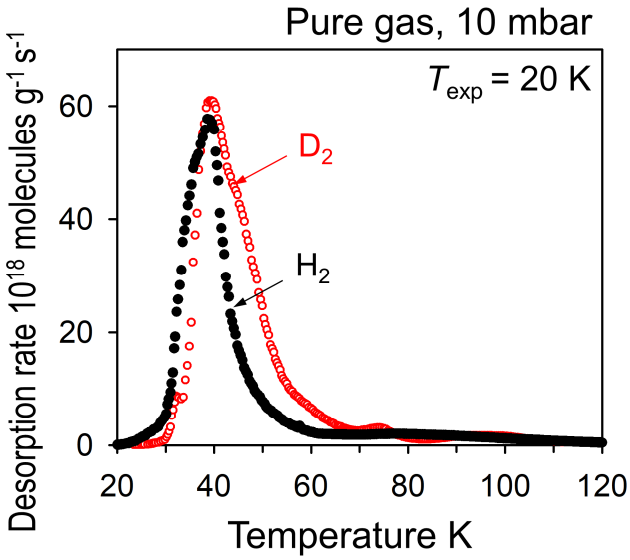

Figure 2.3.6 Thermal desorption spectra (TDS) of pure H_2 gas (black filled symbols) and D_2 (red open symbols) from MIL-53(Al) exposed at 10 mbar and an exposure temperature (T_{exp}) of 20 K

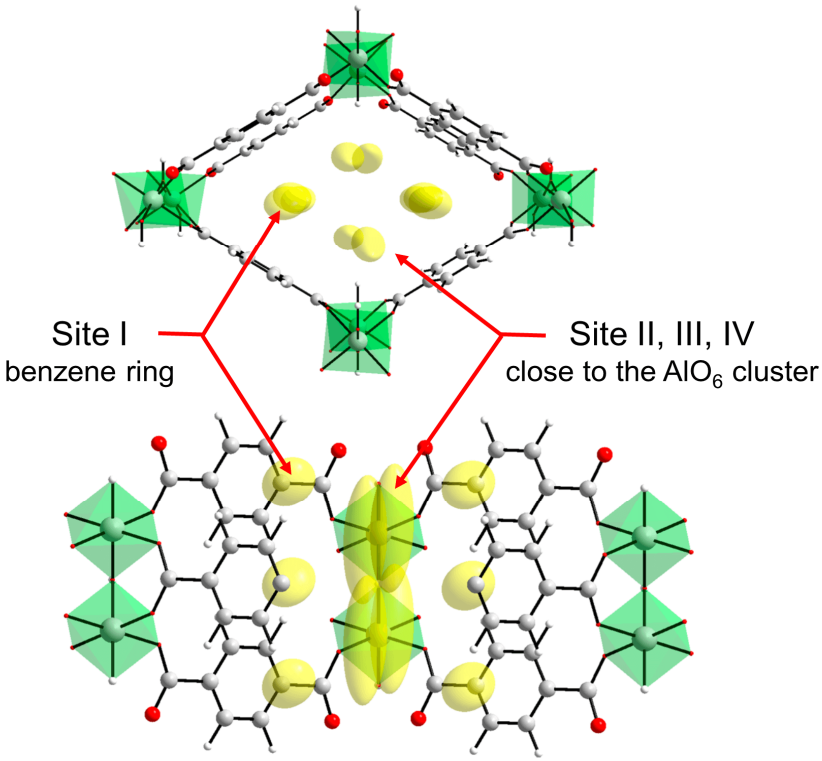

Figure 2.3.7 D_2 sorption sites of MIL-53(Al). Adapted with permission from reference 35. Copyright 2014 American Chemical Society.

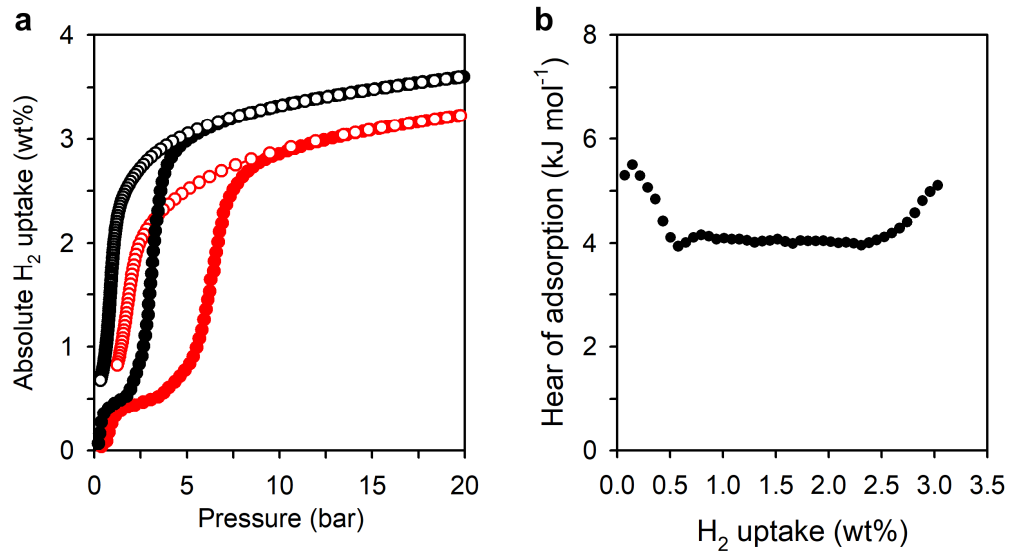

Figure 2.3.8 (a) High pressure isotherm of H_2 sorption on MIL-53(Al) measured at 77 K (black) and 87 K (red), and (b) isosteric heat of adsorption of MIL-53(Al) obtained from high pressure H_2 sorption isotherm at 77K and 87K.

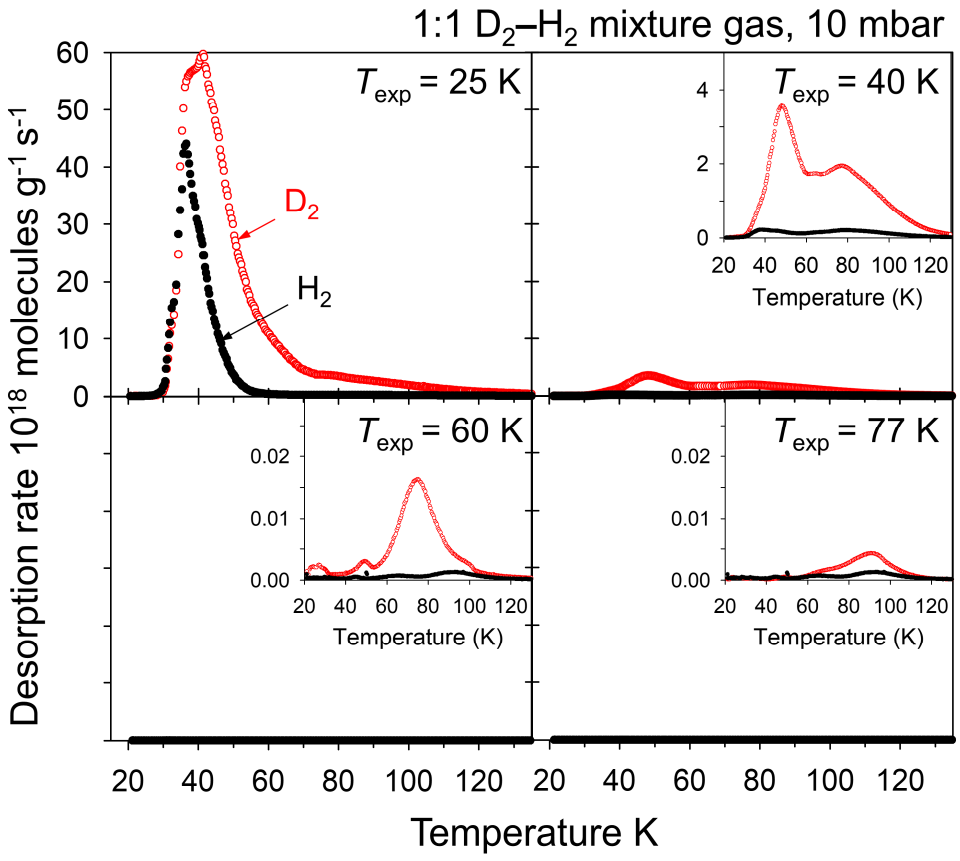

Figure 2.3.9 TDS of 1:1 D_2–H_2 mixed gas from MIL-53(Al) exposed at 10 mbar and T_{exp} of 25, 40, 60, and 77 K; the insets show close-ups of the spectra in the low-desorption rate region.

carried out TDS measurements after exposure of the MIL-53(Al) sample to 10 mbar of a 1:1 D_2–H_2 isotope mixture at different exposure temperatures (T_{exp}) of 25, 40, 60, and 77 K (Figure 2.3.9). The area under the desorption peak is related to the amount of desorbed gas molecules, which can be quantified with careful calibration[36] (against the $Pd_{95}Ce_5$ alloy, see experimental section), and the selectivity for D_2 over H_2 could be directly calculated from the ratio of the peak areas[27,37].

The exposure pressure of 10 mbar for the TDS experiments was a meaningful criterion because as shown in the H_2 sorption isotherms (Figure 2.3.10), it belonged to three individual stages of the transition of MIL-53 during breathing: before breathing at 77 K; in the intermediate states of breathing at 40 K; after breathing at 20 K. Thus, the TDS results obtained at the relevant temperatures could offer information of selective adsorption of H_2 and D_2 during dynamic changes in the pore aperture. Figure 2.3.11a and Table 2.3.1 shows the selectivity of D_2 over H_2 and the total D_2 uptake as a function of T_{exp}. The D_2 uptake decreased with increasing T_{exp}; however, the selectivity exhibited a maximum, where $S_{D2/H2}$ = 10.5, at T_{exp} = 40 K, before it decreased below the initial selectivity (at T_{exp} = 25 K) when T_{exp} = 60 and 77 K. This unique behavior of MIL-53(Al) can be attributed to its structural flexibility. Once the pores are completely opened by high gas loading (T_{exp} = 25 K), the aperture of the *lp* phase is too large for effective QS and both D_2 and H_2 are adsorbed on the newly generated accessible surface, resulting in the low overall selectivity. When T_{exp} > 60 K at 10 mbar, MIL-53(Al) remains in the *np* phase, resulting in negligible adsorption and thus low selectivity. At T_{exp} = 40 K the breathing process takes place at about 10 mbar and the *np*–*lp* phase transition in MIL-53(Al) occurs by a change of aperture size moving along the channel. The continuously opening aperture will first create an optimal interaction for D_2 possessing the smaller de Broglie wave length, while H_2 is still too large to penetrate effectively. In total, this leads to the observed high selectivity in this temperature and pressure window.

Since the breathing process depended on T_{exp} and the exposure pressure (P_{exp}) of the gas, it could be systematically tuned to further investigate its effect on QS (Figure 2.3.11b). For this study, T_{exp} was set to a constant value of 40 K, at which the transition upon breathing was clearly observed. As P_{exp} was increased from 5 to 80 mbar, the selectivity decreased from 11.6 to 6.4, while the D_2 uptake was significantly enhanced from 0.87 to 8.6 mmol g^{-1} (Figures 2.3.11b, 2.3.12, and Table 2.3.2). At low pressure (P_{exp} = 5 mbar), the pore aperture was nearly closed, thus producing a strong penetration or diffusion barrier (and consequently a very small gas loading) and D_2 could preferentially penetrate because its zero-point energy is lower than that of H_2, resulting in high selectivity. When P_{exp} was increased to 80 mbar, the selectivity decreased soon afterwards owing to the higher accessibility of H_2, as shown in Figure S7. Nonetheless, at 80 mbar, the significantly increased amount of adsorbed gas (approximately tenfold) with moderate selectivity (8.6 mmol g^{-1} with $S_{D2/H2}$ of 6.4) was still impressive and considerably larger than the highest separation capacity with selectivity similar to those of a

previously reported MOF, MFU-4 (1.26 mmol g^{-1} with $S_{D2/H2}$ 7.5), a rigid porous structure with only flexible apertures.[26]

Since the adsorption process required time to reach equilibrium, the isotope selectivity could have been time-dependent in the region of the breathing transition, i.e., during the dynamic changes in pore aperture change. Figure 3d shows the selectivity and gas uptake as functions of the exposure time (t_{exp}). In general, the kinetic QS effect and the selectivity decrease with time until the gas uptake is fully saturated.[26] However, for MIL-53(Al) at 40 K and 10 mbar, increasing t_{exp} from 10 to 120 min led to increases in gas uptake and selectivity from 2.3 to 2.9 mmol g^{-1} and $S_{D2/H2}$ = 10.5 to $S_{D2/H2}$ = 13.6, respectively (Figures 2.3.11c, 2.3.13, and Table 2.3.3). The applied P_{exp} led to a partial gas loading and an intermediate state of the flexible framework. The gas loading was approximately 12–15% (2.3–2.9 mmol g^{-1}) of the saturation uptake of ~20 mmol g^{-1}, and it may have induced just the optimum dynamic opening of the pores during the phase transition, leading to effective QS. Meanwhile, the remaining *np* phase had an opening of only 2.6 Å in one dimension, thus preventing gas from penetrating the pores. With increasing t_{exp}, breathing propagation continued to occur, even at the same P_{exp}, to generate the optimum pore size required for QS through the dynamic changes in pore aperture. As a result, along with the increase in D_2 uptake, $S_{D2/H2}$ was enhanced.

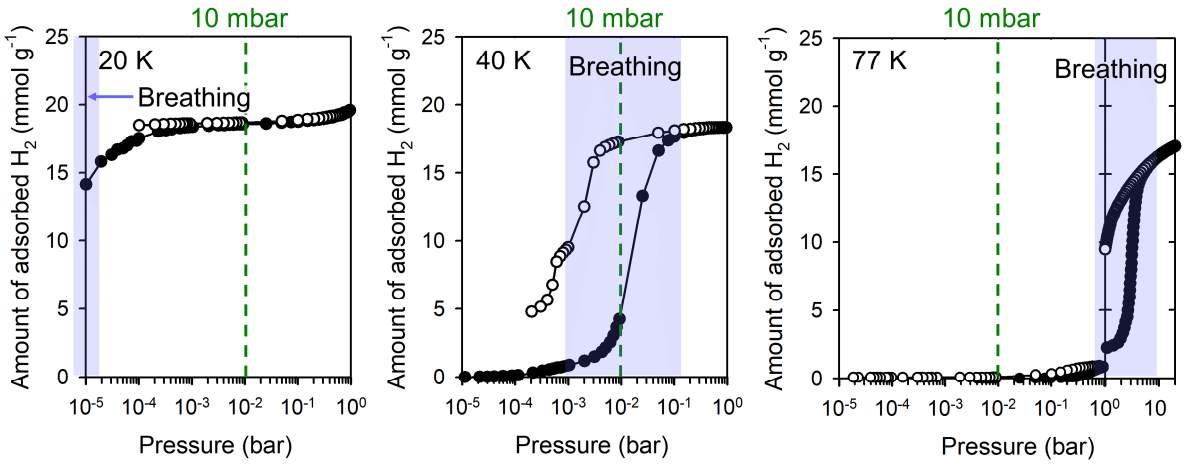

Figure 2.3.10 Isotherms of H_2 on MIL-53 at 20, 40, and 77 K. The green vertical dotted lines indicate the points at which the pressure was 10 mbar, which was the exposure-mixture pressure for the TDS measurements.

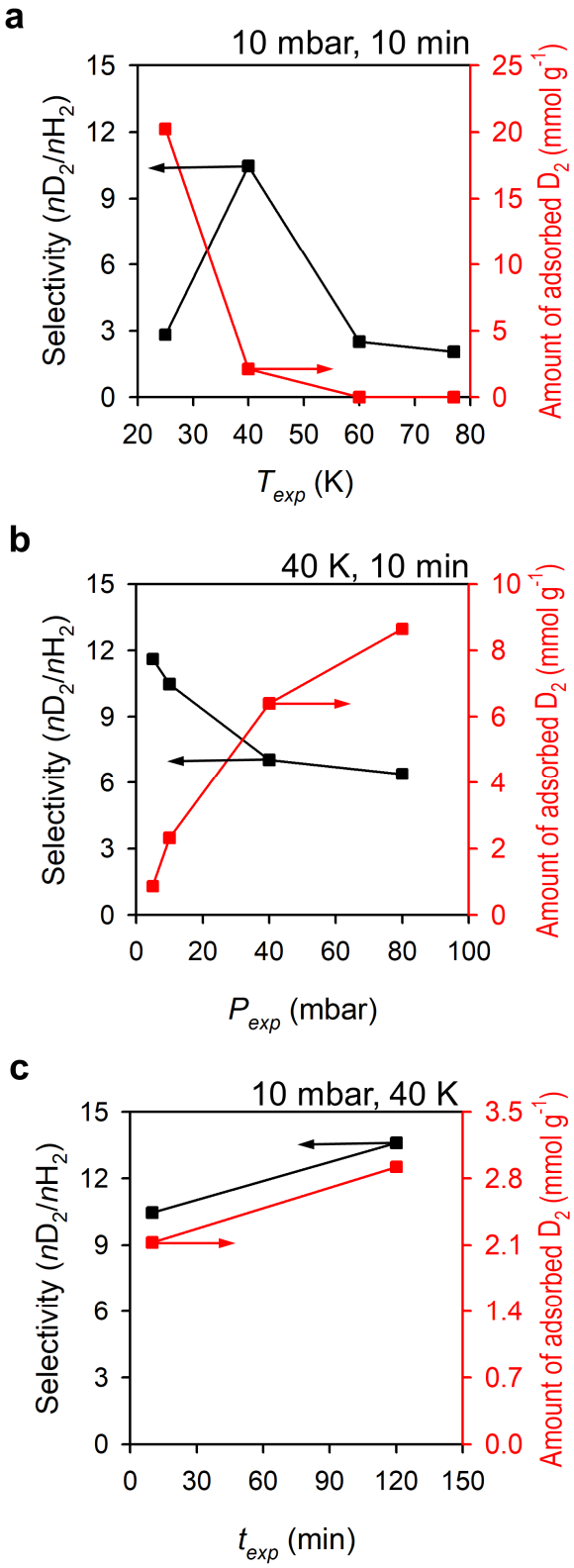

Figure 2.3.11 The selectivity (black symbols) and the corresponding amount of adsorbed D_2 (red symbols) as functions of (a) exposure temperature (T_{exp}), (b) exposure pressure (P_{exp}), and (c) exposure time (t_{exp}).

Table 2.3.1 Separation performance of the 1:1 D_2–H_2 mixture gas depended on exposure temperature (T_{exp})[a].

T_{exp} (K)	Adsorbed D_2 amount (mmol g^{-1})	Adsorbed H_2 amount (mmol g^{-1})	$S_{D2/H2}$
25	22.1	7.81	2.83
40	2.32	0.221	10.5
60	0.00741	0.00297	2.49
77	0.00230	0.00112	2.05

[a] Exposed at 10 mbar of 1:1 D_2–H_2 mixture gas and target exposure temperature (T_{exp}) for 10 min.

Table 2.3.2 Separation performance of the 1:1 D_2–H_2 mixture gas depended on exposure pressure (P_{exp})[a].

P_{exp} (mbar)	Adsorbed D_2 amount (mmol g^{-1})	Adsorbed H_2 amount (mmol g^{-1})	$S_{D2/H2}$
5	0.867	0.0746	11.6
10	2.32	0.222	10.5
40	6.40	0.909	7.04
80	8.65	1.35	6.41

[a] Exposed at target exposure pressure (P_{exp}) of 1:1 D_2–H_2 mixture gas and 40 K for 10 min.

Table 2.3.3 Separation performance of the 1:1 D_2–H_2 mixture gas depended on exposure time (t_{exp})[a].

t_{exp} (min)	Adsorbed D_2 amount (mmol g^{-1})	Adsorbed H_2 amount (mmol g^{-1})	$S_{D2/H2}$
10	2.32	0.222	10.5
120	2.92	0.215	13.6

[a] Exposed at 10 mbar of 1:1 D_2–H_2 mixture gas and 40 K for target exposure time (t_{exp}).

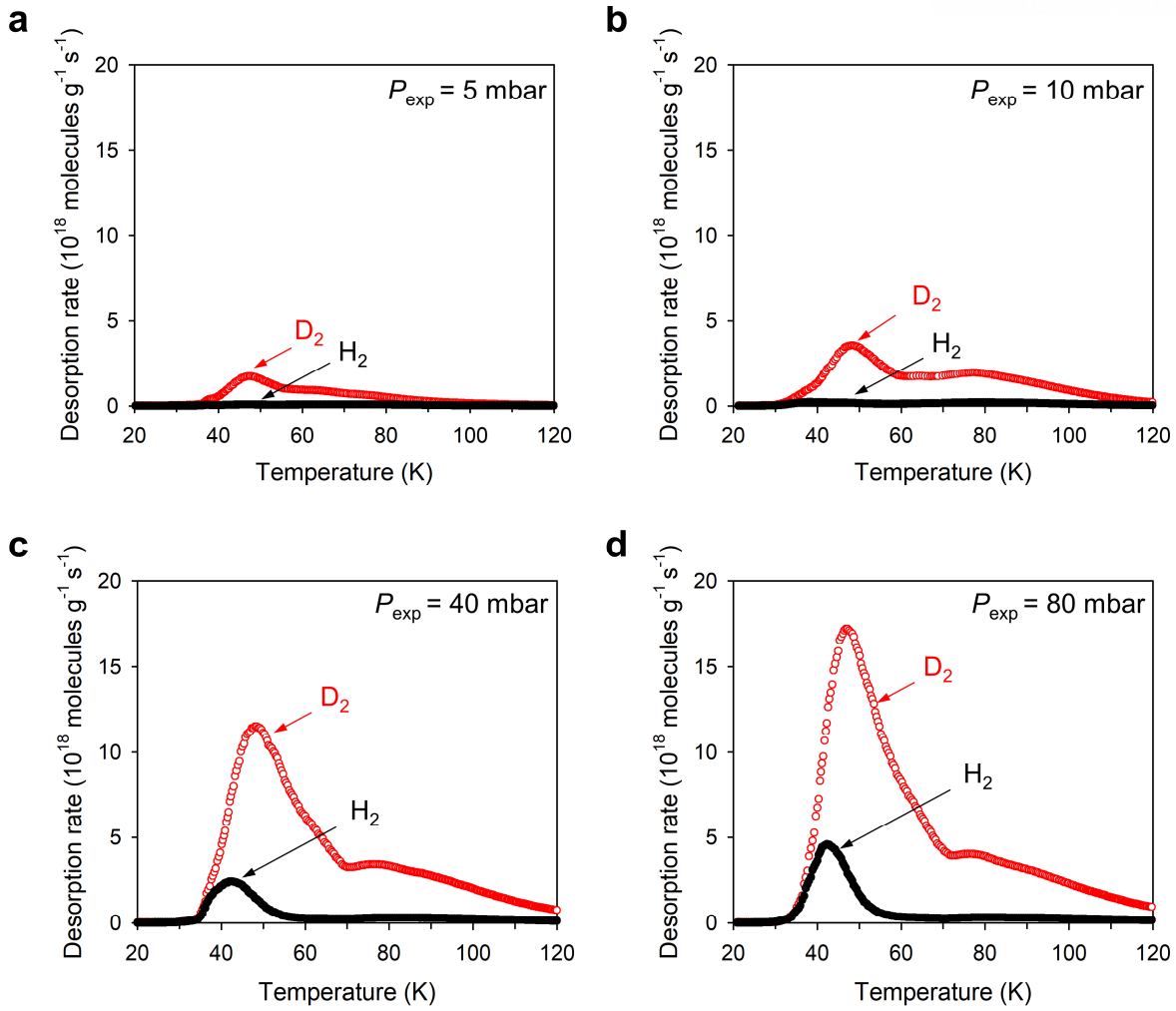

Figure 2.3.12 Thermal desorption spectra of mixture gas (1:1 H_2–D_2 mixture) at 40 K as a function of exposure pressure (a) 5 mbar, (b) 10 mbar, (c) 40 mbar, and (d) 80 mbar.

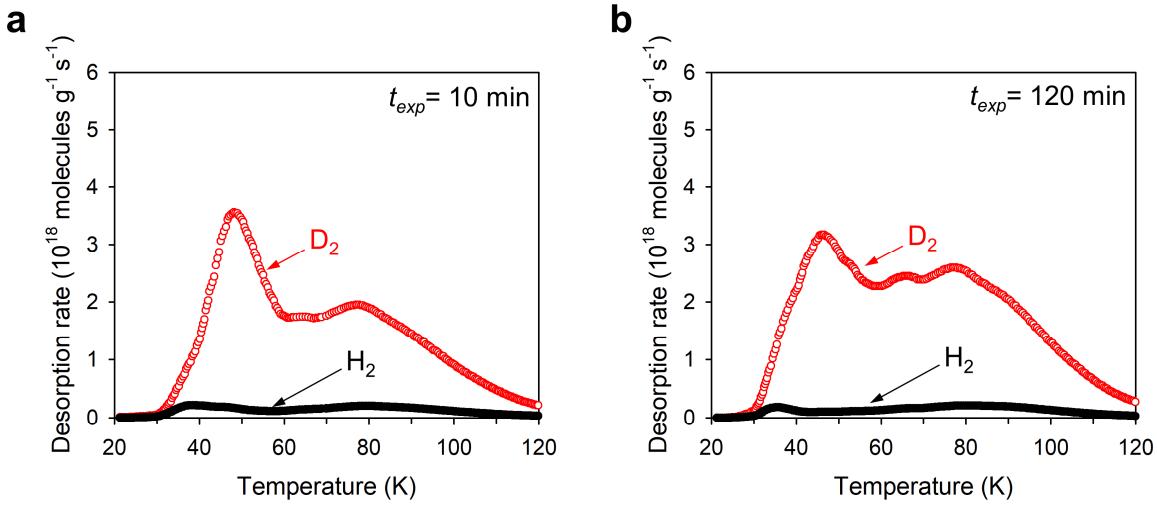

Figure 2.3.13 Thermal desorption spectra of mixture gas (1:1 H_2–D_2 mixture, 10 mbar) at 40 K as a function of exposure time (t_{exp}) (a) 10 min and (b) 120 min.

2.3.4 Conclusion

In conclusion, we experimentally investigated the dynamic breathing transition of the flexible MOF system, MIL-53(Al), for efficient hydrogen isotope separation. The direct D_2 over H_2 separation experiments using 1:1 D_2–H_2 mixture show that the selectivity is strongly correlated with the state of pore structure of MIL-53(Al). Due to the dynamic structural change from *np* to *lp* phase by breathing, MIL-53(Al) can continuously generate the effective pore aperture, maximizing the QS effect and resulting in a high selectivity ($S_{D2/H2}$ 10.5) with 2.3 mmol g^{-1} at 40 K. Further enhancement of separation performance was achieved by systematically tuning the breathing process by exposure pressure and time; highest selectivity, $S_{D2/H2}$ = 13.6, with high separation capacity of 2.9 mmol g^{-1}. We expect this study can provide an idea of developing an efficient system, exhibiting both, high selectivity and separation capacity, for separating gas mixtures of atoms/molecules with similar size and shape.

2.3.5 References

1. Schneemann, A.; Bon, V.; Schwedler, I.; Senkovska, I; Kaskel, S.; Fischer, R. A. *Chem. Soc. Rev.* **2014**, *43*, 6062.
2. Horike, S.; Shmomura, S.; Kitagawa, S. *Nat. Chem.* **2009**, *23*, 695.
3. Férey, G. *Chem. Soc. Rev.* **2008**, *37*, 191.
4. Coudert, F.-X. *Chem. Mater.* **2015**, *27*, 1905.
5. Liu, Y.; Her, J.-H.; Dailly, A.; Ramirez-Cuesta, A. J.; Neumann, D. A.; Brown, C. M. *J. Am. Chem. Soc.* **2008**, *130*, 11813.
6. Hyun, S.-m.; Lee, J. H.; Jung, G. Y.; Kim, Y. K.; Kim, T. K.; Jeoung, S.; Kwak, S. K.; Moon, D.; Moon, H. R. *Inorg. Chem.* **2016**, *55*, 1920.
7. Chang, Z.; Yang, D.-H.; Xu, J.; Hu, T.-L.; Bu, X.-H. *Adv. Mater.* **2015**, *27*, 5432.
8. Takashima, Y.; Martínez, V. M.; Furukawa, S.; Kondo, M.; Shimomura, S.; Uehara, H.; Nakahama, M.; Sugimoto, K.; Kitagawa, S. *Nat. Commun.* **2011**, *2*, 168.
9. Sato, H.; Kosaka, W.; Matsuda, R.; Hori. A.; Hijikata, Y.; Belosludov, R. V.; Sakaki, S.; Takata, M.; Kitagawa, S. *Science*, **2014**, *343*, 167.
10. Foo, M. L.; Matsuda, R.; Hijikata, Y.; Krishna, R.; Sato, H.; Horike, S.; Hori, A.; Duan, J.; Sato, Y.; Kubota, Y.; Takata, M.; Kitagawa, S. *J. Am. Chem. Soc.* **2016**, *138*, 3022.
11. Xiang, S.-C.; Zhang, Z.; Zhao, C.-G.; Hong, K.; Zhao, X.; Ding, D.-R.; Xie, M.-H.; Wu, C.-D.; Das, M. C.; Gill, R.; Thomas, K. M.; Chen, B. *Nat. Commun.* **2011**, *2*, 204.
12. Hamon, L.; Llewellyn, P. L.; Devic, T.; Ghoufi, A.; Clet, G.; Guillerm, V.; Pirngruber, G. D.; Maurin, G.; Serre, C.; Driver, G.; van Beek, W.; Jolimaître, E.; Vimont, A.; Daturi, M.; Férey, G. *J. Am. Chem. Soc.* **2009**, *131*, 17490.
13. Alaerts, L.; Maes, M.; Giebeler, L.; Jacobs, P. A.; Martens, J. A.; Denayer, J. F. M.; Kirschhock, C. E. A.; De Vos, D. E. *J. Am. Chem. Soc.* **2008**, *130*, 14170.
14. Heymans, N.; Vaesen, S.; De Weireld, G. *Microporous Mesoporous Mater.* **2012**, *154*, 93.
15. Kim, J.; Kim, W. Y.; Ahn, W.-S. *Fuel* **2012**, *102*, 574.
16. Springuel-Huet, M.-A.; Nossov, A.; Adem, Z.; Guenneau, F.; Volkringer, C.; Loiseau, T.; Férey, G.; Gédéon, A. *J. Am. Chem. Soc.* **2010**, *132*, 11599.

17. Walton, R. I.; Munn, A. S.; Guillou, N.; Millange, F.; *Chem.–Eur. J.* **2011**, *17*, 7069.

18. Boutin, A.; Bousquet, D.; Ortiz, A. U.; Coudert, F.-X.; Fuchs, A. H.; Ballandras, A.; Weber, G.; Bezverkhyy, I.; Bellat, J.-P.; Ortiz, G.; Chaplais, G.; Paillaud, J.-L.; Marichal, C.; Nouali, H.; Patarin, J. *J. Phys. Chem. C* **2013**, *117*, 8180.

19. Parent, L. R.; Pham, C. H.; Patterson, J. P.; Denny, Jr. M. S.; Cohen, S. M.; Gianneschi, N. C.; Paesani, F. *J. Am. Chem. Soc.* **2017**, *139*, 13973.

20. Seoane, B.; Sorribas, S.; Mayoral, Á.; Téllez, C.; Coronas, J. *Microporous Mesoporous Mater.* **2015**, *203*, 17.

21. Loiseau, T.; Serre, C.; Huguenard, C.; Fink, G.; Taulelle, F.; Henry, M.; Bataille, T.; Férey, G. *Chem.–Eur. J.* **2004**, *10*, 1373.

22. Boutin, A.; Springuel-Huet, M.; Nossov, A.; Gédéon, A.; Loiseau, T.; Volkringer, C.; Férey, G.; Coudert, F.; Fuchs, A. H. *Angew. Chem. Int. Ed.* **2009**, *48*, 8314.

23. Triguero, C.; Coudert, F.-X.; Boutin, A.; Fuchs, A. H.; Neimark, A. V. *J. Phys. Chem. Lett.* **2011**, *2*, 2033.

24. Neimark, A. V.; Coudert, F.-X.; Boutin, A.; Fuchs, A. H. *J. Phys. Chem. Lett.* **2010**, *1*, 445.

25. Niimura, S.; Fujimori, T.; Minami, D.; Hattori, Y.; Abrams, L.; Corbin, C.; Hata, K.; Kaneko, K. *J. Am. Chem. Soc.* **2012**, *134*, 18483.

26. Teufel, J.; Oh, H.; Hirscher, M.; Wahiduzzaman, M.; Zhechkov, L.; Kuc, A.; Heine, T.; Denysenko, D.; Volkmer, D. *Adv. Mater.* **2013**, *25*, 635.

27. Oh, H.; Kalidindi, S. B.; Um, Y.; Bureekaew, S.; Schmid, R.; Fischer, R. A.; Hirscher, M. *Angew. Chem. Int. Ed.* **2013**, *52*, 13219.

28. Kim, J. Y.; Balderas-Xicohténcatl, R.; Zhang, L.; Kang, S. G.; Hirscher, M.; Oh, H.; Moon, H. R. *J. Am. Chem. Soc.*, **2017**, *139*, 15135.

29. Chen, B.; Zhao, X.; Putkham, A.; Hong, K.; Lobkovsky, E. B.; Hurtado, E. J.; Fletcher, A. J.; Thomas, K. M. *J. Am. Chem. Soc.* **2008**, *130*, 6411.

30. Oh, H.; Park, K. S.; Kalidindi, S. B.; Fischer, R. A.; Hirscher, M. *J. Mater. Chem. A* **2013**, *1*, 3244.

31. Trung, T. K.; Trens, P.; Tanchoux, N.; Bourrelly, S.; Llewellyn, P. L.; Loera-Serna, S.; Serre, C.; Loiseau, T.; Fajula, F.; Férey, G. *J. Am. Chem. Soc.* **2008**, *130*, 16926.

32. Oh, H.; Kalidindi, S. B.; Um, Y.; Bureekaew, S.; Schmid, R.; Fischer, R. A.; Hirscher, M. *Angew. Chem. Int. Ed.* **2013**, *52*, 13219.

33. Oh, H.; Savchenko, I.; Mavrandonakis; A., Heine, T.; Hirscher, M. *ACS Nano* **2014**, *8*, 761.

34. Mounfield, W. P.; Walton, K. S. *J. Colloid Interface Sci.* **2015**, *447*, 33.

35. Pollock, R. A.; Her, J.-H.; Brown, C. M.; Liu, Y.; Dailly, A. *J. Phys. Chem. C* **2014**, *118*, 18197.

36. von Zeppelin, F.; Haluška, M.; Hirscher, M. *Thermochim. Acta* **2003**, *404*, 251.

37. Oh, H.; Savohenko, I.; Mavrandonakis, A.; Heine, T.; Hirscher, M. *ACS Nano* **2014**, *8*, 761.

2.4 Exploiting Diffusion Barrier and Chemical Affinity of Metal-Organic Frameworks for Efficient Hydrogen Isotope Separation

2.4.1 Introduction

Highly pure deuterium (D) is an irreplaceable raw material in industrial and scientific research, used for isotope tracing[1-3], neutron scattering[4-6], and fuel in future nuclear fusion reactors[7]. Thus to ensure a ready supply of this key material, a cost-effective and large-scale separation technique is required. However, the nearly identical physicochemical properties of deuterium and hydrogen make it difficult to extract deuterium from isotopic mixtures using conventional molecular sieving methods. The current separation technologies for purifying heavy hydrogen isotopes, such as liquid hydrogen distillation and the Girdler sulfide process, are extremely energy intensive, and, furthermore, possess low separation efficiencies (i.e. cryogenic distillation, with a selectivity of 1.5 at 24 K)[8] Recently, Geim *et al.* reported that the two-dimensional membranes of graphene or boron nitride could efficiently separate hydrogen ion isotopes[9]. In this work, hydrogen ions (H^+) diffuse 10 times faster than deuterium ions (D^+) through the two-dimensional crystal membrane at room temperature yielding a purer hydrogen gas. However, from an industrial viewpoint a product predominantly containing the heavier isotope would be more favourable. Thus, although it is still challenging, developing a cost- and energy-efficient system for directly extracting high purity deuterium is very important to meet industrial and scientific demand.

As a promising system for D_2/H_2 separation, nanoporous materials have attracted significant research interest, as they can directly capture heavier isotope gas molecules *via* kinetic quantum sieving (KQS)[10-26] or chemical affinity quantum sieving (CAQS)[27-30]. Heavier isotopes, having a shorter de Broglie wavelength at cryogenic temperatures, experience a lower diffusion barrier and can diffuse faster than lighter isotopes in a confined space, resulting in enrichment of the product with heavier isotope materials using the KQS effect[10]. Hirscher *et al.* enforced KQS effects by decorating the internal surface of MOFs and covalent organic frameworks (COFs) with Cl^- and pyridyl groups, respectively, in order to optimize pore aperture, leading to significantly enhanced isotope selectivity ($S_{D2/H2}$) of 7.5 at 60 K and 9.7 at 22 K, respectively[11,12]. However, due to the weak binding energies of hydrogen isotopes on the internal surface of porous materials, this approach effectively operates at only very low cryogenic temperatures. In order to overcome this limitation, CAQS exploits the preferential adsorption of heavier isotopes using strongly interacting sites introduced into the nanoporous materials[27-30]. As proposed theoretically as well as experimentally, the generation of open metal sites (OMSs) is a top priority for generating strong substrate interactions with H_2 and D_2[31-33]. FitzGerald *et al.* first explored the CAQS effect of OMSs in D_2/H_2 separation showing a selectivity of 5 at 77 K, which demonstrated that efficient selectivity can be achieved even at high temperatures using strong binding sites[27]. Nonetheless, a D_2/H_2

separation system comprising only OMSs is still far from meeting global demand and thus there is a critical need for an effectively designed of D_2-selective system.

Based on previous findings, the ideal deuterium separation and storage system should have a high density of OMSs that can selectively adsorb deuterium even at high temperatures and a narrow pore size for further increasing the separation effect through the selective diffusion of D_2 into the pores *via* KQS. In this sense, to realize very effective isotope separation, intelligently designed high capacity porous materials possessing both KQS and CAQS effects are required. Herein, we report a highly effective isotope separation system based on MOFs having a high uptake (2.8 mmol g^{-1}) with a separation factor as high as ~26 at 77 K by maximizing the synergistic effects of CAQS and KQS. To the best of our knowledge, this is the first study to implement two quantum sieving effects, KQS and CAQS, in one system to separate isotopic mixtures (Figure 2.4.1). For this purpose, MOF-74-Ni was chosen as the host material, providing CAQS functionality due to its high hydrogen adsorption enthalpies (~13 kJ mol^{-1}) at OMSs as reported in the literature[27,34]. Simultaneously, imidazole molecules (IM) were introduced into the one-dimensional (1D) channel of MOF-74-Ni as a diffusion barrier, effectively reducing the aperture size and repeatedly blocking H_2 diffusion, resulting in the KQS effect. Above all, the system can be implemented using a simple post-modification strategy by introducing the imidazole molecules into the MOF-74-Ni channel without complex structural design or a new MOF synthesis.

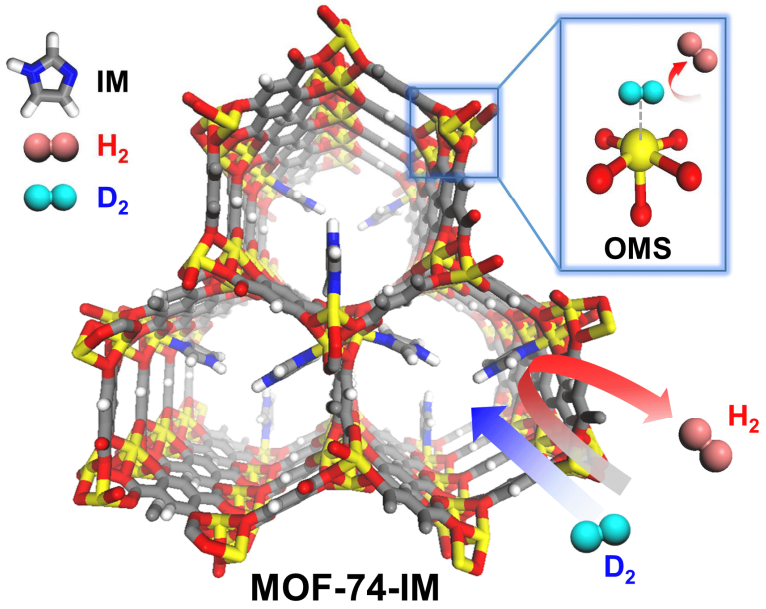

Figure 2.4.1 Schematic view of MOF-74-IM incorporating the OMS and imidazole. OMS and IM are employed for enhancing of the chemical affinity quantum sieving (CAQS) effect and the kinetic quantum sieving (KQS) effect, respectively.

2.4.2 Experimental Section

Methods

Materials and characterization. All chemicals and solvents were of reagent grade and were used as received without further purification. Fourier-transform (FT)-NMR spectra were recorded on a Varian 600 MHz spectrometer. Infrared (IR) spectra were recorded with a ThermoFisher Scientific Nicolet 6700 FT-IR spectrometer. Elemental analyses were performed at the UNIST Central Research Facilities Center (UCRF) in the Ulsan National Institute of Science and Technology (UNIST). UV-Vis-NIR spectra were recorded with a Cary 5000 UV/vis spectrophotometer. XRPD patterns were collected on a Bruker D8 advance diffractometer at 40 kV and 40 mA for Cu Kα (λ = 1.54050 Å), with a step size of 0.02° in 2θ. The nitrogen adsorption-desorption isotherms were obtained using a BELSORP-max at 77 K. Prior to the adsorption measurements, all samples (~100 mg) were evacuated ($p < 10^{-5}$ mbar) at 393 K for 5 h. The specific surface area was determined from the linear part of the Brunauer-Emmett-Teller (BET) equation, and the total pore volume was calculated from the amount adsorbed at a relative pressure of 0.99. The micropore volume was computed using the Horvath-Kawazoe (HK) method. The hydrogen and deuterium adsorption isotherms of all samples were measured at 20 K to 77 K using a fully automated Quantachrome Autosorb-iQ with a controlled cryo-cooler. All samples (~70 mg) were activated under ultra-high vacuum at 400 K for 5 h prior to each measurement.

Synthesis of 2,5-dioxido-1,4-benzenedicarboxylic acid (H_4dobdc). 2,5-Dioxido-1,4-benzenedicarboxylic acid (H_4dobdc) was prepared using a reported method[35] with minor modifications. K_2CO_3 (24.42 g, 177 mmol) was placed in a 250 mL 2-neck round bottom flask equipped with a condenser. Formic acid (8.7 ml, 230 mmol) was slowly added under stirring and the mixture was heated to 210 ^oC for 30 min under Ar flow. When the temperature reached to 210 ^oC, Ar flow changed to CO_2 flow and hydroquinone (5.56 g, 50.5 mmol) was quickly added. After stirred at 210 ^oC for 6 h, the boiling deionized water (H_2O, 75 mL) was added to the dark brown reaction mixture, cooled to room temperature, filtered, and washed briefly with H_2O. The resultant gray product was suspended in H_2O (50 mL) and acidified with HCl (10 mL, 37%). The suspension changed to yellow color and kept stirring for 1 h, filtered, and washed 3 times with H_2O. The resultant yellow product was dried at 80 ^oC overnight under vacuum. Yield: 4.2 g (42%), ^{1}H-NMR (DMSO-d_6): δ 7.28 (s, 2H), FT-IR (ATR): $\nu_{O-C=O}$ 1641(s) cm^{-1}.

Synthesis of MOF-74-ac. MOF-74-Ni was prepared using a reported method[35] with minor modifications. An aqueous suspension (15 mL) of H_4dobdc (0.404 g, 2.04 mmol) was refluxed with stirring, to which an aqueous solution (5 mL) of $Ni(CH_3COO)_2 \cdot 4H_2O$ (1.00 g, 4 mmol) was added. The solution was stirred for 1 h and cooled to room temperature. The yellow powder was collected by centrifugation at 7500 rpm and washed 3 times with hot H_2O and washed 3 times with methanol.

Heating at 250 °C under vacuum for 5 h yielded the fully activated adsorbent MOF-74-Ni (designated MOF-74-ac), the yellow powder was stored in an Ar-filled glove box. Yield: 0.495 g (79%). Anal. calcd. for MOF-74-ac, $[Ni_2(dobdc)(H_2O)_{1.1}]$ ($Ni_2C_8H_{4.2}O_{7.1}$): C, 29.00; H, 1.28%; Found: C, 29.60; H, 1.34%. FT-IR (ATR, cm^{-1}): $\nu_{O-C=O(carboxylate,\ asym)}$ = 1555(s), $\nu_{O-C=O(carboxylate,\ sym)}$ = 1414(s), ν_{C-O} = 1239(s). The elemental analysis was conducted in air so that H_2O could be adsorbed from air.

Preparation of MOF-74-IM. As-synthesized MOF-74-Ni was activated by heating at 250 °C in vacuum for 5 h, and is hereafter referred to as MOF-74-ac. In an Ar-filled glove box, the yellow powder of MOF-74-ac (0.100 g, 0.640 mmol based on Ni^{2+}) was suspended in anhydrous DCM (8.00 mL) under vigorous stirring. To this solution 2.00 mL of imidazole solution in DCM was added, which corresponds to a concentration of 3.20 x 10^{-2}, 1.28 x 10^{-1}, and 2.24 x 10^{-1} M for MOF-74-IM-10, MOF-74-IM-38, and MOF-74-IM-70, respectively. After stirring for 15 h at room temperature, the greenish resultant solid was isolated by centrifugation and dried in an Ar-filled glove box. For further measurements and experiments, the product was completely dried at 120 °C under vacuum for 5 h. Anal. calcd. for MOF-74-IM-10, $[Ni_2(dobdc)(IM)_{0.2}(H_2O)_{1.3}]$ ($Ni_2C_{8.6}H_{5.4}N_{0.4}O_{7.3}$): C, 29.60; H, 1.56; N, 1.61%; Found: C, 30.00; H, 1.52; N, 1.59%. FT-IR (ATR, cm^{-1}): $\nu_{N-H(imidazole)}$ = 3434, $\nu_{C-H(imidazole)}$ = 3150, $\nu_{O-C=O(carboxylate,\ asym)}$ = 1552(s), $\nu_{O-C=O(carboxylate,\ sym)}$ = 1415(s), ν_{C-O} = 1235(s), $\delta_{C-H(imidazole)}$ = 1058, $\delta_{C-H(imidazole)}$ = 729. Anal. calcd. for MOF-74-IM-38, $[Ni_2(dobdc)(IM)_{0.76}(H_2O)_{0.60}]$ ($Ni_2C_{10.28}H_{6.24}N_{1.52}O_{6.6}$): C, 33.01; H, 1.68; N, 5.69%; Found: C, 33.52; H, 1.73; N, 5.65%. FT-IR (ATR, cm^{-1}): $\nu_{N-H(imidazole)}$ = 3430, $\nu_{C-H(imidazole)}$ = 3146, $\nu_{O-C=O(carboxylate,\ asym)}$ = 1552(s), $\nu_{O-C=O(carboxylate,\ sym)}$ = 1411(s), ν_{C-O} = 1239(s), $\delta_{C-H(imidazole)}$ = 1058, $\delta_{C-H(imidazole)}$ = 741. Anal. calcd. for MOF-74-IM-70, $[Ni_2(dobdc)(IM)_{1.4}(H_2O)_{0.5}]$ ($Ni_2C_{12.2}H_{8.6}N_{2.8}O_{6.5}$): C, 35.24; H, 2.08; N, 9.43%; Found: C, 35.00; H, 2.17; N, 9.42%. FT-IR (ATR, cm^{-1}): $\nu_{N-H(imidazole)}$ = 3426, $\nu_{C-H(imidazole)}$ = 3140, $\nu_{O-C=O(carboxylate,\ asym)}$ = 1556(s), $\nu_{O-C=O(carboxylate,\ sym)}$ = 1411(s), ν_{C-O} = 1238(s), $\delta_{C-H(imidazole)}$ = 1061, $\delta_{C-H(imidazole)}$ = 739. Since the sample preparation of elemental analyses was conducted in air, adsorbed water molecules were detected despite careful handling.

N_2 BET measurement. Specific surface area measurements at 77 K were carried out using Belsorb instrument with N_2 gas using optimized protocols, and all samples (~100 mg) were priory degassed at 393 K for 5 h. The specific surface area was obtained by the Brunauer-Emmett-Teller (BET) method. The micropores volume were computed from the Horvath-Kawazoe (HK) method.

Low-pressure, high-resolution hydrogen/deuterium adsorption isotherm measurement. The hydrogen and deuterium adsorption isotherms of all samples were measured at 20 K to 77 K by full automated Quantachrome Autosorb-iQ with controlled cryocooler. Around 70 mg of all samples were activated under ultra-high vacuum at 400 K for 5 h prior to each measurement.

Low temperature thermal desorption spectroscopy (TDS). A laboratory-designed experimental set-up is previously described in details[2] with ca. 3~4 mg of samples. The HV chamber contains the sample

holder that is screwed tightly to a Cu block, which is surrounded by a resistive heater. This Cu block is connected to a cold finger of a flowing helium cryostat, which allows cooling below 20 K. All samples were activated at 400 K, 5 h. For the pure gas thermal desorption experiment, the sample is exposed to pure D_2 or H_2 atmosphere (10 mbar) at RT. Afterwards, the sample is rapidly cooled to the boiling temperature of the adsorbed gas, and the gas molecules that had not been adsorbed were pumped out. Finally, a linear heating ramp (0.1 K s^{-1}) is applied. In case of the D_2/H_2 mixture thermal desorption experiments, the sample was exposed to a 10 mbar 1:1 D_2/H_2 mixture at the given exposure temperatures between 20 K to 77 K for 10 min. After 10 min, the gas molecules that had not been adsorbed were mildly pumped off until HV is reached again. Afterwards, the sample chamber was cooled quickly down to below 20 K. For desorption, the sample was heated with a rate of 0.1 K s^{-1} from 20 K to 150 K and the desorbing gas was continuously detected by a quadrupole mass spectrometer. In order to quantify the mass spectrometer signal, the TDS device had been calibrated by a hydrogen/deuterium loaded $Pd_{95}Ce_5$ alloy.

Theoretical calculation. Plane wave DFT calculations were carried out using the Vienna ab initio Simulation Package (VASP)[36,37]. We used the Perdew-Burke-Ernzerhof (PBE) generalized gradient approximation (GGA) functional[38]. The Grimme D3 (DFT-D3) correction was included in our calculations for dispersion correction[39]. An energy cutoff and the convergence criterion of the energy were set to 600 eV and 2×10^{-4} eV, respectively. Each atom was fully relaxed until the forces were below 0.03 eV $Å^{-1}$. The spin polarization was included in our calculations. A 1×1×4 Monkhorst-Pack k-point grid was chosen[40]. The Hubbard U correction with U_{eff} = 6.4 eV for Ni was applied using DFT+U method by Dudarev[41,42]. For the calculation of classical migration energy of deuterium and hydrogen molecules, the climbing image nudged elastic band (CI-NEB) method was employed[43]. Zero point energy (ZPE) corrections to the classical migration energy of H_2 and D_2 was applied in our calculations.

Table 2.4.1. Summary of experiment conditions with different molar ratio of imidazole to Ni^{2+} and elemental compositions of the resultant materials.

Sample[a]	Amounts used in experiments		Molar ratio	Elemental analysis, wt% (Anal. Calcd.)			
	MOF-74	Imidazole	Imidazole/Ni^{2+}	C	H	N	Formula
MOF-74-IM-10	0.10 g (0.64 mmol of Ni^{2+})	0.064 mmol	0.1	30.00 (29.60)	1.52 (1.56)	1.59 (1.61)	$[Ni_2(C_8O_6H_2)\cdot(C_3N_2H_4)_{0.20}\cdot(H_2O)_{1.30}]$
MOF-74-IM-38		0.256 mmol	0.4	33.52 (33.01)	1.73 (1.68)	5.65 (5.69)	$[Ni_2(C_8O_6H_2)\cdot(C_3N_2H_4)_{0.76}\cdot(H_2O)_{0.60}]$
MOF-74-IM-70		0.448 mmol	0.7	35.00 (35.24)	2.17 (2.08)	9.42 (9.43)	$[Ni_2(C_8O_6H_2)\cdot(C_3N_2H_4)_{1.40}\cdot(H_2O)_{0.50}]$

[a] The name of post synthetically modified MOF samples are designated based on the EA results, as given in Table 2..4.1.

2.4.3 Results and Discussion

Synthesis and Characterization. In order to develop a system containing OMSs as well as diffusion barriers, first, as-prepared MOF-74-Ni was completely activated at 250 °C in vacuum for 5 h (designated as MOF-74-ac). MOF-74-ac which has fully exposed OMSs was soaked in the solutions of imidazole in dichloromethane (DCM) with three different concentrations in order to prepare different amounts of imidazole containing MOF-74-Ni. As calculated based on the elemental analyses results, the resultant MOF samples contained 10, 38, and 70% of all Ni^{2+} OMSs in MOF-74-Ni occupied by imidazole molecules, respectively, denoted MOF-74-IM-10, MOF-74-IM-38, and MOF-74-IM-70 (Table 2.4.1). The X-ray powder diffraction (XRPD) patterns of MOF-74-ac, MOF-74-IM-10, MOF-74-IM-38, and MOF-74-IM-70 indicate that the framework structures of samples were maintained after post-synthetic treatments (Figure 2.4.2). In order to examine the incorporation of imidazole molecules in MOF-74-Ni, Fourier transform-infrared (FT-IR) spectra were obtained. As shown in Figure 2.4.3, compare with MOF-74-ac, MOF-74-IM-10 shows weak additional peaks at 3434, 3150, 1058, and 729 cm^{-1}, which correspond to ν(N-H), ν(C-H), δ(C-H), and δ(C-H) of the imidazole molecule, respectively[44.45]. The same peaks were observed in MOF-74-IM-38 and MOF-74-IM-70 with higher intensities due to the increase in the amount of imidazole. The appearance of the N-H stretching vibration around 3430 cm^{-1} indicates that the incorporated imidazole molecules are neutral and not in the deprotonated form as imidazolate. The coordination of incorporated imidazole molecules to the Ni^{2+}

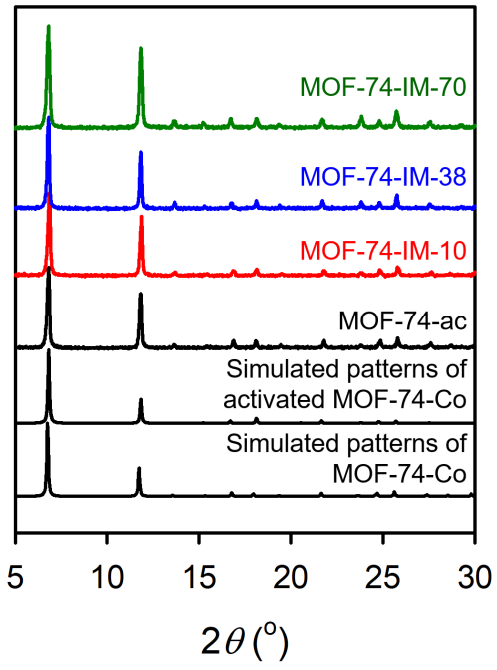

Figure 2.4.2 XRPD patterns of MOF-74-ac (black), MOF-74-IM-10 (red), MOF-74-IM-38 (blue), and MOF-74-IM-70 (green) with the simulated XRPD patterns of MOF-74-Co.

OMSs was verified by ultraviolet visible near-infra red (UV-Vis-NIR) spectroscopy *via* diffuse reflectance spectroscopic measurements conducted with solid powders (Figure 2.4.4). In MOF-74-ac, five-coordinated Ni^{2+}−OMSs species in a square-pyramidal geometry show absorption bands at 14144, 10040 and 5555 cm^{-1}, which correspond to the electronic transitions, $^3B_1(^3F) \rightarrow {}^3A_2(^3F)$, $^3B_1(^3F) \rightarrow {}^3B_2(^3F)$, and $^3B_1(^3F) \rightarrow {}^3A_2(^3P)$, respectively[46]. Upon inclusion of imidazole molecules into MOF-74-ac, new absorption peaks appear at 13141 and 9930 cm^{-1}, which clearly show the *d-d* transitions of an octahedral six-coordinated Ni^{2+} species, $^3A_{2g}(^3F) \rightarrow {}^3T_{1g}(^3F)$ and $^3A_{2g}(^3F) \rightarrow {}^3T_{2g}(^3F)$, respectively[37]. As the amount of coordinating imidazole molecules increases, absorption bands related to five-coordinate Ni^{2+} decrease, while bands corresponding to six-coordinate Ni^{2+} species increase. In order to exclude the possibility of H_2O molecules coordination instead of imidazole molecules in an ambient atmosphere, the UV-Vis-NIR spectra for intentionally air-exposed samples were examined. For MOF-74-IM series as well as MOF-74-ac, a new peak at 5556 cm^{-1} was clearly shown, which is a characteristic H_2O overtone peak originating from the coordination of H_2O molecules upon exposure to air[47] (Figure 2.4.5). The decreasing intensity of the H_2O overtone peak with increasing amount of imidazole molecules in MOF-74-Ni indicates that the imidazole molecules occupy Ni^{2+}-OMSs. Overall, *via* simple post-synthetic modification we successfully prepared a series of MOF-74-IM materials possessing 1D channels decorated with different amounts of imidazole molecules as well as OMSs.

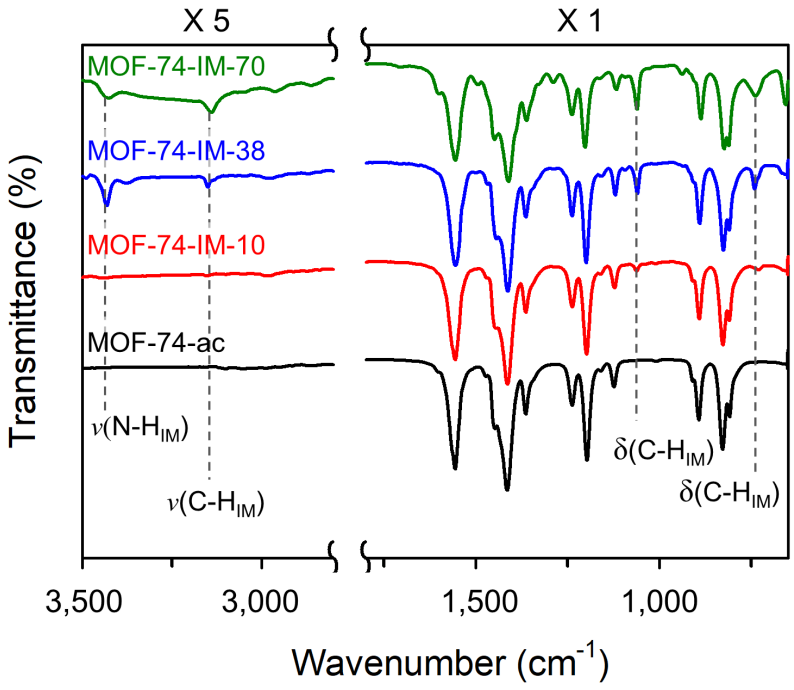

Figure 2.4.3 FT-IR spectra of MOF-74-ac (black), MOF-74-IM-10 (red), MOF-74-IM-38 (blue), and MOF-74-IM-70 (green).

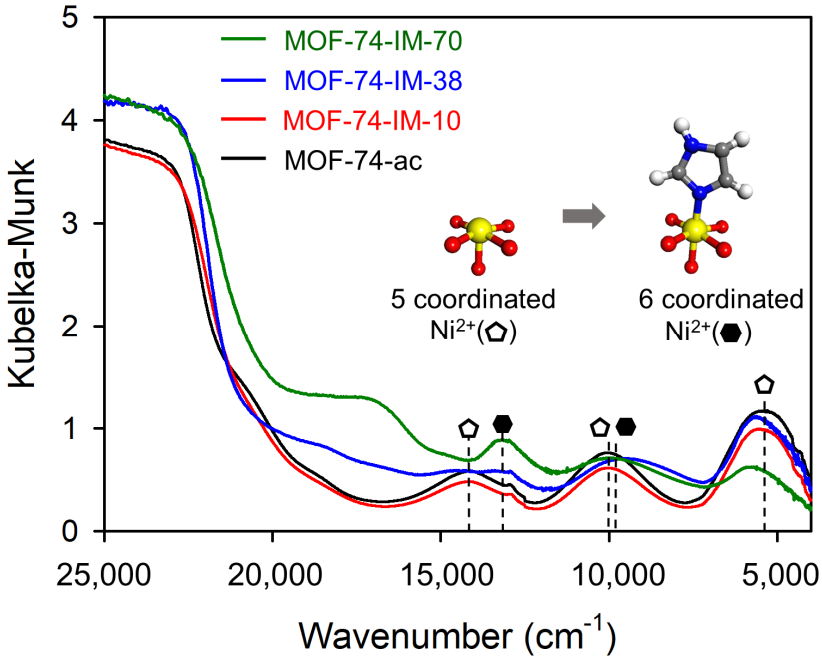

Figure 2.4.4 Diffuse reflectance UV-Vis-NIR spectra of MOF-74-ac (black), MOF-74-IM-10 (red), MOF-74-IM-38 (blue), and MOF-74-IM-70 (green).

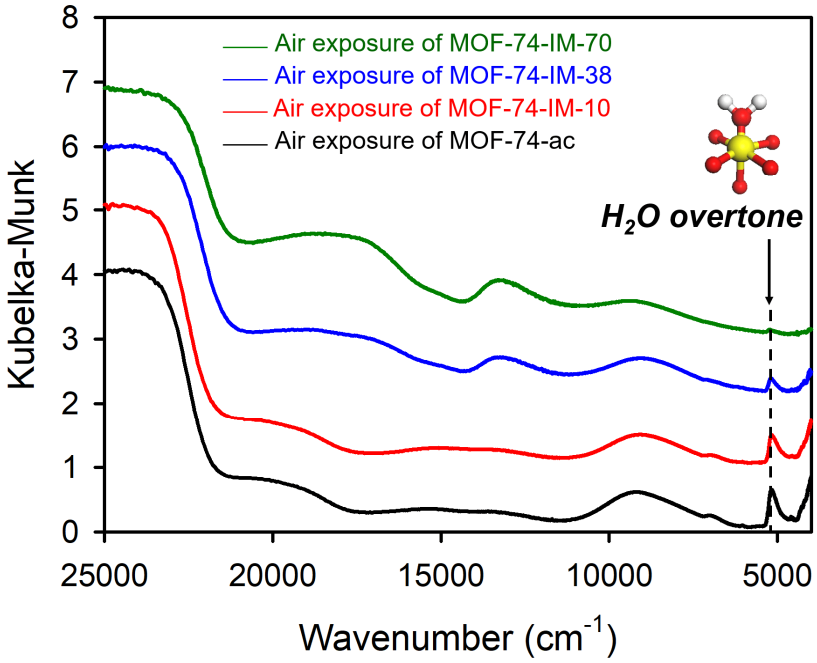

Figure 2.4.5 Diffuse reflectance UV-Vis-NIR spectra of MOF-74-ac (black), MOF-74-IM-10 (red), MOF-74-IM-38 (blue), and MOF-74-IM-70 (green) after air exposure for 15 min. The peak intensity at ca. 5556 cm^{-1} of H_2O overtone decreases as increasing the amount of coordinated IM. For clarity, DR-UV-Vis-NIR spectra were shifted upward by 1.

Examination of Aperture Modification. In order to understand the effect of imidazole addition on the pore structure of MOF-74-Ni, we conducted N_2 adsorption/desorption experiments at 77 K for MOF-74-ac and imidazole coordinated samples. Brunauer-Emmett-Teller (BET) surface area is increasingly reduced from 1406 $m^2 g^{-1}$ for MOF-74-ac to 1094 and 425 $m^2 g^{-1}$ for MOF-74-IM-10 and MOF-74-IM-38, respectively, as the number of coordinated imidazole molecules increased. Despite this, these samples were still microporous (Figure 2.4.6a and Table 2.4.2). After loading 70% of Ni^{2+} OMSs with imidazole molecules, the surface area decreased to 51 $m^2 g^{-1}$ showing a nonporous nature, which indicated that the pores of MOF-74-IM-70 were mostly blocked by imidazole molecules and were thus inaccessible to N_2 molecules. H_2 sorption experiments at 77 K with N_2 sorption studies imply that our synthetic strategy can be potentially exploited as a D_2/H_2 separation system. For N_2 and H_2 gases, MOF-74-ac does not limit the diffusion due to its large channel diameter (~1.1 nm) and thus exhibits fully reversible isotherms. On the other hand, MOF-74-IM-10 and MOF-74-IM-38 show large hysteresis loops due to the increasing amount of coordinated imidazole, implying slow diffusion kinetics (Figure 2.4.6). Moreover, despite a 30% difference in the N_2 BET surface area between MOF-74-ac and MOF-74-IM-10, their similar H_2 uptake indicates that aperture modification by imidazole molecule coordination generates selective accessibility for H_2 over N_2 due to the existence of numerous apertures smaller than the N_2 probe. For H_2 and D_2 gas sorption isotherms obtained at various exposure temperatures (25, 40, 60, and 77 K) (Figures 2.4.7-10), MOF-74-IM-10 and MOF-74-IM-38 show hysteresis loops (Figures 2.4.8 and 2.4.9), revealing the existence of a diffusion barrier indicating that the KQS effect exists over the entire measured temperature range. Due to the nonporous nature of MOF-74-IM-70 (Figure 2.4.10), it was excluded for further measurements. Smaller hysteresis with higher uptake of D_2 over H_2 may be ascribed to its favourable diffusion in this pore system, which possesses a smaller de Broglie wavelength and lower zero point energy in confinement. Therefore, the present aperture modification strategy may effectively form a kinetic diffusion barrier in MOF-74, indicating that the MOF-74-IM system may be a potential advanced material for applications in D_2/H_2 separation.

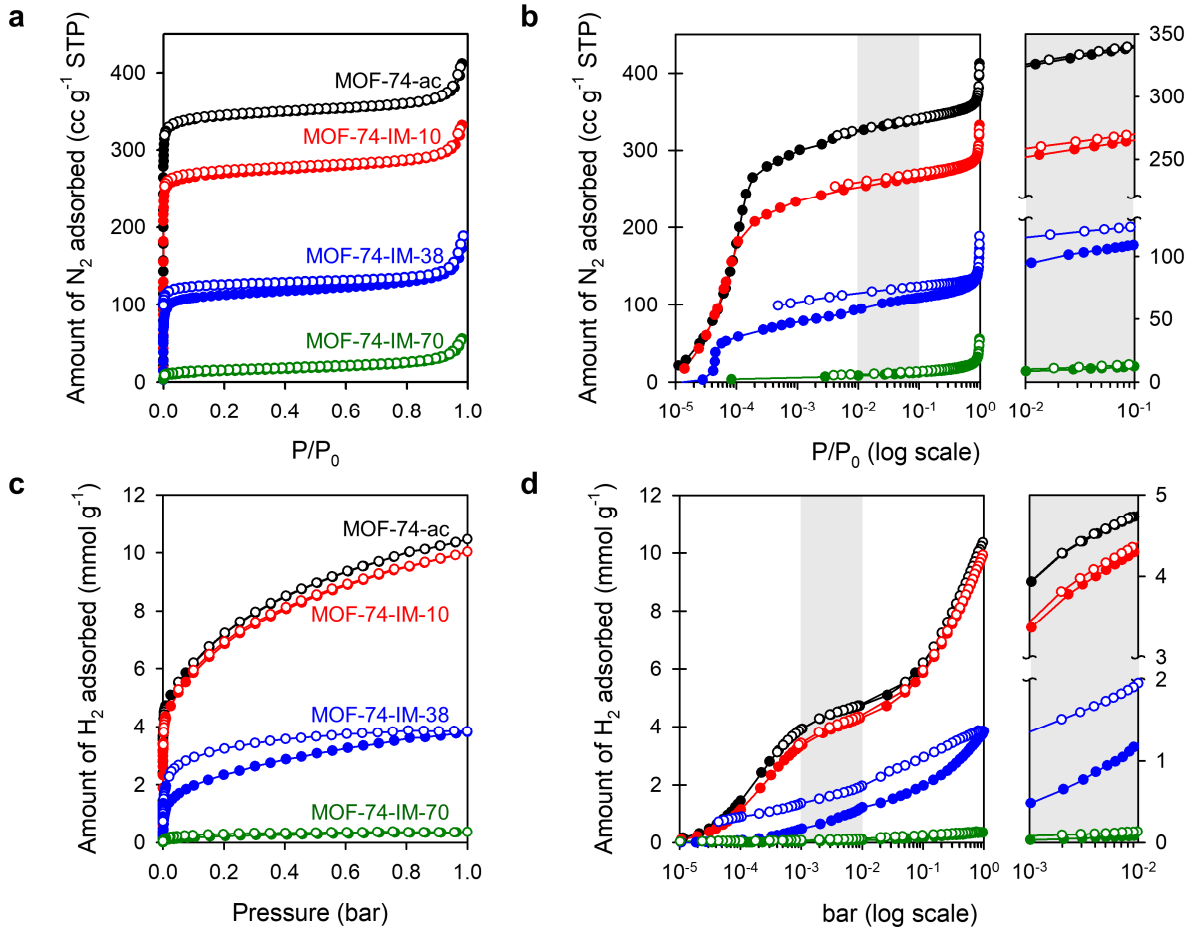

Figure 2.4.6 Gas sorption isotherms on the MOF-74-ac and MOF-74-IMs. (**a**) N_2 sorption, and (**b**) H_2 sorption isotherms represented in linear and log scale at 77 K of MOF-74-ac (black), MOF-74-IM-10 (red), MOF-74-IM-38 (blue), and MOF-74-IM-70 (green). Filled and open symbols correspond to adsorption and desorption, respectively. The grey coloured graphs to the right are the enlargement of the low-pressure region in the sorption isotherms in log scale.

Table 2.4.2 Summary of N_2 sorption of MOF-74-ac, MOF-74-IM-10, MOF-74-IM-38, and MOF-74-IM-70.

Sample name	S_{BET}[a] (m^2/g)	V_t[b] (cm^3/g)	D_{HK}[c] (nm)
MOF-74-ac	1406	0.64	0.74
MOF-74-IM-10	1094	0.51	0.71
MOF-74-IM-38	436	0.29	0.69
MOF-74-IM-70	51	0.086	-

[a] The specific surface area (S_{BET}) was calculated by nitrogen isotherm using Brunauer-Emmet-Teller (BET) method. [b] V_t represented the total pore volume at $P/P_0 = 0.99$. [c] D_{HK} represents the micropore size by the Horvath-Kawazoe (HK) method.

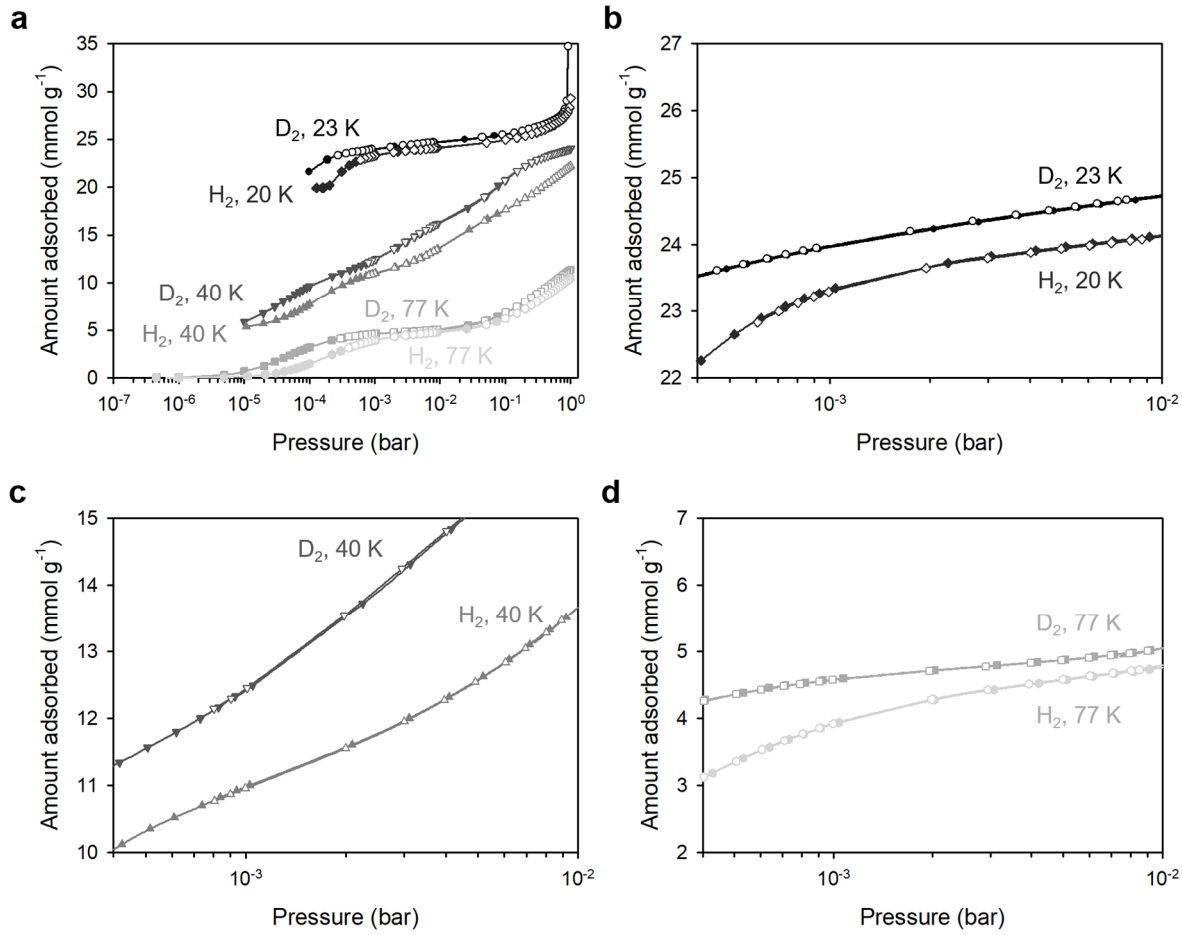

Figure 2.4.7 H_2 and D_2 sorption isotherms for (a) MOF-74-ac, and enlargement at (b) 20-23 K, (c) 40 K, and (d) 77 K. Filled and open symbols correspond to adsorption and desorption, respectively. The desorption isotherms for MOF-74-ac show the fully reversible desorption isotherm.

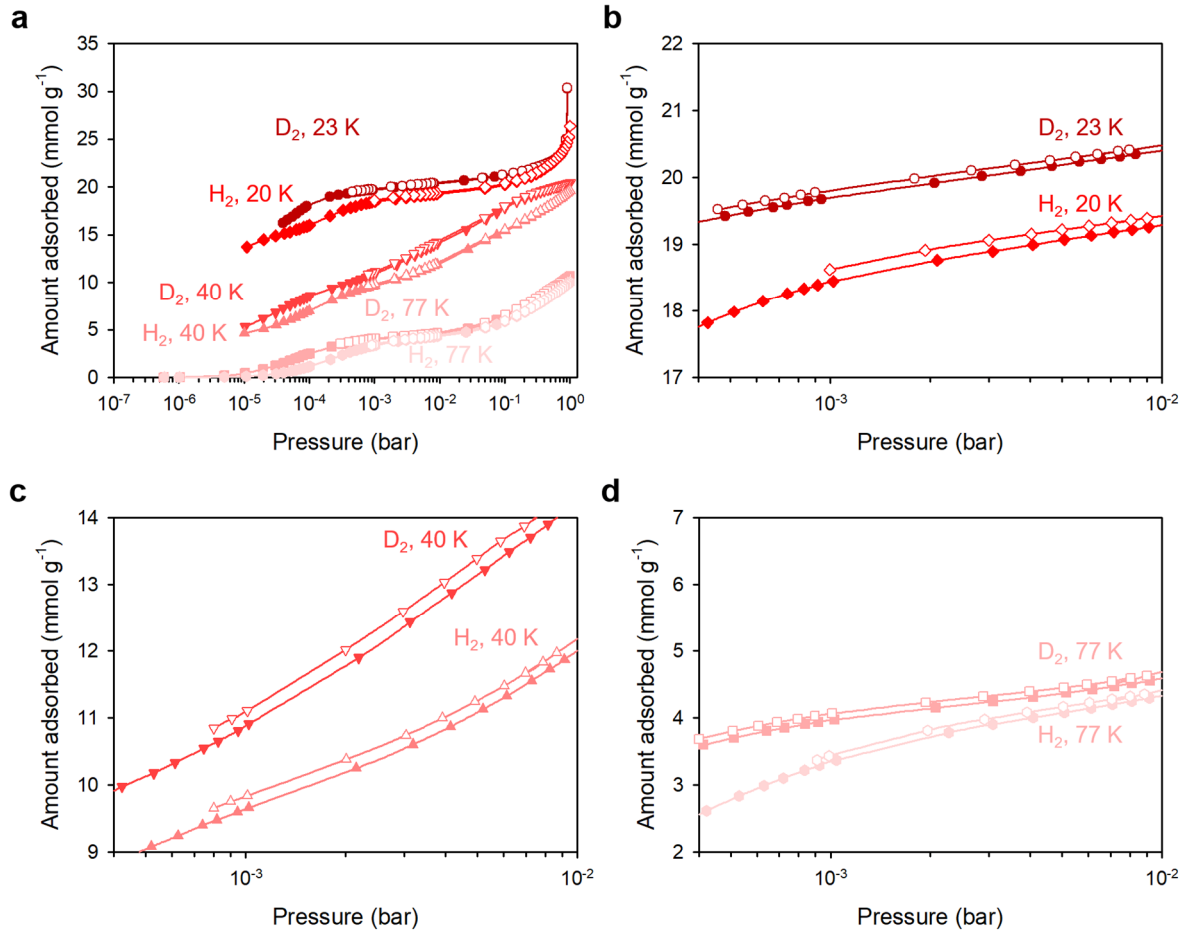

Figure 2.4.8 H_2 and D_2 sorption isotherms for (a) MOF-74-IM-10, and enlargement at (b) 20-23 K, (c) 40 K, and (d) 77 K. Filled and open symbols correspond to adsorption and desorption, respectively. The desorption isotherms for MOF-74-IM-10 show the large hysteresis.

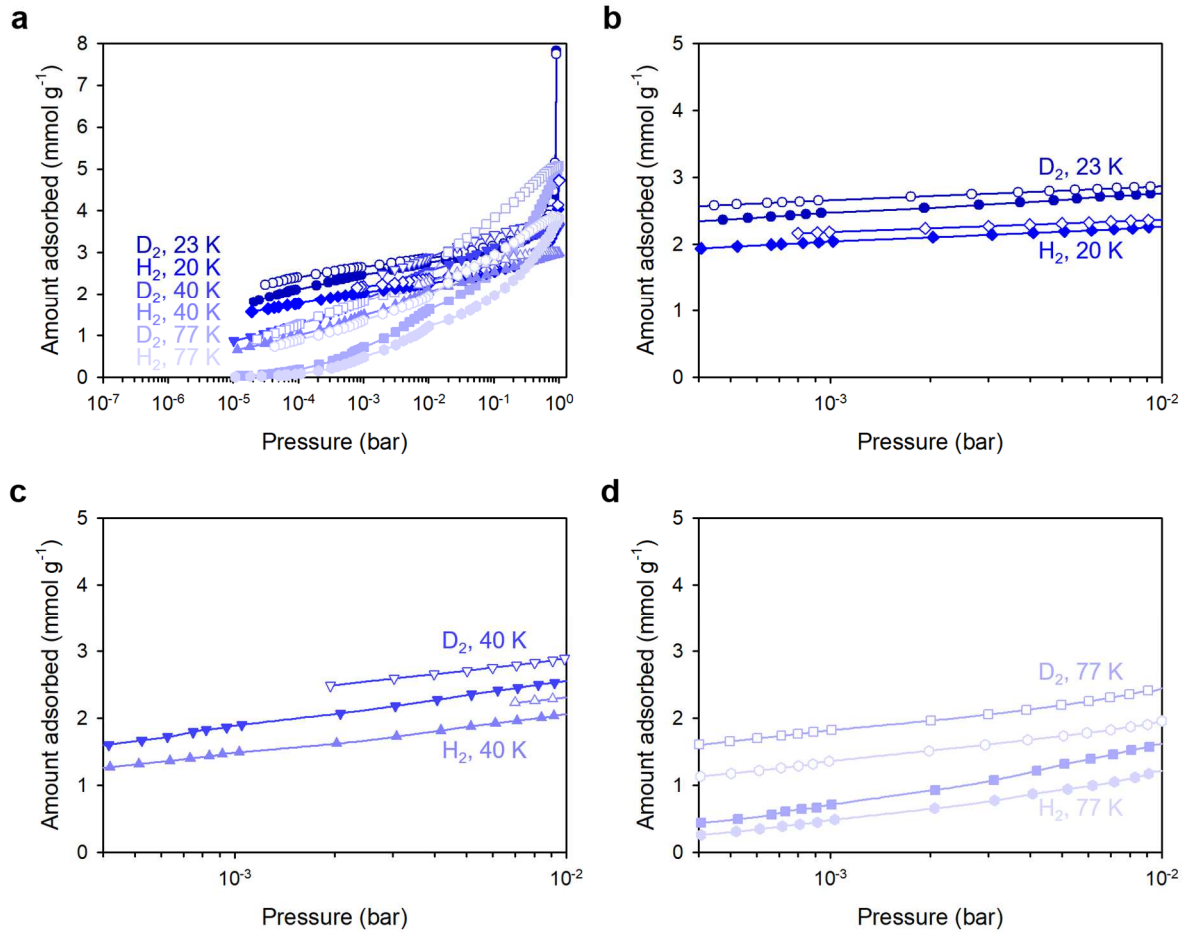

Figure 2.4.9 H_2 and D_2 sorption isotherms for (a) MOF-74-IM-38, and enlargement at (b) 20-23 K, (c) 40 K, and (d) 77 K. Filled and open symbols correspond to adsorption and desorption, respectively. The desorption isotherms for MOF-74-IM-38 show the large hysteresis.

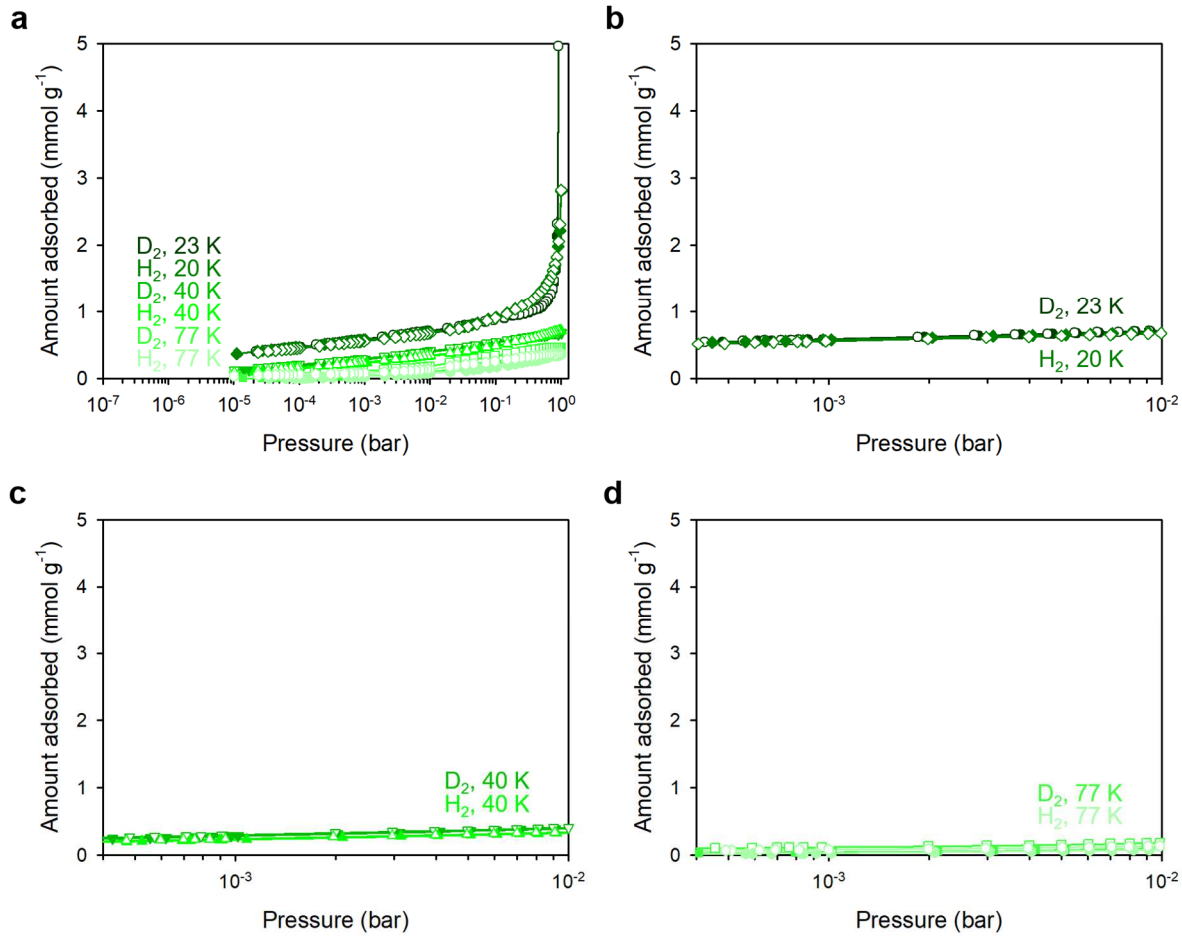

Figure 2.4.10 H_2 and D_2 sorption isotherms for (a) MOF-74-IM-70, and enlargement at (b) 20-23 K, (c) 40 K, and (d) 77 K. Filled and open symbols correspond to adsorption and desorption, respectively. The sorption isotherms for MOF-74-IM-70 show the nonporous nature.

TDS studies of adsorption sites and preferential isotope binding on the sites. In order to verify the adsorption sites on the MOF-74-Ni based-samples and their adsorption affinity to H_2 and D_2, cryogenic thermal desorption spectroscopy (TDS)[11,28] measurements were performed for pure H_2 and D_2 gas. MOF-74-IM-10 was exposed to a pure D_2 or H_2 atmosphere (10 mbar) at room temperature. Afterwards, the sample was rapidly cooled to the target exposure temperature, T_{exp}, of 25 K. After 3 min exposure, the sample chamber was evacuated, and cooled quickly down to below 20 K. A heating ramp of 0.1 K s^{-1} was applied and the TDS spectrum was obtained between 20 - 120 K. As shown in Figure 2.4.11a, the spectra for both H_2 and D_2 show three desorption peak maxima. This phenomenon has been similarly observed in previous studies using MOF-74-Co[28]. Along with well-known neutron powder diffraction results[48], those three peaks were assigned as three energetically different adsorption sites, namely, adsorption at a benzene ring (site I), at a triangle of oxygen atoms (site II), and at an OMS (site III). For both H_2 and D_2, the three desorption peak maxima appeared at different temperature shifts. The peak corresponding to desorption from site I (benzene ring) appeared at 32 K for H_2 and 34 K for D_2 while desorption from site II (triangle of oxygen atoms) occurred at 41 K and 45 K for H_2 and D_2, respectively. Significantly, the desorption maximum of D_2 from site III (OMS) occurred at 85 K, which is much higher than that of hydrogen by ~7 K, indicating a huge difference between H_2 and D_2 adsorption enthalpy at OMSs. We attribute this to the presence of a strong CAQS effect. Considering the desorption temperature maxima, we classify sites I and II as weak binding site (WBS) and site III as a strong binding site (SBS).

The preference of SBSs for D_2 over H_2 is clearly visible in the TDS spectra obtained for the isotopic mixture of H_2 and D_2. As shown in Figure 2.4.11b, the SBSs dominantly adsorb D_2 over H_2 at T_{exp} = 25 K. Despite increasing T_{exp} from 25 to 77 K (Figure 2.4.13), D_2 adsorption still dominantly occurs at SBSs, leading to potentially efficient isotope separation even at high temperatures. Further examination of the performance of MOF-74-ac and MOF-74-IM-38 using a 1:1 isotope mixture also clearly demonstrates the existence of SBSs and the preferential adsorption of D_2 over H_2 on these sites (Figures 2.4.12 and 2.4.14), indicating a strong CAQS effect. However, the number of SBSs is dramatically reduced with increasing imidazole content, which in turn reduces the CAQS effect. Thus, optimization of the amount of imidazole in the system is crucial to effectively merge both the KQS and CAQS effects.

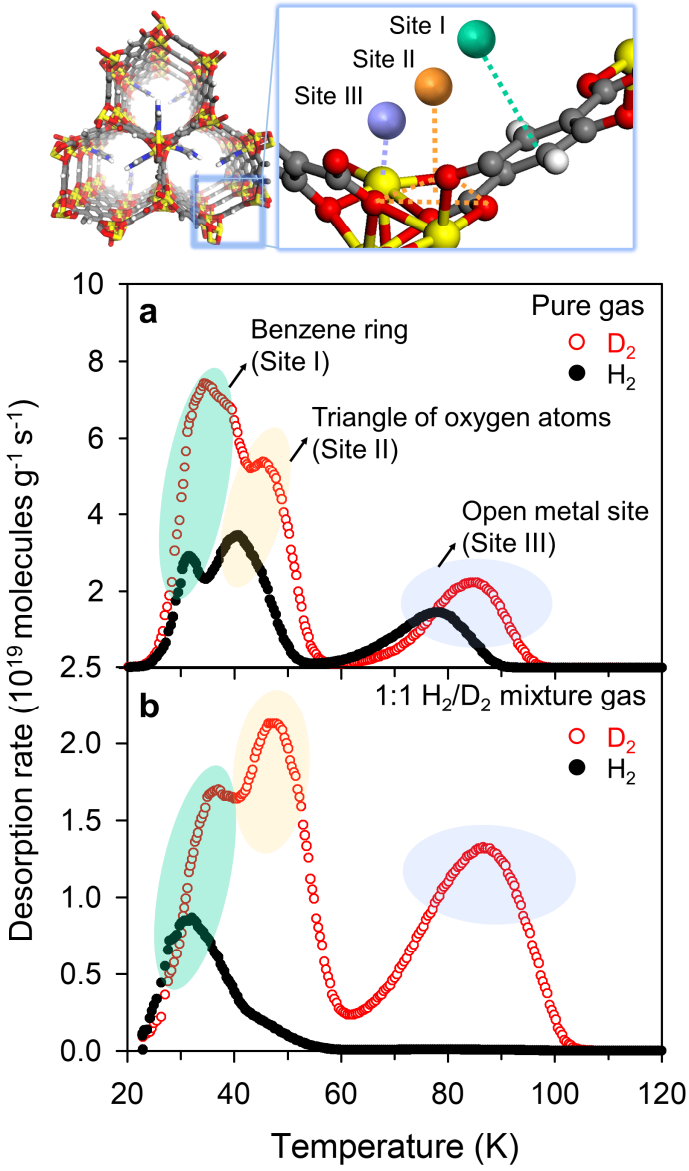

Figure 2.4.11 Thermal desorption spectra of MOF-74-IM-10. (**a**) pure gas H_2 (black, filled circle) and D_2 (red, open circle) and (**b**) 1:1 D_2/H_2 mixture gas loading on MOF-74-IM-10 at an exposure temperature, T_{exp}, of 25 K. The site III clearly shows preferential adsorption of D_2 over H_2 from the isotope mixture.

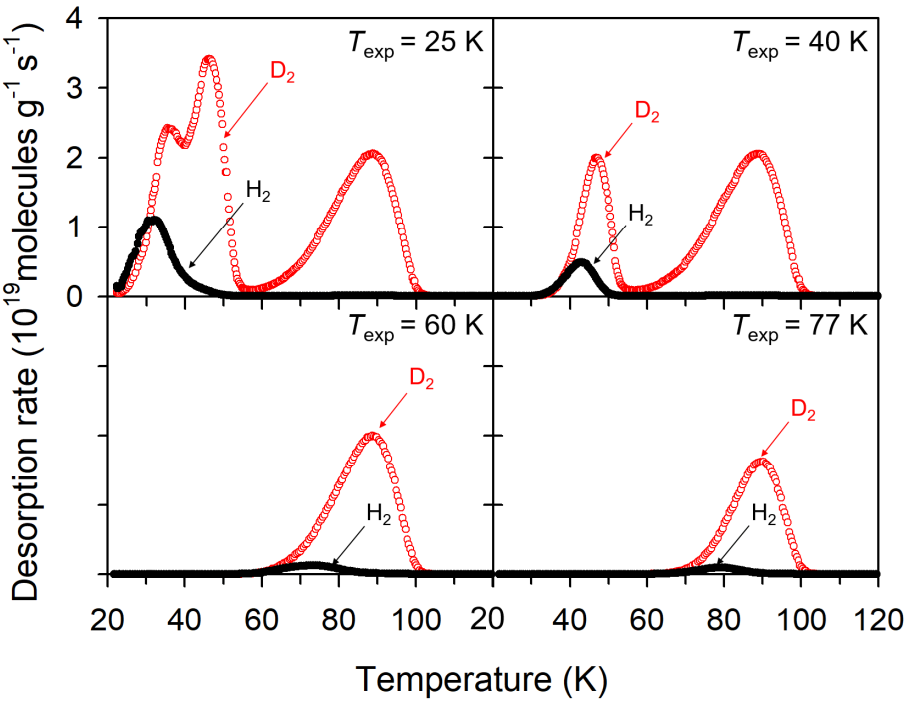

Figure 2.4.12 H_2 (black, filled circle) and D_2 (red, open circle) desorption spectra of 10 mbar (1:1 D_2/H_2 mixture) loading on MOF-74-ac with a heating rate of 0.1 K/s. Exposure temperature (T_{exp}) at 25 K, 40 K, 60 K, and 77 K.

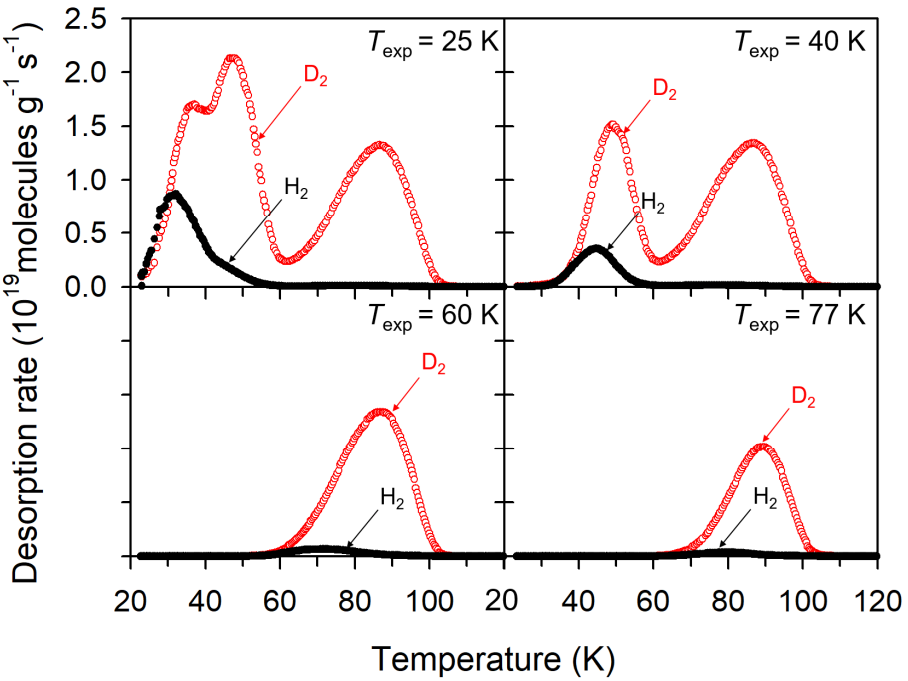

Figure 2.4.13 H_2 (black, filled circle) and D_2 (red, open circle) desorption spectra of 10 mbar (1:1 D_2/H_2 mixture) loading on MOF-74-IM-10 with a heating rate of 0.1 K/s. Exposure temperature (T_{exp}) at 25 K, 40 K, 60 K, and 77 K.

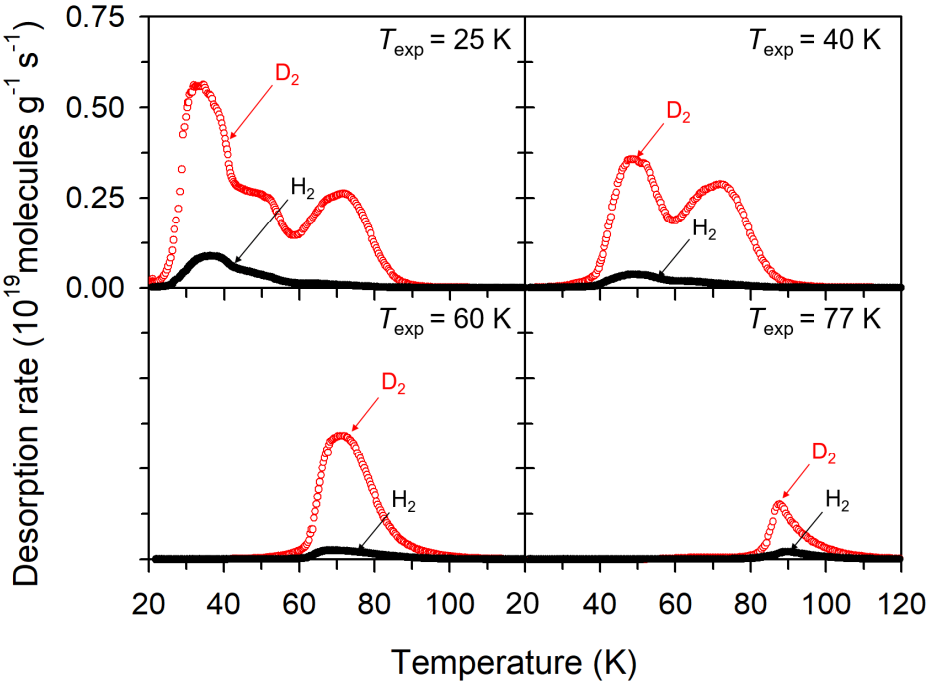

Figure 2.4.14 H_2 (black, filled circle) and D_2 (red, open circle) desorption spectra of 10 mbar (1:1 D_2/H_2 mixture) loading on MOF-74-IM-38 with a heating rate of 0.1 K/s. Exposure temperature (T_{exp}) at 25 K, 40 K, 60 K, and 77 K.

Separation performance of MOF-74-IM systems. Inspired by the co-existence of both quantum-sieving effects in MOF-74-IM systems, we further investigated the direct D_2/H_2 selectivity of MOF-74-IM systems and MOF-74-ac with TDS experiments. All samples were exposed to an equimolar D_2/H_2 isotope mixture at various exposure temperatures (T_{exp} = 25, 40, 60, and 77 K). The overall selectivity ($S_{D2/H2}$) and the corresponding amount of adsorbed D_2 of MOF-74-ac, MOF-74-IM-10 and MOF-74-IM-38 are presented in Figure 2.4.15. One should note that since the area under the desorption curves in TDS are proportional to the amount of desorbed gas, the ratio of these areas directly reflects the selectivity of D_2 over H_2. In addition, since all samples are exposed to the gas mixture first and then evacuated at the same target exposure temperature before the heating ramp is applied, any gas phase originally present in the chamber can be excluded and thus the obtained values suggest the actual gas amount originates only from adsorbed species and thus is a direct indication of the selectivity of WBSs and/or SBSs.

For MOF-74-ac, selectivity increases linearly from $S_{D2/H2}$ = 7 at a T_{exp} of 25 K to $S_{D2/H2}$ = 19 at a T_{exp} of 77 K. At higher T_{exp} (above 60 K), hydrogen isotopes can be only adsorbed on SBSs (see Figure 2.4.12), and these SBSs are preferentially occupied by deuterium, resulting in high selectivity. On the other hand, at lower T_{exp} (below 60 K), hydrogen isotopes can be adsorbed on both WBSs and SBSs, thus weakening the CAQS effect, resulting in a lower selectivity. MOF-74-IM-10 and MOF-74-IM-38 show

two distinct regions below and above T_{exp} = 60 K. Above 60 K, where gas adsorption only occurs at SBSs, the selectivity of MOF-74-IM-10 and MOF-74-IM-38 show large differences while similar selectivity is obtained below 60 K. With increasing temperature, the selectivity of MOF-74-IM-10 is greatly enhanced compared to that of the MOF-74-ac, resulting in $S_{D2/H2}$ = 26 at a T_{exp} of 77 K, whereas the selectivity MOF-74-IM-38 is significantly reduced to $S_{D2/H2}$ = 5 at a T_{exp} of 77 K. The greatly enhanced selectivity of MOF-74-IM-10 can be ascribed to the synergistic effect of KQS and CAQS, as was our aim. Introducing a diffusion barrier by incorporating small amounts (10%) of imidazole magnifies the difference in diffusion rates between H_2 and D_2 leading to improved accessibility of D_2 to the sorption site (KQS effect). Moreover, a relatively high density of SBSs in the MOF-74-IM-10 channels result in additional selectivity for D_2 adsorption due to the CAQS effect. One should note that this diffusion limitation, leading to the KQS effect, is more clearly observed with an increase in imidazole content. Reducing the exposure time from 120 min to 3 min for MOF-74-IM-38, enhances the selectivity both at 60 K and 77 K (Figure 2.4.16), implying that the kinetic effect still exists even at high temperature.

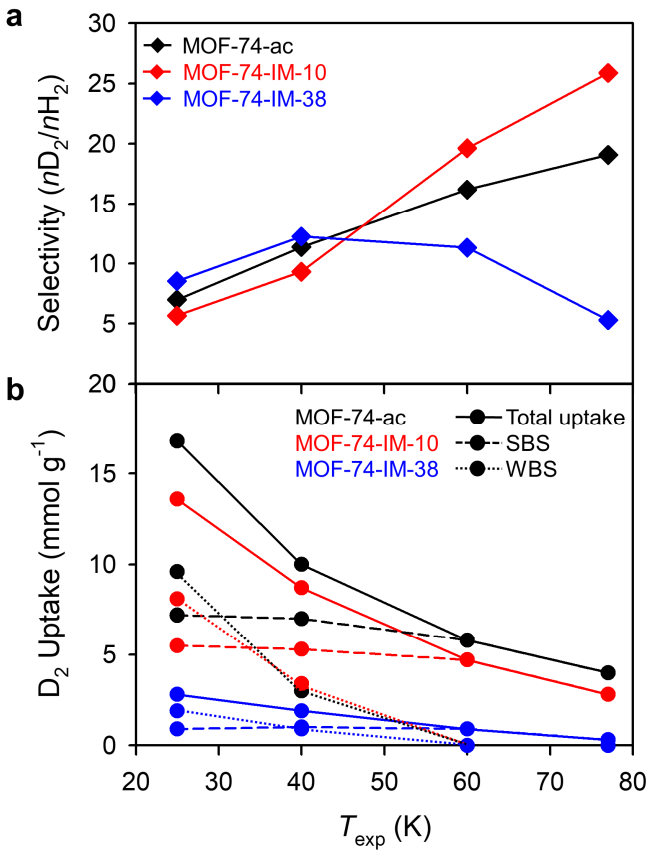

Figure 2.4.15 Adsorptive separation for an equimolar D_2/H_2 isotope mixture. (**a**) Selectivity for D_2 compared to H_2 and (**b**) D_2 uptake at strong binding sites (dashed line) and weak binding sites (dotted line) and total D_2 uptake (solid line) of MOF-74-ac (black), MOF-74-IM-10 (red), and MOF-74-IM-38 (blue) as a function of T_{exp}. At higher T_{exp} (above 60 K), D_2 adsorption only occurs at SBSs.

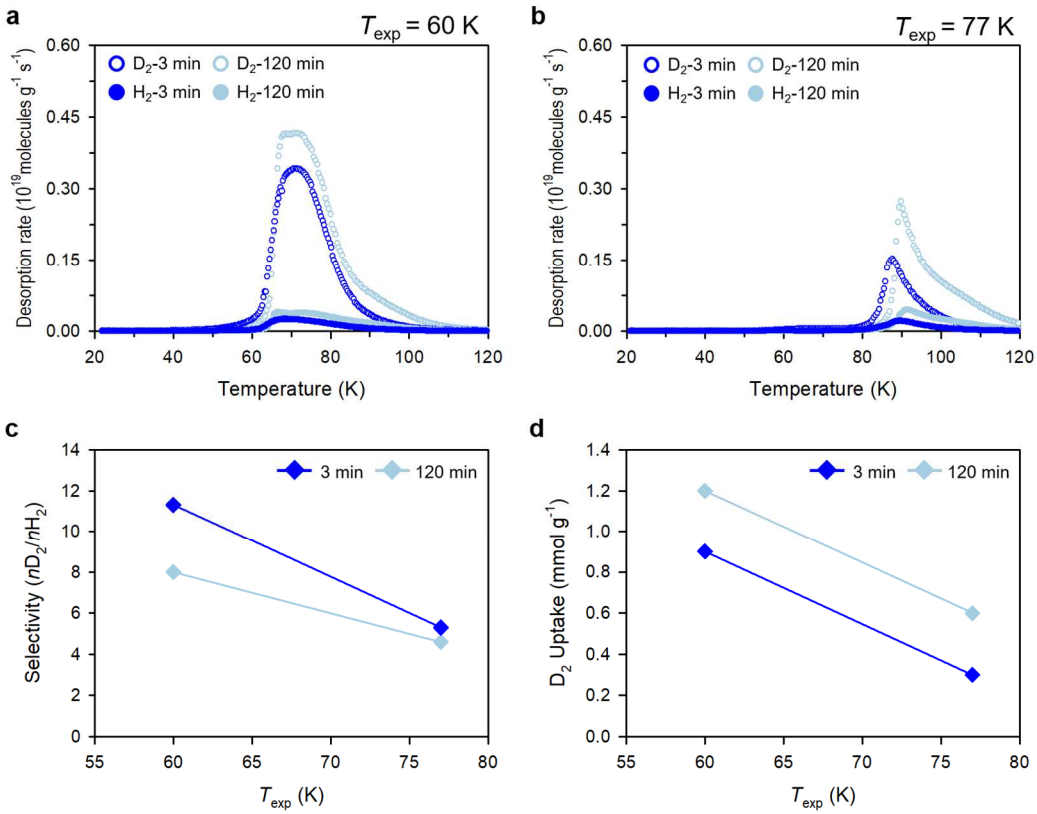

Figure 2.4.16 Kinetic effect of MOF-74-IM-38 at 60 K and 77 K. H_2 and D_2 desorption spectra of 10 mbar (1:1 D_2/H_2 mixture) loading on MOF-74-IM-38 with a different loading time (3 min and 120 min) at exposure temperature (T_{exp}) (a) 60 K and (b) 77 K and its corresponding (c) selectivity and (d) D_2 uptake.

The computational activation energy of H_2/D_2 in MOF-74-IM was found by density functional theory (DFT) calculations (Figures 2.4.17-2.4.20). The relaxed MOF-74-IM structure was calculated (Figure 2.4.17), and then the nudged elastic band (NEB) methods were utilized to explore the transition states of H_2/D_2 migration. Since there is no difference in the transition states of H_2 and D_2 using the classical method, the zero-point energy and formation energy of both H_2 and D_2 on the metal centre had to be considered (Figures 2.4.19 and 2.4.20). Due to the system limitation for designing MOF-74-IM periodic systems for gas diffusion studies, our model was simplified to characterize a gas molecule hopping circularly from one Ni^{2+} OMS to an adjacent site, rather than molecular transport into the MOF (Figure 2.4.18). It should be noted that D_2 selectivity calculation in the previous report typically considered coupling between the translation and orientation[49], whereas our calculation described in the present study exhibits only activation energy difference between isotopes. Nevertheless, this model still can indirectly provide insight into the effect of coordinated imidazole on gas migration. The calculated results exhibit a difference in the activation energy of 1.43 kJ mol^{-1}, implying that higher activation

energy was observed in H_2 than in D_2 (Figure 2.4.19 and 2.4.20). This difference is even higher than previous theoretical calculations performed with pristine MOF-74-Ni in which the difference of isosteric heats of adsorption was found to be 0.92 kJ/mol[27], consistent with our experimental observations. Thus, the diffusion of heavier isotopes in channels of MOF-74-IM is more energetically favourable than the diffusion of lighter isotopes. Although imidazole is useful to increase the activation energy difference between H_2 and D_2, increasing the amount of imidazole diminishes the CAQS effect due to the reduction of OMSs leading to a low selectivity and low D_2 separation capacity (see MOF-74-IM-38 in Figure 2.4.15). This indicates that the optimum imidazole amount should be considered for both selectivity and the amount of D_2 adsorbed. To the best of our knowledge, the experimental $S_{D2/H2}$ value of 26 for MOF-74-IM-10 (2.8 mmol/g of D_2 uptake) obtained at liquid nitrogen temperature is one of the highest reported $S_{D2/H2}$ experimental values among various porous adsorbents (Figure 2.4.21 and Table 2.4.3).

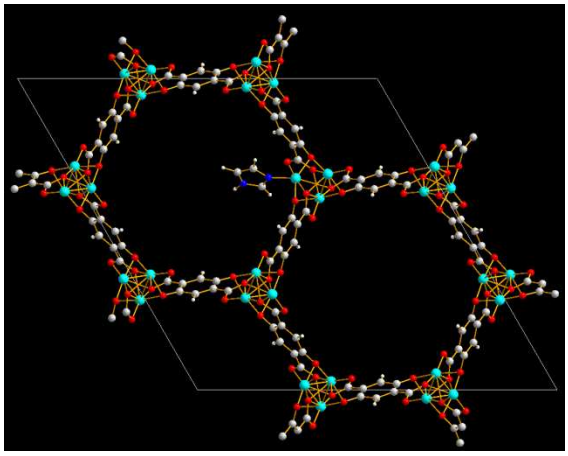

Figure 2.4.17 Relaxed atomic position of the MOF-74 channel with incorporating imidazole (IM) molecules. Color scheme: Ni, turquoise; O, red; N, blue; C, grey; and H, white.

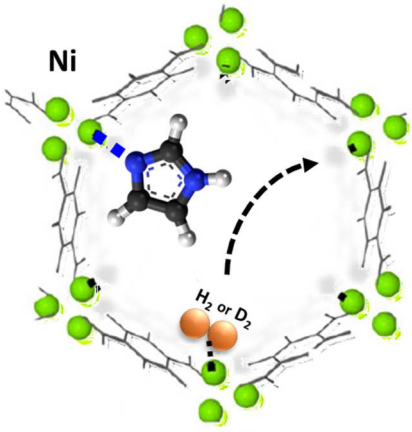

Figure 2.4.18 Graphical representation of the migration mechanisms of H_2 or D_2 considered in this study.

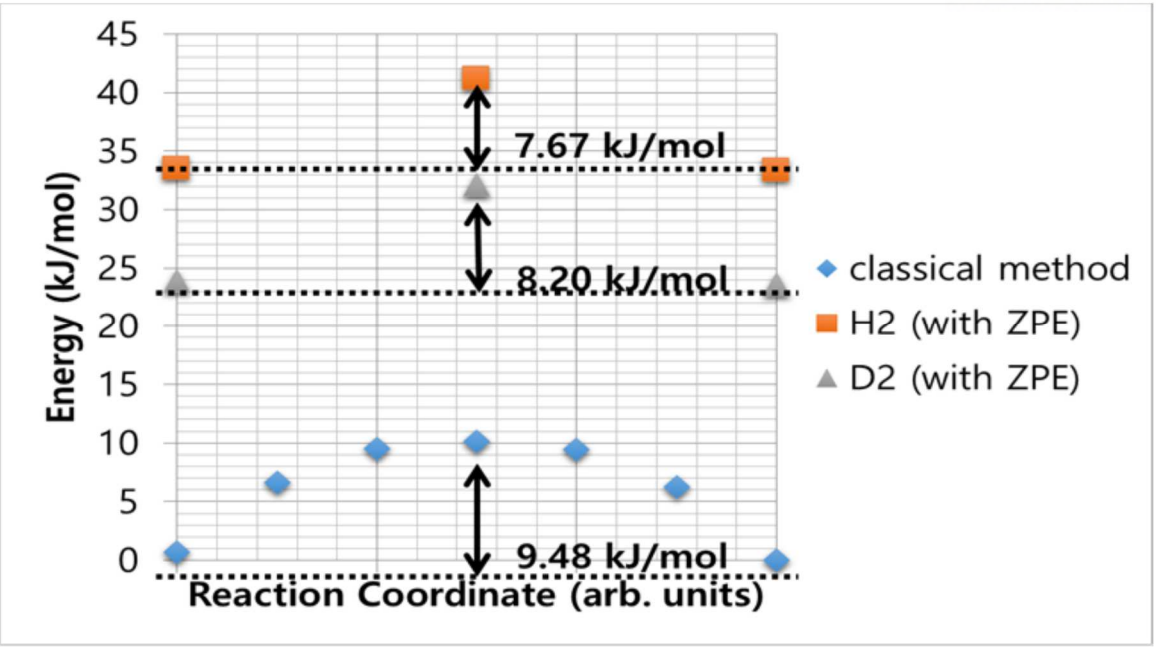

Figure 2.4.19 The migration profile of H_2/D_2 using classical method and zero point energy corrected migration energy of H_2/D_2 in kJ/mol.

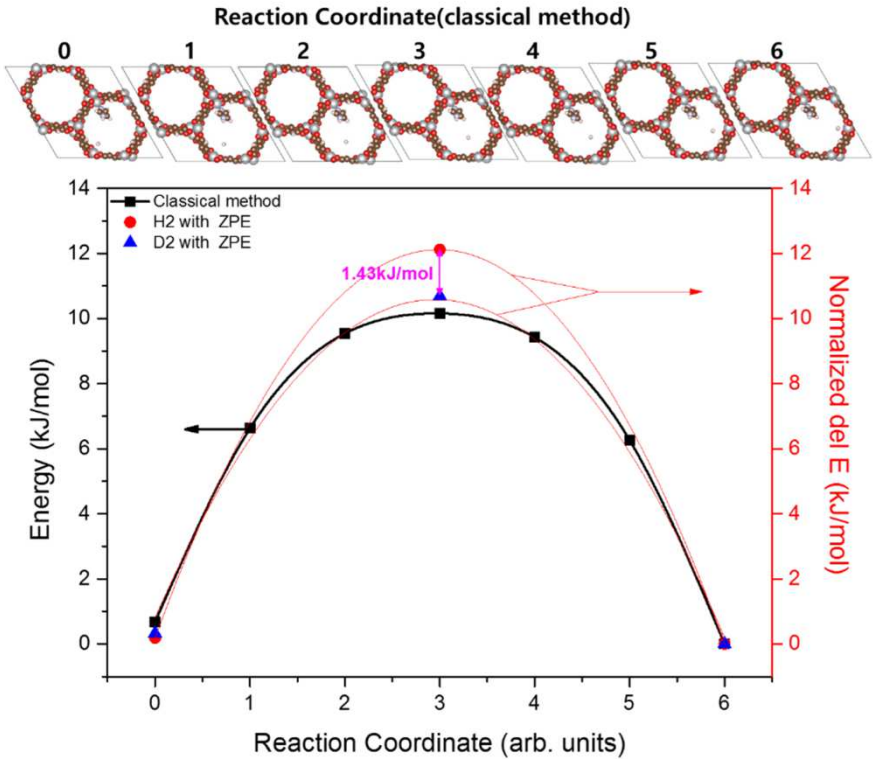

Figure 2.4.20 Migration progress coordinates of hydrogen isotope molecule through MOF-74-IM. Seven figures show the initial (0) → transition (1-5) → final state (6) of hydrogen isotope (classical method).

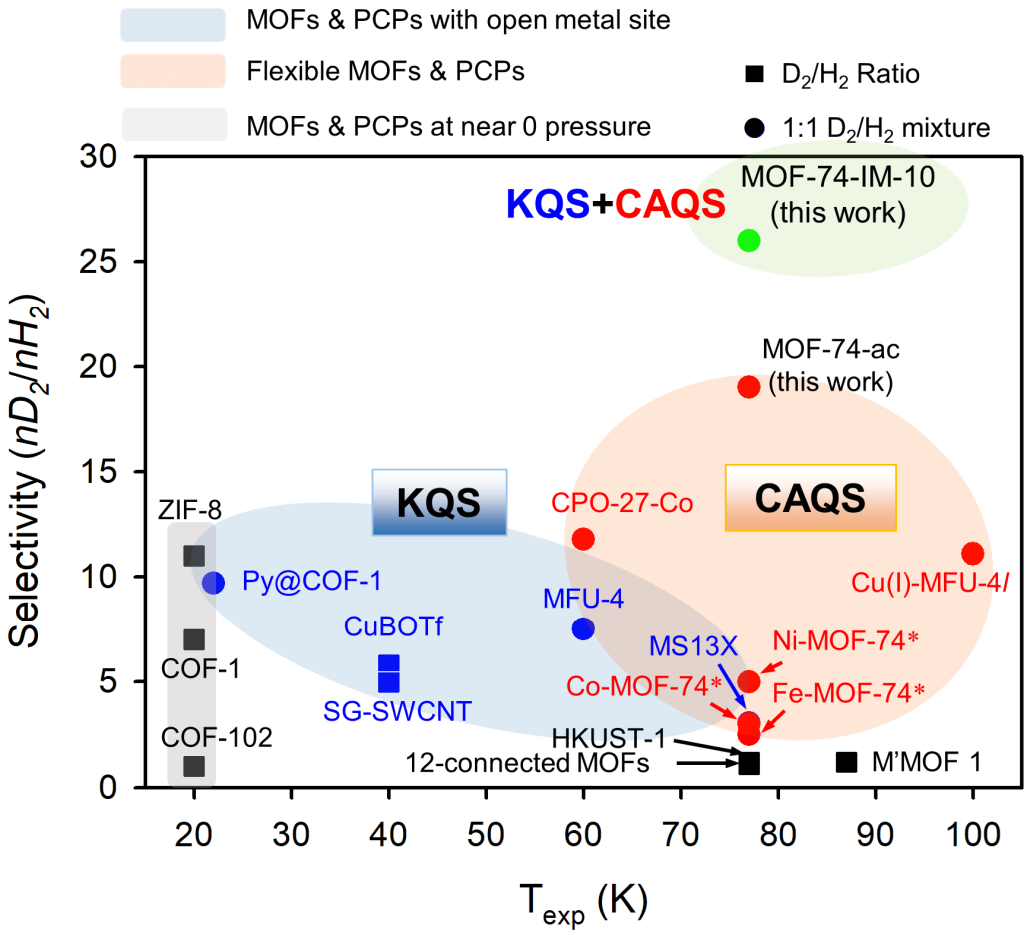

Figure 2.4.21 Comparison of MOF-74-IM-10 with various porous frameworks for hydrogen isotope separation as a function of working temperature.[15] (Note: *1:1 D_2/H_2 mixture selectivity calculated from pure gas sorption isotherms using idealized adsorption solution theory (IAST) methods)

Table 2.4.3 Summary of hydrogen isotope separation factors for various porous frameworks as a function of working temperature.

Compound	T (K)	P (mbar)	R (nD_2/nH_2)	$S_{D2/H2}$ (1:1 mixture)	D_2 uptake (mmol/g)	Ref
MOF-74-IM-10	77	10	-	26	2.8	This work
MOF-74-ac	77	10	-	19	4.0	This work
SG-SWCNT	40	0.5	5	-	-	19
MS13X	77	5	-	3.05	0.61	49
M'MOF 1	87	1	1.2	-	0.68[a]	23
12-connected MOFs	77	1,000	1.1	-	11.10[a]	50
HKUST-1	77	20	1.2	-	2.39[a,b]	51
ZIF-8	20	NZP[c]	11	-	-	26
COF-1	20	NZP[c]	7	-	-	26
COF-102	20	NZP[c]	1	-	-	26
Ni-MOF-74	77	NZP[c]	4.6	5[d]	-	27
Co-MOF-74	77	NZP[c]	3.2	3[d]	-	27
Fe-MOF-74	77	NZP[c]	2.5	2.5[d]	-	27
CPO-27-Co	60	30	-	11.8	2.80[b]	28
MFU-4	60	4-20	-	7.5	1.30	11
Py@COF-1	22	26	-	9.7	0.70[b]	12
CuBOTf	40	20	5.8	-	1.30	24
Cu(I)-MFU-4*l*	100	-	-	11.1	-	30

[a] Sorption uptake (mmol/g) from pure D_2 sorption isotherm measurement at exposed pressure. [b] Sorption amount estimated from pure D_2 sorption isotherm graph. [c] Near zero pressure. [d] 1:1 mixture selectivity obtained by applying ideal adsorbed solution theory (IAST) from the pure gas adsorption isotherms.

2.4.4. Conclusion

In summary, we demonstrated that deuterium could be efficiently separated and stored inside the pores of the MOF-74-IM system by implementing two quantum-sieving effects in one system. The simple post modification strategy of introducing imidazole molecules into the highly dense OMS channels of MOF-74 eliminates the need for complex design and synthesis of new MOF structures to optimize the aperture size and increase the internal binding energy, simultaneously, and is also applicable to other gas mixture separation such as tritium, deuterium and hydrogen mixtures or He isotopic mixtures. Imidazole molecules are able to repeatedly block the diffusion of lighter isotopes into the 1D channels of MOF-74, acting as a diffusion barrier, while the strong binding sites of the MOF can selectively adsorb heavier isotopes. By optimizing the amount of coordinated imidazole molecules *via* a post synthetic strategy, the synergistic effect of KQS arising from the kinetic diffusion barrier and CAQS arising from the presence of open metal sites yields an impressively high selectivity of ~26 even at high temperatures (77 K) with high D_2 uptake (2.84 mmol g^{-1}). We believe that this strategy of combining KQS and CAQS in one system will provide new opportunities for the intelligent design of porous materials leading to the development of other highly efficient isotope and gas separation systems.

2.4.5 References

1. Stiopkin, I. V.; Weeraman, C.; Pieniazek, P. A.; Shalhout. F. Y.; Skinner, J. L.; Benderskii, A. V. *Nature* **2011**, *474*, 192.
2. Povinec, P. P.; Bokuniewicz, H.; Burnett, W. C.; Cable, J.; Charette, M.; Comanducci, J. –F.; Kontar, E. A.; Moore, W. S.; Oberdorfer, J. A.; Oliveira, J. de.; Peterson, R.; Stieglitz, T.; Taniguchi, M. *J. Environ. Radioactiv.* **2008**, *99*, 1596.
3. Keppler, F.; Hamilton, J. T. G.; McRoberts, W. C.; Vigano, I.; Braß, M.; Röckmann, T. *New Phytol.* **2008**, *178*, 808.
4. Zaccai, G. *Science* **2002**, 288, 1604.
5. Büldt, G.; Gally, H. U.; Seelig, A.; Seelig, J.; Zaccai, G.; *Nature* **1978**, *271*, 182.
6. Machida, A.; Saitoh, H.; Sugimoto, H.; Hattori, T.; Sano-Furukawa, A.; Endo, N.; Katayama, Y.; Lizuka, R.; Sato, T.; Matsuo, M.; Orimo, S-i,; Aoki, K. *Nat. Commun.* **2014**, *5*, 5063.
7. Miller, A. I. *Can. Nuclear Soc. Bull.* **2001**, *22*, 1.
8. Rae, H. K. Selecting Heavy Water Processes. In *Separation of Hydrogen Isotopes*; American Chemical Society: Washington, DC, 1978; Vol. 68, pp 1-26.
9. Lozada-Hidalgo, M.; Hu, S.; Marshall, O.; Mishchenko, A.; Grigorenko, A. N.; Dryfe, R. A. W.; Radha, B.; Grigorieva, I. V.; Geim, A. K. *Science* **2016**, *351*, 68.
10. Beenakker, J. J. M.; Borman, V. D.; Krylov, S. Y. *Chem. Phys. Lett.* **1995**, *232*, 379.
11. Teufel, J.; Oh, H.; Hirscher, M.; Wahiduzzaman, M.; Zhechkov, L.; Kuc, A.; Heine, T.; Denysenko, D.; Volkmer, D. *Adv. Mater.* **2013**, *25*, 635.
12. Oh, H.; Kalidindi, S. B.; Um, Y.; Bureekaew, S.; Schmid, R.; Fischer, R. A.; Hirscher, M. *Angew. Chem. Int. Ed.* **2013**, *52*, 13219.
13. Cai, J.; Xing, Y.; Zhao, X. *RSC Adv.* **2012**, *2*, 8579.
14. Kowalczyk, P.; Terzyk, A. P.; Gauden, P. A.; Furmaniak, S.; Pantatosaki, E.; Papadopoulos, G. K. *J. Phys. Chem. B* **2015**, *119*, 15373.
15. Hattori, Y.; Tanaka, H.; Okino, Fl.; Touhara, H.; Nakahigashi, Y.; Utsumi, S.;; Kanoh, H.; Kaneko, K. *J. Phys. Chem. B* **2006**, *110*, 9764.
16. Zhao, X.; Villar-Rodil, S.; Fletcher, A. J.; Thomas, K. M. *J. Phys. Chem. B* **2006**, *110*, 9947.

17. Tanaka, H.; Kanoh, H.; Yudasaka, M.; Lijima, S.; Kaneko K. *J. Am. Chem. Soc.* **2005**, *127*, 7511.

18. Nguyen, T. X.; Jobic, H.; Bhatia, S. K. *Phys. Rev. Lett.* **2010**, *105*, 085901.

19. Noguchi, D.; Tanaka, H.; Fujimori, Tl.; Kagita, H.; Hattori, Y.; Honda, H.; Urita, K.; Utsumi, S.; Wang, Z-m,; Ohba, T.; Kanoh, H.; Hata, K.; Kaneko, K. *J. Phys.: Condens. Matter* **2010**, *22*, 334207.

20. Kumar, A. V. A.; Bhatia, S. K. *Phys. Rev. Lett.* **2005**, *95*, 245901.

21. Kumar, A. V. A.; Jobic, H.; Bhatia, S. K. *Adsorption* **2007**, *13*, 501.

22. Niimura, S.; Fujimori, T.; Minami, D.; Hattori, Y.; Abrams, L.; Corbin, D.; Hata, K.; Kaneko, K. *J. Am. Chem. Soc.* **2012**, *134*, 18483.

23. Chen, B.; Zhao, X.; Putkham, A.; Hong, K.; Lobkovsky, E. B.; Hurtado, E. J.; Fletcher, A. J.; Thomas, K. M. *J. Am. Chem. Soc.* **2008**, *130*, 6411.

24. Noguchi, D.; Tanaka, H.; Kondo, A.; Kajiro, H.; Noguchi, H.; Ohba, T.; Kanoh, H.; Kaneko, K. *J. Am. Chem. Soc.* **2008**, *130*, 6367.

25. Liu, D.; Wang, W.; Mi, J.; Zhong, C.; Yang, Q.; Wu, D. *Ind. Eng. Chem. Res.* **2012**, *51*, 434.

26. Oh, H.; Park, K. S.; Kalidindi, S. B.; Fischer, R. A.; Hirscher, M. *J. Mater. Chem. A* **2013**, *1*, 3244.

27. FitzGerald, S. A.; Pierce, C. J.; Rowsell, J. L.; Bloch, E. D.; Mason, J. A. *J. Am. Chem. Soc.* **2013**, *135*, 9458.

28. Oh, H.; Savchenko, I.; Mavrandonakis, A.; Heine, T.; Hirscher, M. *ACS nano* **2014**, *8*, 761.

29. Savchenko, I.; Mavrandoaski, A.; Heine, T.; Oh, H.; Teufel, J.; Hirscher, M. *Micropor. Mesopor. Mater.* **2015**, *216*, 133.

30. Weinrauch, I.; Savchenko, I.; Denysenko, D.; Souliou, S. M.; Kim, H. -H.; Tacon, M. L.; Daemen, L. L.; Cheng, Y.; Mavrandonakis, A.; Ramirez-Cuesta, A. J.; Volkmer, D.; Schütz, G.; Hirscher, M.; Heine, T. *Nat. Commun.* **2017**, *8*, 14496.

31. Suh, M. P.; Park, H. J.; Prasad, T. K.; Lim, D. W. *Chem. Rev.* **2011**, *112*, 782.

32. Cheon, Y. E.; Suh, M. P. *Chem. Commun.* **2009**, 2296.

33. Yang, Q.; Zhong, C. *J. Phys. Chem. B* **2006**, *110*, 655.

34. Zhou, W.; Wu, H.; Yildirim, T. *J. Am. Chem. Soc.* **2008**, *130*, 15268.

35. Cadot, S.; Veyre, L.; Luneau, D.; Farrusseng, D.; Quadrelli, E. A. *J. Mater. Chem. A* **2014**, *2*, 17757.

36. Kresse, G.; Furthmüller, J. *Phys. Rev. B* **1996**, *54*, 11169

37. Kresse, G.; Furthmüller, J. *Comp. Mater. Sci.* **1996**, *6*, 15.

38. Perdew, J. P.; Burke, K.; Ernzerhof, M. *Phys. Rev. Lett.* **1996**, *77*, 3865.

39. Grimme, S.; Antony, J.; Ehrlich, S.; Krieg, H. *J. Chem. Phys.* **2010**, *132*, 154104

40. Monkhorst, H. J; Pack, J. D. *Phys. Rev. B* **1976**, *13*, 5188.

41. Dudarev, S. L.; Botton, G. A.; Savrasov, S. Y.; Humphreys, C. J.; Sutton, A. P. *Phys. Rev. B* **1998**, *57*, 1505.

42. Wang, L.; Maxisch, T.; Ceder, G. *Phys. Rev. B* **2006**, *73*, 195107.

43. Henkelman, G.; Uberuaga, B. P.; Jónsson, H. *J. Chem. Phys.* **2000**, *113*, 9901.

44. González, M.; Lemus-Santana, A. A.; Rodríguez-Hernández, J.; Knobel, M.; Reguera, E. *J. Solid State Chem.* **2013**, *197*, 317.

45. Ramasamy, R. *Armen. J. Phys.* **2015**, *8*, 51.

46. Chavan, S.; Bonino, F.; Valenzano, L.; Civalleri, B.; Lamberti, C.; Acerbi, N.; Cavka, J. H.; Leistner, M.; Bordiga, S. *J. Phys. Chem. C* **2013**, *117*, 15615.

47. Gallo, E.; Lamberti, C.; Glatzel, P. *Inorg. Chem.* **2013**, *52*, 5633.

48. Liu, Y.; Kabbour, H.; Brown, C. M.; Neumann, D. A.; Ahn, C. C. *Langmuir* **2008**, *24*, 4772.

49. Qu, Y.; Li, F.; Zhou, H.; Zhao, M. *Sci. Rep.* **2016**, *6*, 19952.

Chapter III. Versatile Processing of Metal-Organic Framework-Fluoropolymer Composite Inks with Chemical-Resistance and Sensor Applications

3.1 Introduction

High functionality and structural diversity of metal-organic frameworks (MOFs) have enticed material scientists as well as inorganic chemists into this research area.[1-5] In the early days of MOF research, establishing synthetic methods and understanding its physical and chemical properties were of main interest.[6,7] With passage of time, a variety of MOF uses have been explored such as hydrogen[8] and methane storage,[9] carbon dioxide capturing,[10] small molecule separation membranes,[11] catalysts,[12] drug delivery systems,[13] and sensors[14,15]. Some of these applications are still under investigation,[16,17] while some others have been abandoned due to intrinsically vulnerable properties of MOFs and the difficulty of shaping the powders. The challenges facing MOF applications are mainly poor processability as well as hydrolytic, chemical, thermal, and mechanical instabilities,[18-21] and these limitations have often rendered well-designed multi-functional MOFs practically useless.

Early research of MOF shaping were mainly done in its patterning and spraying on substrates, and those techniques were conducted by using MOF precursor solutions, followed by crystallization upon solvent evaporation.[22-24] Later, in order to improve the mechanical reliability and the processibility required in applications, various type of polymers were mixed with MOF crystals, formulating MOF-polymer composites, which were mostly used to produce MOF-based mixed matrix membranes.[25-32] However, in the membranes, the polymer matrix mainly played a role of a binder, and thus often did not efficiently shield the chemical vulnerability of the MOFs in water and harsh chemical environments. In addition, increasing the amount of MOF loading in the composites is one of the important issues to utilize it. Therefore, in order to further expand and bring forth novel MOF-polymer based applications beyond mixed matrix membrane, an ideal polymer matrix having chemical stability and compatibility with various MOFs is still required for versatile processibility and long-term stability of the formed objects, even under wet or humid environment, for the development of MOF-based devices and for the realization of various applications.

Here, we report a new class of MOF-polymer composite ink, which is highly versatile to process coating, pattern, and 3D structures at ambient temperature via spray-coating, pen writing, stencil printing, and moulding techniques (Figure 3.1). In the MOF ink, water-repellent, photocurable methacrylate-terminated perfluoropolyether (PFPE) is introduced, which is widely compatible to various type of MOFs, achieving high loading up to 90 wt%, and provides a robust shielding matrix against moisture and chemicals. It is well-documented that the cured PFPE has high elasticity, gas permeability, transparency, and solvent resistance.[33,34] Note that the methacrylate-terminated fluoropolymer can be simply consolidated by UV radiation with no thermal treatment, allowing the use of various substrates.

In addition, the composite inks formulated with MOFs are used to manufacture two types (coated, patterned) of chemosensors to detect volatile organic compounds (VOCs) in water, and also a thermosensor to visualize temperature profiles in various organic, acidic, and basic solutions. Thus, our newly formed chemical-resistant MOF ink greatly expands the usability of MOFs for a wide variety of novel applications. The facile processability and chemical/mechanical durability greatly enhance the feasibility of diverse MOF-based applications.

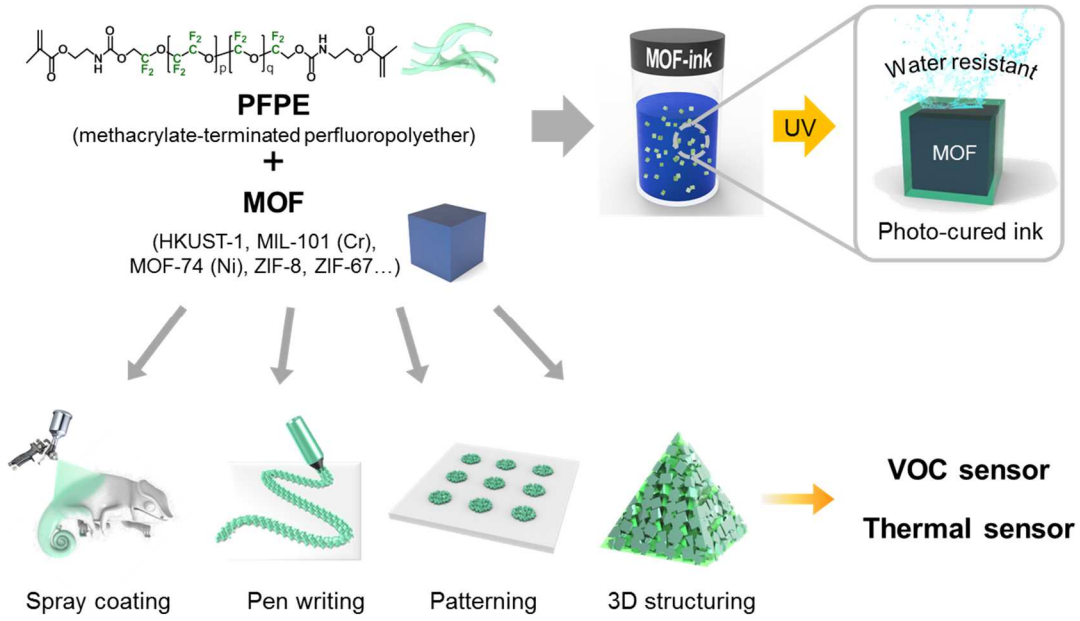

Figure 3.1 Schematic illustration of the preparation of MOF-fluoropolymer composite inks to form diverse structures via various processing techniques, and its use for sensor applications.

3.2 Experimental Section

Materials and characterization. All chemicals and solvents were of reagent grade and were used as received without further purification. PFPE (Fluorolink MD 700, viscosity 581 cP and Molecular weight: ca. 2000 g mol^{-1}) was received from Solvay-Solexis (Milan, Italy); 2-hydroxy-2methyl-1-phenyl-propan-1-one (Darocur 1173) as a photoinitiator was received from BASF (Ludwigshafen, Germany). XRPD patterns were collected on a Bruker D8 advance diffractometer at 40 kV and 40 mA for Cu Kα (λ = 1.54050 Å), with a step size of 0.02° in 2θ. Fourier transformed-Infrared (FT-IR) spectra were recorded on a ThermoFisher Scientific Nicolet 6700 FT-IR spectrometer. Scanning electron microscope (SEM) images were taken using a Hitach High-Technologies Cold FE-SEM operating at 10 kV. High-resolution transmission electron microscopy (HR-TEM) images were taken using a JOEL JEM-2200FS HRTEM. The nitrogen adsorption-desorption isotherms were obtained using a BELSORP-max at 77 K. Prior to the adsorption measurements, all samples (~100 mg) were evacuated (p < 10-5 mbar) at 393 K for 5 h. The specific surface area was obtained by the Brunauer-Emmett-Teller (BET) method. Fluorescence spectra were corrected at excitation 365 nm in 1 cm quartz cuvettes containing a suspension of the dispersed powder in the guest solvent using a Varian Cary Eclipse. The dispersed powder samples were prepared by sonication for 10 min. Fourier-transform nuclear magnetic resonance (FT-NMR) spectra were recorded on an Agilent 400 MHz spectrometer.

Synthesis of MOFs

Synthesis of HKUST-1[35] : $Cu(NO_3)_2 \cdot 2.5H_2O$ (2.35 g, 10.5 mmol) and trimesic acid (1.16 g, 5.52 mmol) were dissolved in dimethyl sulfoxide (5 mL) and dropped into methanol (500 mL) under stirring during 1 min. After additional stirring for 10 min, the light blue powder was collected by centrifugation, washed 3 times with methanol, and dried at 120 ^oC overnight under vacuum.

Synthesis of MIL-101(Cr)[29] : The aqueous suspension (25 mL) containing $Cr(NO_3)_3 \cdot 9H_2O$ (2.00 g, 5.0 mmol), terephthalic acid (0.83 g, 5.0 mmol), and HF (0.18 mL of 48% soln, in water, 5.0 mmol) was placed in teflon lined stainless steel autoclave. The autoclave was heated at 220 ^oC for 8 h. After cooling to room temperature, green powder was collected by centrifugation, washed 3 times with DMF and washed 3 times with ethanol. The resulting green powder was dried overnight at room temperature.

Synthesis of ZIF-8[36]: To an aqueous solution (10 mL) containing 2-methylimidazole (2.24 g, 27.3 mmol), the solution of 10 mL H_2O containing $Zn(CH_3COO)_2 \cdot 2H_2O$ (0.60 g, 2.73 mmol) was added, stirred for 1 min, and kept for 3.5 hours. The resulting white powder was washed 3 times with methanol and dried under vacuum for 5 h at room temperature.

Synthesis of ZIF-67[36] : To an aqueous solution (5 mL) containing 2-methylimidazole (2.24 g, 27.3 mmol), the solution of 5 mL H_2O containing $Co(CH_3COO)_2 \cdot 4H_2O$ (0.60 g, 2.41 mmol) was added, stirred for 1 min, and kept for 10 min. The resulting purple powder was washed 3 times with methanol and dried under vacuum for 5 h at room temperature.

Synthesis of MOF-74 (Ni)[37] : The suspension of 15 mL H_2O containing 2,5-dioxido-1,4-benzenedicarboxylic acid (0.40 g, 2.0 mmol) was refluxed with stirring and an aqueous solution of $Ni(CH_3COO)_2 \cdot 4H_2O$ (1.00 g, 4.0 mmol) was added. The solution was stirred for 1 hour. After cooling to room temperature, yellow powder was collected by centrifugation, washed 3 times with H_2O and washed 3 times with ethanol. The resulting powder was dried for 5 hours at 250 ^oC, prior to further experiments.

Synthesis of $Zn_2(bdc)_2(dpNDI)$ (MOF_{chemo}): MOF_{chemo} was prepared by slightly modifying a reported method[38]. A suspension of 150 mL of *N*,*N'*-dimethylformamide (DMF) containing $Zn(CH_3COO)_2 \cdot 2H_2O$ (0.33 g, 1.5 mmol), terephthalic acid (H_2bdc) (0.25 g, 1.5 mmol), and *N*,*N'*-di(4-pyridyl)-1,4,5,8-naphthalenediimide (dpNDI) (0.63 g, 1.5 mmol) were placed in a 250 mL 2-neck round bottom flask equipped with a condenser. The suspension was heated at 95 ^oC for 24 h with vigorous stirring. After cooling to room temperature, ivory powder was collected by centrifugation at 7500 rpm, washed 3 times with DMF and washed 3 times with ethanol. The resulting powder was dried overnight at 120 ^oC under vacuum prior to further experiments.

Synthesis of $Tb_{0.99}Eu_{0.01}(hfa)_3(dpbp)$ (MOF_{thermo}): Synthesis of 4,4'-dibromobiphenyl : 4,4'-dibromobiphenyl was prepared by slightly modifying a reported method[39]. Biphenyl (3.10 g, 20.1 mmol) was placed in slightly opened 500 mL lab bottle and exposed to Br_2 (2.50 mL, 48.8 mmol) for 12 h with stirring. The products were recrystallized in benzene, filtered and washed with small amount of benzene and acetone, respectively. The resulting white crystals are dried overnight at 50 ^oC in vacuum oven. Yield: 5.4 g (86%). ^{1}H-NMR (400 MHz, $CDCl_3$) δ 7.55–7.58 (m, 4H), 7.40–7.43 (m, 4H) ppm.

Synthesis of 4,4′-bis(diphenylphosphoryl)biphenyl (dpbp)[40]: A solution of 4,4'-dibromobiphenyl (1.90 g, 6.1 mmol) in anhydrous tetrahydrofuran (30 mL) was stirred at -78 ^oC in an Ar(g) atmosphere, treated dropwise with a n-BuLi (9.3 mL, 1.6 M hexane, 14.9 mmol), and stirred for 15 min. The mixture was heated to -10 ^oC and stirred additionally for 3 h. The mixture was cooled again to -78 ^oC, then PPh_2Cl (2.7 mL, 14.6 mmol) was added dropwise and stirred for 14 h to gradually rise to room temperature. The resulting product was extracted with ethyl acetate, washed with brine, and dried over $MgSO_4$. After evaporation of ethyl acetate, the white product was washed with ethanol and acetone. The white product was dissolved in dichloromethane (40 mL), treated with H_2O_2 aqueous solution (5 mL, 30%) at 0 ^oC, and stirred for 3 h. The resulting product was extracted with dichloromethane, washed with brine, and dried over $MgSO_4$. Finally, the white product was obtained after solvent evaporation

and recrystallized from dichloromethane and ethanol. Yield: 2.3 g (69%). ^{1}H-NMR (400 MHz, $CDCl_3$) δ 7.67–7.80 (m, 16H), 7.45–7.60 (m, 12H) ppm.

MOF_{thermo} was prepared by slightly modifying a reported method with prepared dpbp ligand[41]. A solution of 30 mL methanol containing 4,4′-bis(diphenylphosphoryl)biphenyl (dpbp) (0.61 g, 1.17 mmol), $Tb(hfa)_3(H_2O)_3$ (0.92 g, 1.10 mmol), and $Eu(hfa)_3(H_2O)_2$ (0.0091 g, 0.011 mmol) was refluxed for 2 h. The resulting white powder was filtered, washed with methanol and $CHCl_3$, respectively. The product was dried overnight at 50 °C in vacuum oven prior to further experiments.

Preparation of s-MOF-inks

Preparation of s-$MOF_{HKUST-1(90)}$–inks: The dried powder of HKUST-1 (0.9 g) was suspended in 5 mL ethanol under sonication for 10 min, and the 0.1 g of PFPE was added. After additional sonication for 10 min, s-$MOF_{HKUST-1(90)}$-ink was prepared.

Preparation of the series of s-$MOF_{(70)}$-inks: In order to process the s-$MOF_{(70)}$-inks into thin film, pen writing, and stencil printing, 5 types of s-$MOF_{(70)}$-inks (s-$MOF_{HKUST-1(70)}$-ink, s-$MOF_{MIL-101(Cr)(70)}$-ink, s-$MOF_{ZIF-67(70)}$-ink, s-$MOF_{ZIF-8(70)}$-ink, and s-$MOF_{MOF-74(Ni)(70)}$-ink) were prepared. The 0.20 g of dried MOF powder was suspended in 5 mL ethanol under sonication for 10 min, and 0.086 g of PFPE was added. After additional sonication for 10 min, s-$MOF_{(70)}$-ink containing 70 wt% of the MOF was prepared.

Preparation of s-$MOF_{HKUST-1(30)}$-ink for 3D structures: The dried powder of HKUST-1 (0.30 g) was suspended in 5 mL ethanol under sonication for 10 min, and the 0.7 g of PFPE was added. After additional sonication for 10 min, s-$MOF_{HKUST-1(30)}$-ink containing 30 wt% of the MOF was prepared.

Preparation of s-$MOF_{chemo(70)}$-ink: The dried powder of MOF_{chemo} (0.10 g) was suspended in ethanol or dichloromethane (1.5 mL) under sonication for 10 min. To this suspension was added a 0.5 mL ethanol or dichloromethane solution containing PFPE (0.043 g). After sonication for 10 min, s-$MOF_{chemo(70)}$-ink containing 70 wt% of the MOF was prepared.

Preparation of s-$MOF_{thermo(10)}$-ink: Dried powder of MOF_{thermo} (0.10 g) was suspended in dichloromethane (0.9 mL) under sonication for 10 min, and subsequently PFPE (0.90 g) was added. After sonication for 10 min, s-$MOF_{thermos(10)}$-ink containing 10 wt% of the MOF was prepared.

Preparation of s-$MOF_{thermo(10)}$-ink for 3D structures: MOF_{thermo} powder (0.50 g) and PFPE precursor (5.0 g) were mixed in volatile ethanol solvent (2 mL) at room temperature. After additional sonication for 30 min, s-$MOF_{thermo(10)}$-ink containing 10 wt% of the MOF was prepared.

Processing methods

Spray coating technique: In order to prevent the clogging of the outlet of the spray, 0.2 mL of ethanol solution containing 1 wt% of PVP was added to prepared 2.0 mL of s-$MOF_{(70)}$-ink and sonicated for 10 min. PVP added s-$MOF_{(70)}$-inks was spray coated on the hot substrates at 100 ^{o}C using a spray gun with a nozzle of 300 m diameter. The distance between the spray nozzle and the substrate was fixed at 10 cm and the angle was set to ~90^{o}. After coated, the MOF thin films were photocured for 10 min under 365 nm UV light.

Pen writing technique: For pen writing, 3.0 mL of s-$MOF_{HKUST\text{-}1(70)}$-ink was filled into the empty board marker pen. The MOFs ink was penetrated into the tip of board marker pen by capillary force. Afterwards, the s-$MOF_{HKUST(70)}$-ink was written on various substrates (paper, glass vial, cloth, and polyethylene film) through the pen tip of board maker and photocured for 10 min under 365 nm UV light.

Stencil printing technique : The stencil printing process was carried out by gently placing the target shaped stencil mask on the substrate. The prepared s-$MOF_{(70)}$-ink was dropped on the stencil mask with micro-patterns of circular shape (200 m in width, and 50 m in height), and dried in a vacuum for 10 min. After dried, stencil mask was removed and photocured for 10 min under 365 nm UV light.

Replica molding technique : In order to fabricate s-MOF-ink with the various shape of 3D structures, the three types of molds (hemisphere, square pyramid, and cuboid) with dimensions (0.5~1 cm in width, 5 mm in height) were prepared via 3D printing with polypropylene. The prepared s-MOF–ink was poured into the desired mold. The excess solvent was evaporated and the remaining d-MOF-ink was photocured for 10 min under 365 nm UV light. After photocured, 3D mold was removed.

Coating technique : The prepared s-$MOF_{thermo(10)}$-ink was coated to the glass rod, and stirring bar. After dried, coated surfaces were photocured for 10 min under 365 nm UV light.

VOCs sensing test with a $MOF_{chemo(70)}$-ink

Sensing pure VOC solvents: the p-$MOF_{chemo(70)}$-ink coated chameleon sensor was immersed in pure VOC solvent and immediately removed. The luminescence color change was monitored under excitation at 365 nm using a handheld UV lamp.

Sensing aqueous VOC (0.2 vol%) solution: The emulsion was prepared by 30 min sonication of 200 mL of water containing 0.4 mL VOC solvent. After sonication, the emulsion was stirred vigorously to

maintain a homogeneous distribution. To a vigorously stirred emulsion, the VOC-molecule patterned sensor on slide glass was immersed for 30 seconds and the luminescence color change was monitored under excitation at 365 nm using a handheld UV lamp. This was repeated 10 times for 5 min. (Figureures 3.13-16).

Thermal sensing test with a $MOF_{thermo(10)}$-ink

Safety test in chemical environments: the p-$MOF_{thermo(10)}$-ink coated stirring bar or p-MOF_{thermo}-ink slices were immersed for 5 min and the luminescence color change was monitored under excitation at 365 nm using a handheld UV lamp.

Testing the rapid change of luminescence color depending on the temperature: the luminescence color change of p-$MOF_{thermo(10)}$-ink was observed in real time while boiling water (100 ^{o}C) or ice water (0 ^{o}C) was poured into the cup.

Visualizing temperature gradient: oil bath (120 ^{o}C) was preheated and a cooling bath (-20 ^{o}C) was prepared by mixing 66 g of NaCl to 200 g of ice. The cooling bath and oil bath were placed at each end of the p-$MOF_{thermo(10)}$-ink coated glass road and the luminescence color change was monitored under excitation at 365 nm using a handheld UV lamp.

3.3 Results and Discussion

The MOF ink was prepared by a simple post-synthetic mixing method. First, to a MOF-dispersed ethanol or dichloromethane solution, a desired amount of methacrylate-functionalized PFPE (M_n = ~2000, viscosity = 581 cP) was added and mixed well to formulate the processing-ready MOF ink solution (designated as s-MOF-ink). The prepared s-MOF-ink was applied to form various structures using different processing methods as described in Figure 3.1. The excessive amount of volatile solvents was dried, yielding the solvent-free but viscous MOF ink (d-MOF-ink). Finally, the photocurable PFPE in the d-MOF-ink was crosslinked by exposing to UV radiation (λ = 365 nm) for 10 min to solidify the ink in the desired shape (p-MOF-ink).

To understand the chemistry of the composite ink, a moisture-sensitive HKUST-1 was chosen as a model MOF. When a 90/10 wt% HKUST-1/PFPE solution (s-$MOF_{HKUST-1(90)}$-ink) was prepared by the simple recipe of MOF ink, in which 1 g HKUST-1/PFPE was dispersed in 5 mL ethanol, the HKUST-1 nanocrystals mixed in the solution were well suspended with no flocculation during the processing time (Figure 3.2a). The solid loading up to 90 wt% of MOF particles in the ink is surprisingly high, offering a wide range of loading, which is advantageous for tuning the performance of MOF based devices. The excellent dispersion capability of PFPE to such a high loading of MOF crystals can be attributed to the significant interactions involving hydrogen bonds of terminal OH in the MOF surface with fluorine and oxygen on ether block of PFPE. In addition, the flexible conformation of the low molecular PFPE chain allows easy adaptation to the atomically rough morphology of the MOF surface, rendering a positive impact on the MOF/polymer compatibility.[42]

The p-$MOF_{HKUST-1(90)}$-ink obtained by solvent evaporation and photocuring had the same X-ray powder diffraction (XRPD) patterns as the pristine HKUST-1, indicating that its crystallinity was maintained (Figure 3.3**)**. Uniform nature of the crosslinked PFPE coated on the HKUST-1 nanocrystals was revealed by the scanning electron microscopy (SEM) images of the p-$MOF_{HKUST-1}$-ink (Figure 3.4), showing the original octahedral morphology of HKUST-1 due to excellent miscibility of MOFs and polymer. The transmission electron microscopy (TEM) image of the p-$MOF_{HKUST-1}$-ink clearly shows a uniform PFPE thin shell with a thickness over ~10 nm on the surface of the HKUST-1 nanocrystal (Figure 3.2b). The elemental mapping images of energy dispersive spectroscopy (EDS) in the figure also confirmed the homogeneous distribution of the polymer phase along the surface of MOF crystals, showing a completely integrated composite phase with compact interface.

Chemical etching of HKUST-1 core by immersing the p-$MOF_{HKUST-1(90)}$-ink in a piranha solution left only hollow PFPE shells in a selective manner, proving the robust chemical resistance and permeability of the PFPE that can act as a binder and protective shielding matrix (Figure 3.2c). Nitrogen sorption measurements of p-$MOF_{HKUST-1(90)}$-ink showed a decrease in surface area (1463 $m^2 g^{-1}$) compared to the

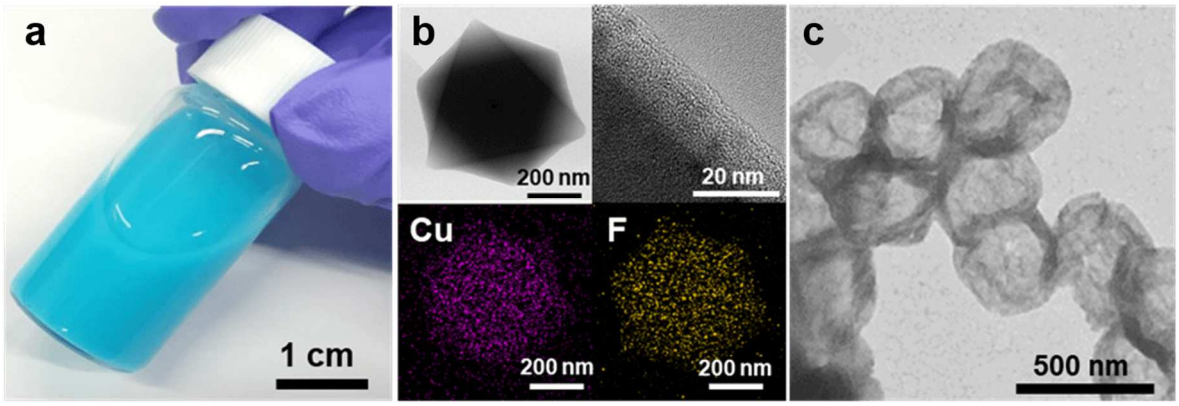

Figure 3.2 Characterization of $MOF_{HKUST\text{-}1(90)}$-ink with 90/10 wt% HKUST-1/PFPE. (a) Photograph of s-$MOF_{HKUST\text{-}1(90)}$-ink in a vial. (b) TEM images and EDS maps of Cu and F in photocured p-$MOF_{HKUST\text{-}1(90)}$-ink. The TEM image in the top-right is a magnified image of PFPE layer on HKUST-1 surface. (c) TEM image of hollow PFPE shell after selective etching of HKUST-1 in p-$MOF_{HKUST\text{-}1(90)}$-ink using piranha solution.

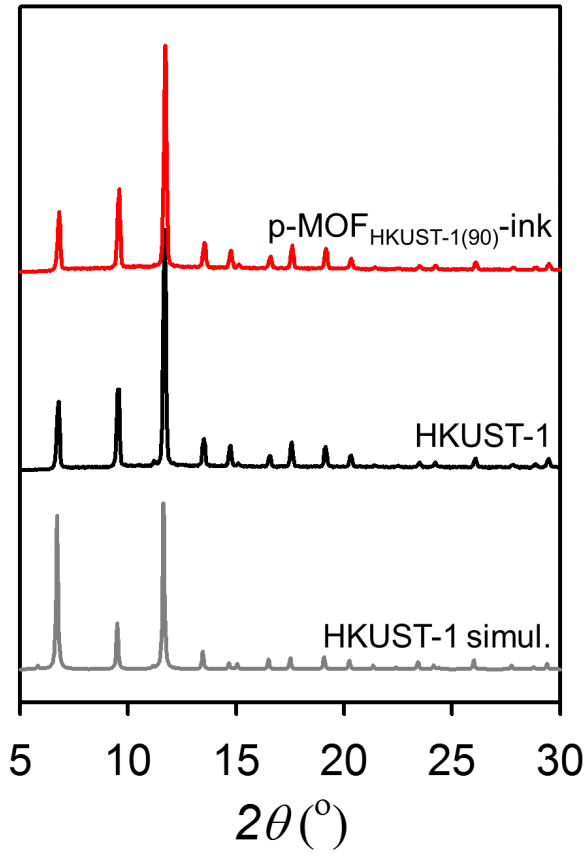

Figure 3.3 XRPD patterns of pristine HKUST-1 (middle) and p-$MOF_{HKSUT\text{-}1(90)}$-ink (top) compared with the simulated pattern of HKUST-1 (bottom).

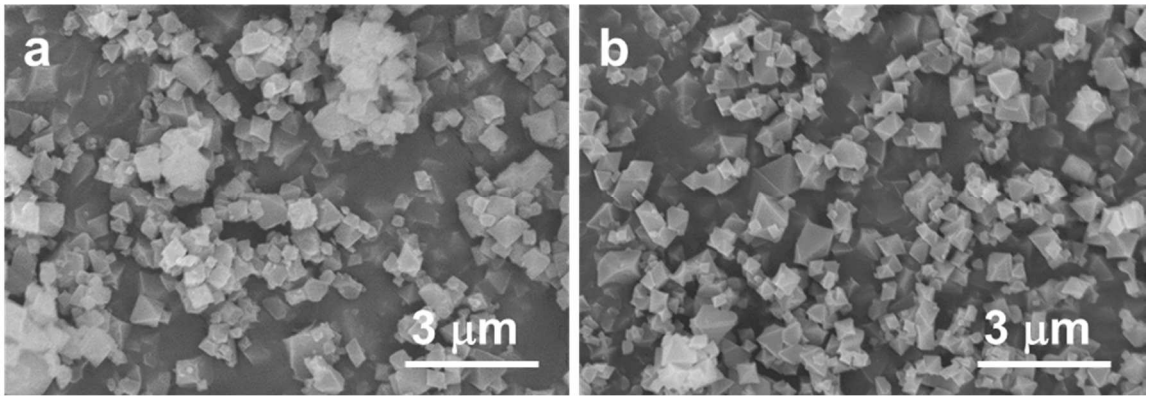

Figure 3.4 SEM images of a) pristine HKUST-1 and b) p-MOF$_{HKSUT-1(90)}$-ink.

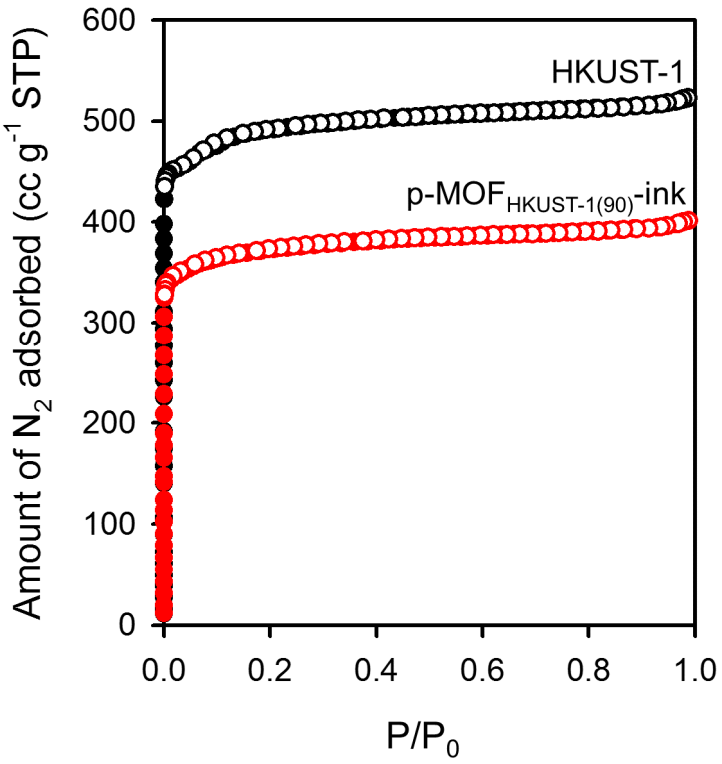

Figure 3.5 N_2 sorption isotherms of pristine HKUST-1 and p-MOF$_{HKSUT-1(90)}$-ink at 77 K.

pristine HKUST-1 (1956 $m^2 g^{-1}$) (Figure 3.5). In the highly compatible HKUST-1/PPFE composite phase, the labile polymer chain ends presumably penetrate into the surface MOF pores,[42] leading to the decrease. The reduced porosity, however, is sufficiently high enough to allow accessibility of small molecules through the permeable polymer shell. The balance between compatibility and performance shown by this MOF-fluoropolymer bodes well for applications.

The nature of chemical resistance, including water-repellency, of the highly fluorinated polymer, PFPE, is directly transferred to the MOF inks.[33,34] The static water contact angles of pristine HKUST-1 and p-$MOF_{HKUST-1(90)}$-ink films were measured and the results are shown in Figures 3.6a and b. The water drop on the HKUST-1 film instantly adsorbed, which prevented the measurement of contact angle and revealed the hydrophilic nature of MOFs. However, in the case of p-$MOF_{HKUST-1(90)}$-ink, the water drop remained on the surface and its contact angle was measured to be approximately 130°, indicating a dramatic increase in the hydrophobicity of the MOF ink. The hydrophobic polymer coating affords MOFs with much greater water stability compared to the bare MOFs. Indeed, the XRPD profiles and SEM images obtained after immersing in water for 1 day show that HKUST-1 completely converted into its hydrolyzed phase,[43] while p-$MOF_{HKUST-1(90)}$-ink maintained the original crystallinity and shape of HKUST-1 at least for a day (Figure 3.6c and Figure 3.7). As illustrated with HKUST-1, the simple incorporation of the water-repellent and photocurable PFPE into MOFs would not alter the inherent properties of both the MOF and PFPE.

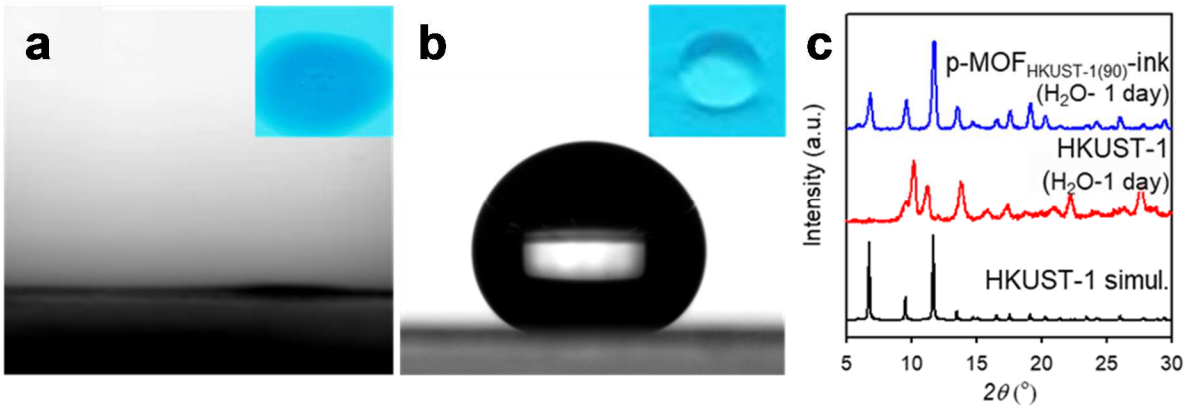

Figure 3.6 Contact angle measurements of (a) HKUST-1 and (b) p-$MOF_{HKUST-1(70)}$-ink. The inset images are the photographs of each sample after dropping water droplets. (c) XRPD profiles of HKUST-1 and p-$MOF_{HKUST-1(70)}$-ink after immersion in water for 1 day.

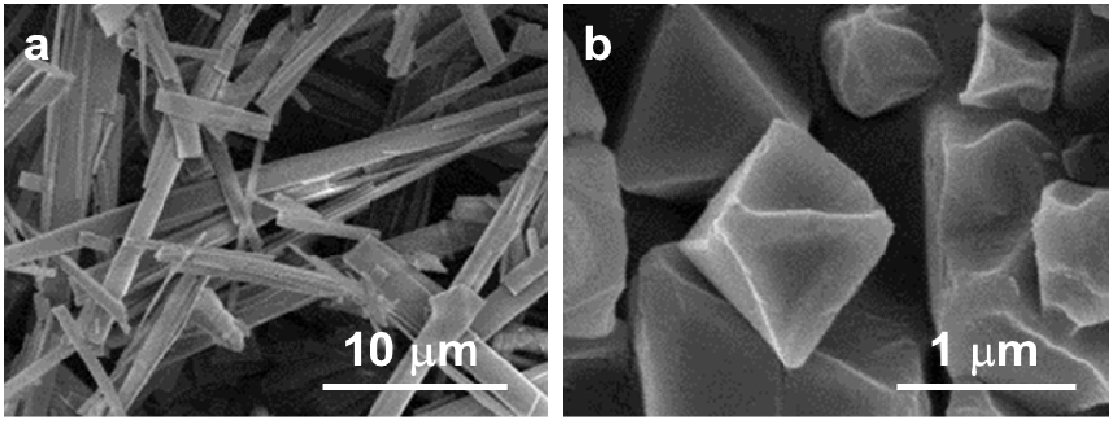

Figure 3.7 SEM images of a) pristine HKUST-1 and b) p-$MOF_{HKUST\text{-}1(90)}$-ink, after immersing in water for 1 day.

The photocurable MOF ink can be readily utilized for various processing techniques such as spray coating, pen writing, stencil printing, and moulding. As shown in Figure 3.8a, various types of MOFs such as HKUST-1, MIL-101 (Cr), ZIF-67, ZIF-8, and MOF-74 (Ni) can successfully be formulated as $MOF_{(70)}$-inks (MOF/PFPE = 70/30 wt%) regardless of the MOF types, and spray-coated to form thin films on glass plates (1.8 cm × 1.8 cm) without any visible defect. In addition, a pen (3 mm tip size) filled with s-$MOF_{HKUST\text{-}1(70)}$-ink could be used to write on any type of substrate including paper, warped glass vial, rough cloth, and flexible polyethylene film (Figure 3.8b). After UV curing, the p-$MOF_{HKUST\text{-}1(70)}$-ink adhered onto the substrates firmly due to the viscous nature of the PFPE binder, which is not possible with the MOF alone (Figure 3.9). Figure 3c shows the stencil-printed $MOF_{HKUST\text{-}1(70)}$-ink on the biocompatible PDMS film (7 cm × 6 cm), demonstrating that the formulated MOF inks can be easily positioned and patterned over a wide area on desired substrate with a resolution of 200 μm. The SEM image of the stencil-printed p-$MOF_{HKUST\text{-}1(70)}$-ink clearly indicates that each dot adheres well to the PDMS film surface. Furthermore, highly loaded MOF inks ($MOF_{HKUST\text{-}1(30)}$-ink, for example) can be utilized to cast 3D structures via moulding (Figure 3.10). The cross-sectional SEM image of the 3D hemisphere reveals that the MOF crystals are well embedded within the polymer matrix (Figure 3.11). These results demonstrate versatile processability of our MOF ink system in terms of applicability to various MOF types, different substrates, and various types of structure formation with good adhesion. Furthermore, the processability does not interfere with the intrinsic properties of the constituents. These attributes together with the hydrolytic stability would open many opportunities otherwise unattainable.

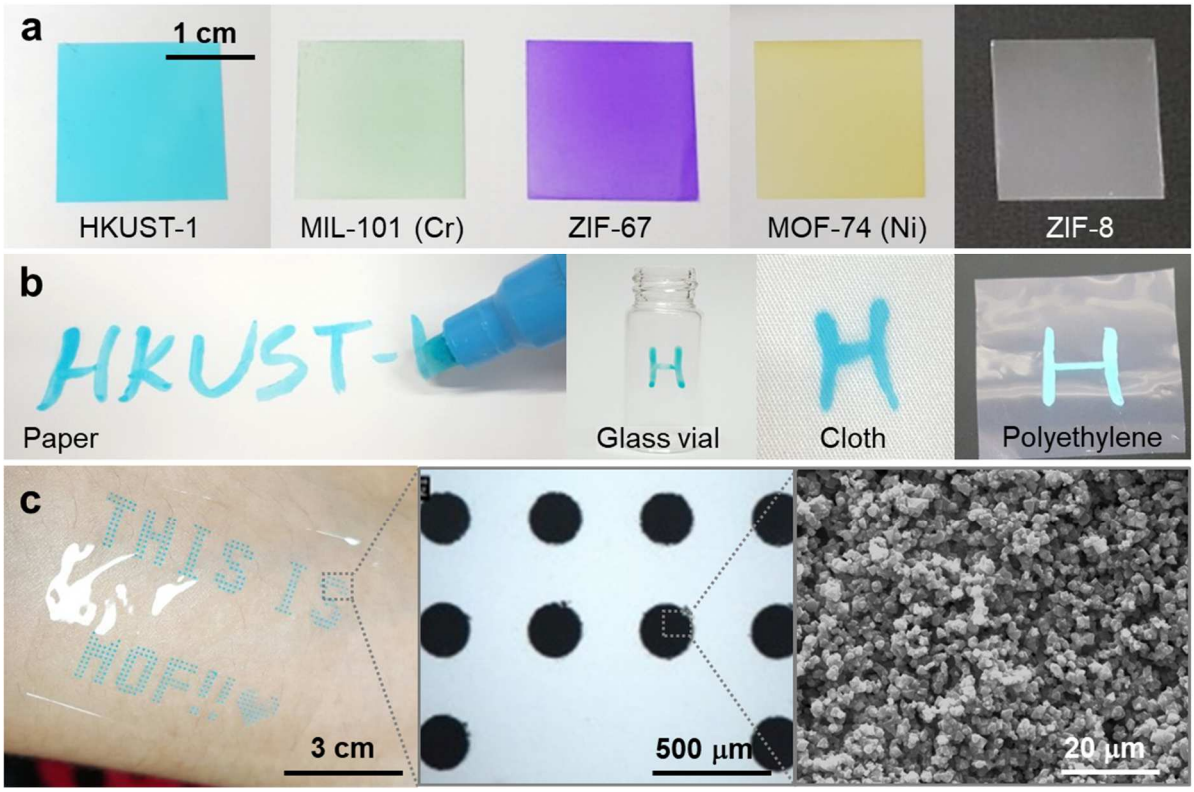

Figure 3.8 Processability of various MOF inks containing MIL-101 (Cr), ZIF-67, ZIF-8, and MOF-74 (Ni). (a) Photographs of five types of p-MOF(70)-ink thin films fabricated on glass plates by spray coating technique. (b) Photographs of writings using a pen filled with p-MOFHKUST-1(70)-ink on various substrates (paper, glass vial, cloth, and polyethylene film). (c) Photograph (left), optical microscopy image (middle), and SEM image (right) of p-MOFHKUST-1(70)-ink dot array (200 μm diameter) patterned on a PDMS thin film by stencil printing technique.

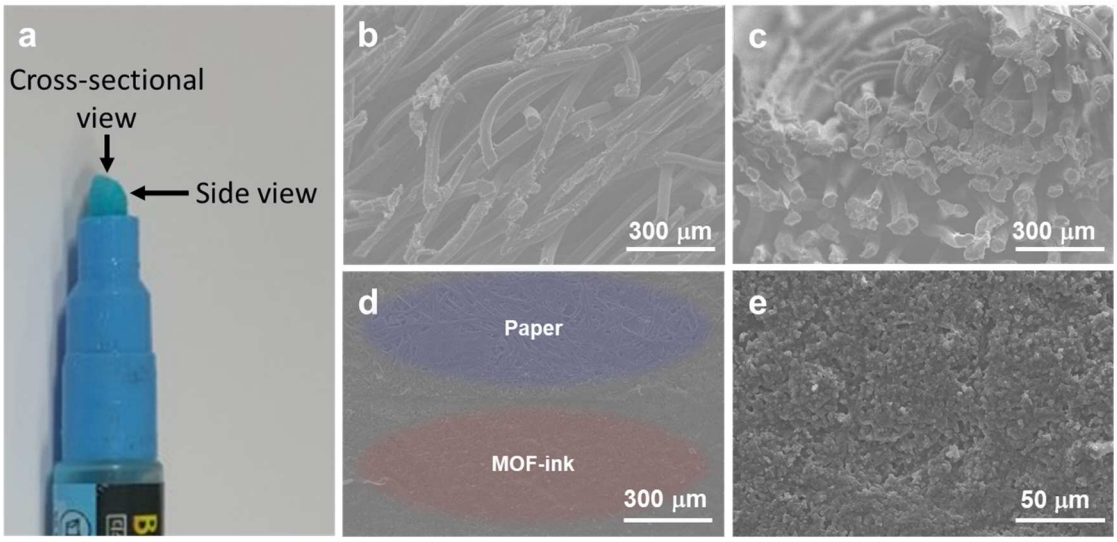

Figure 3.9 a) Photographic image of fiber-based tip of board marker. SEM images of fiber-based tip for b) side view and c) cross-sectional view. s-MOF-ink can be processed on the substrate along the pen movement by wetting the fiber-based tip of the pen. SEM images of d) p-$MOF_{HKUST\text{-}1(70)}$-ink line written on the paper, and e) enlargement of p-$MOF_{HKUST\text{-}1(70)}$-ink line.

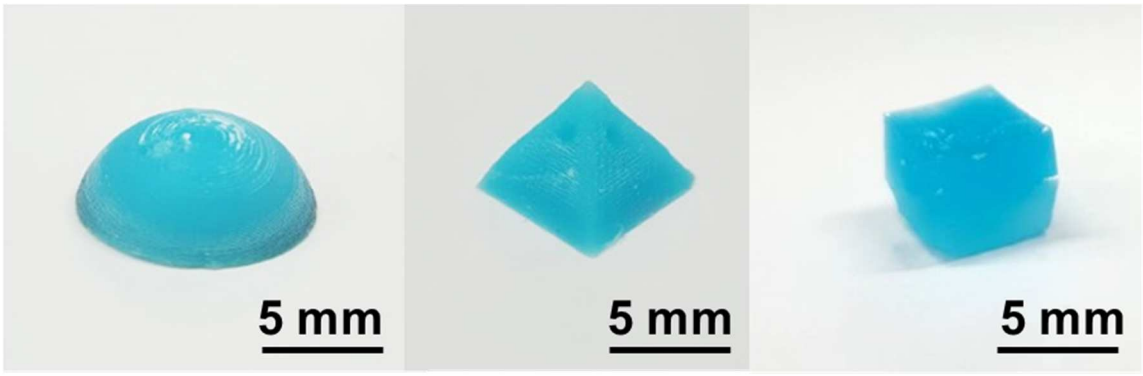

Figure 3.10 Photographic images of 3-dimensional shaped p-$MOF_{HKUST\text{-}1(30)}$-ink *via* molding process; hemisphere, square pyramid, and cuboid.

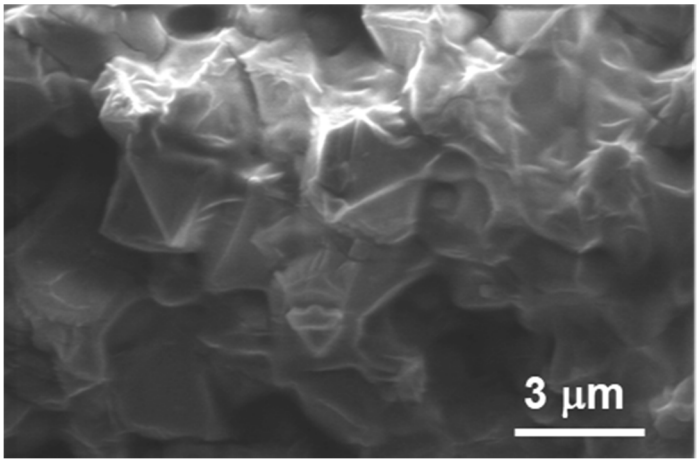

Figure 3.11 SEM image of the p-$MOF_{HKUST\text{-}1(30)}$-ink.

MOFs have attracted considerable scientific attention as a promising material for molecular sensors owing to their structural diversity and tailorable functionality.[14,15] However, difficult device fabrication and hydrolytic (i.e., water) instability limited wide use of MOFs as practical sensors. Inspired by the results that the formulated MOF-PFPE composite ink cooperatively improved the hydrolytic stability and the processability in various forms, we used our MOF ink to fabricate miniaturized portable sensors that can detect volatile organic compounds (VOCs) in water.

A functional but extremely moisture-sensitive MOF, $Zn_2(bdc)_2(dpNDI)$ (bdc = 1,4-benzenedicarboxylate; dpNDI = *N*,*N'*-di(4-pyridyl)-1,4,5,8-naphthalenediimide) (designated as MOF_{chemo}) was selected for demonstrating a chemosensor. Upon excitation of the MOF at 365 nm, the photoluminescent (PL) peak of the MOF at 430 nm changes to 445 nm for benzene when it is present in the water, 475 nm for toluene, 504 nm for *p*-xylene, and 528 nm for styrene, as shown in Figure 3.12. A chameleon-shaped portable underwater sensor was fabricated by spray-coating the chameleon feature (7 cm x 4 cm x 2 cm), which was constructed via 3D printing with polypropylene (Figure 3.13a), with the as-prepared s-$MOF_{chemo(70)}$-ink. After 10 min of UV irradiation (365 nm), the p-$MOF_{chemo(70)}$-ink adhered well on the surface of the 3D irregular structure, as evidenced by the SEM and optical images (Figure 3.13a, Figures 3.14 and 3.15).

When the chameleon sensor was separately soaked in respective VOC solvent, the corresponding emission for each VOC was immediately observed over the entire surface under handheld UV lamp (Figure 3.13b). Identical change in the emission by the p-$MOF_{chemo(70)}$-ink powder (Figure 3.13c) as well as the pristine MOF_{chemo} powder (Figure 3.12) indicates that the p-$MOF_{chemo(70)}$-ink retains its intrinsic sensing properties. Moreover, the water-repellent PFPE-coated $MOF_{chemo(70)}$ shows significant improvement in hydrolytic stability, retaining its structure when immersed in water for 2 min (Figures

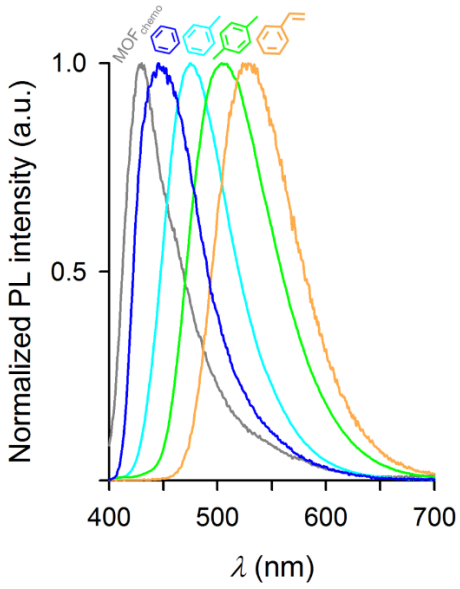

Figure 3.12 No normalized luminescent spectra of pristine MOF_{chemo} immersed in pure VOC solvent upon excitation at 365 nm. The emission changes upon detection of VOCs from 430 nm to 445 nm for benzene, 475 nm for toluene, 504 nm for *p*-xylene, and 528 nm for styrene, respectively.

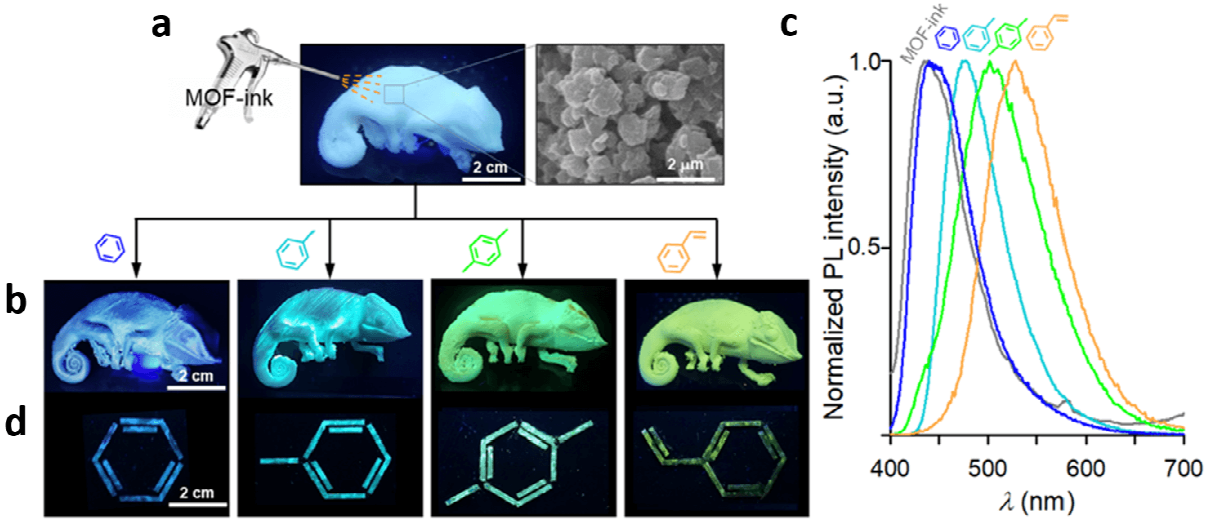

Figure 3.13 VOCs sensing with $MOF_{chemo(70)}$-ink containing $Zn_2(bdc)_2(dpNDI)$. (a) Photograph of 3D printed chameleon feature spray-coated with MOF-fluoropolymer ink as a VOC sensor under UV irradiation at 365 nm and SEM image of the chameleon surface. Scale bar: 2 μm. (b) Photographs of chameleon sensors under UV irradiation at 365 nm and (c) Normalized photoluminescence (PL) spectra of p-$MOF_{chemo(70)}$-ink obtained after immersion in neat VOC solvent upon excitation at 365 nm. The emission peak changes upon detection of VOCs from 434 nm to 440 nm for benzene, 478 nm for toluene, 502 nm for *p*-xylene, and 528 nm for styrene, respectively. (d) Photographs of VOC molecule-patterned sensors on glass slides after immersion in aqueous VOC (0.2 vol%) solution under UV irradiation at 365 nm.

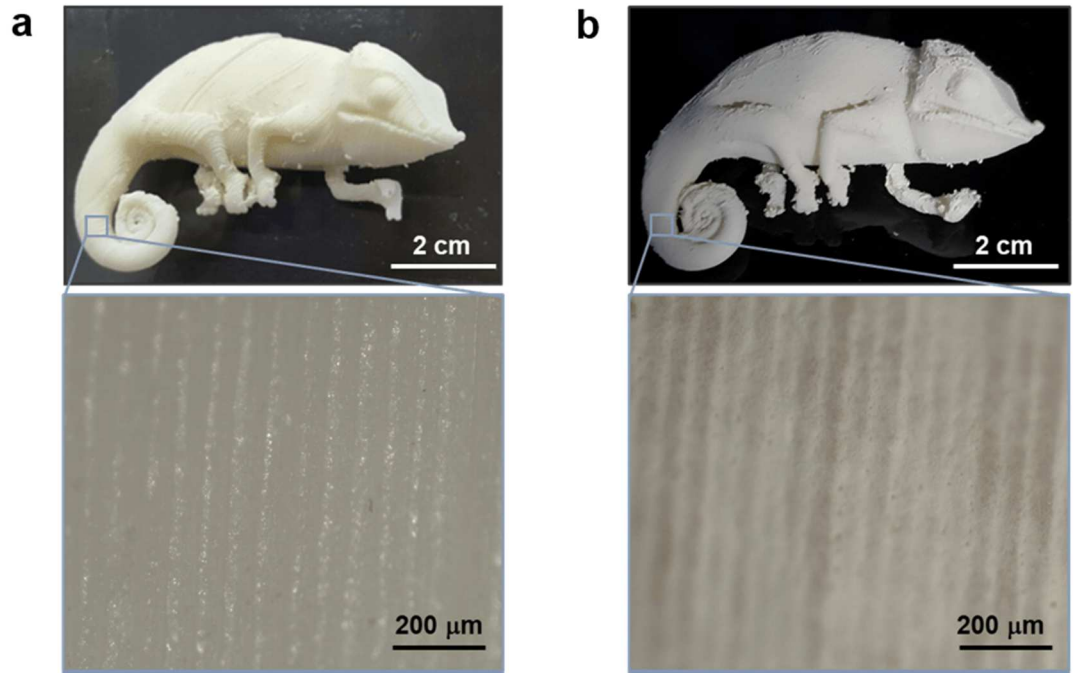

Figure 3.14 Optical images of (a) bare chameleon surface and (b) p-MOF$_{chemo(70)}$-ink coated chameleon surface.

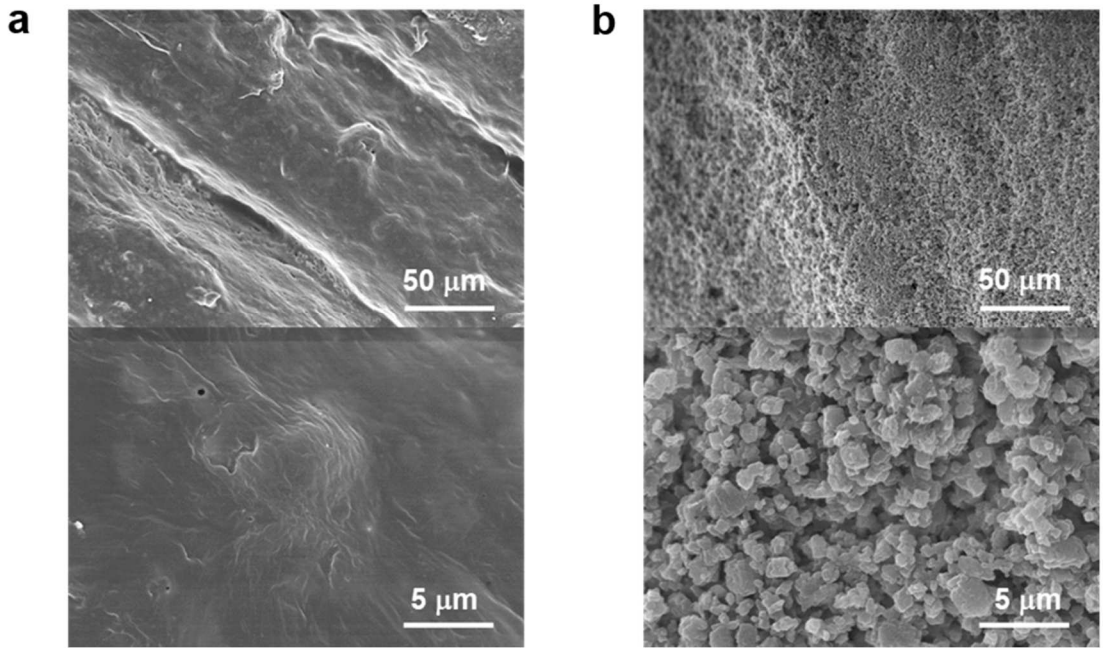

Figure 3.15 SEM images of (a) bare chameleon surface and (b) p-MOF$_{chemo(70)}$-ink attached chameleon surface.

3.16 and 3.17), while the bare MOF_{chemo} instantly lost its crystallinity and luminance in water. Thus, when the VOC molecule patterns on glass slides, which were obtained by stencil printing using the MOF ink as aforementioned, were immersed in 0.2 vol% aqueous VOC solution, the sensor exhibited the same luminescence colour change as that observed for pure VOC molecules for over 5 min (Figure 3.13d and Figures 3.18-3.21). To the best of our knowledge, this experiment is the first attempt to demonstrate the use of a hydrolytically unstable MOF as a VOC sensor to detect various organic compounds in a water-dominant environment, in contrast to previous attempts that involved sensing only under non-hydrolytic conditions to avoid its hydrolytic decomposition.[38-,44-45]

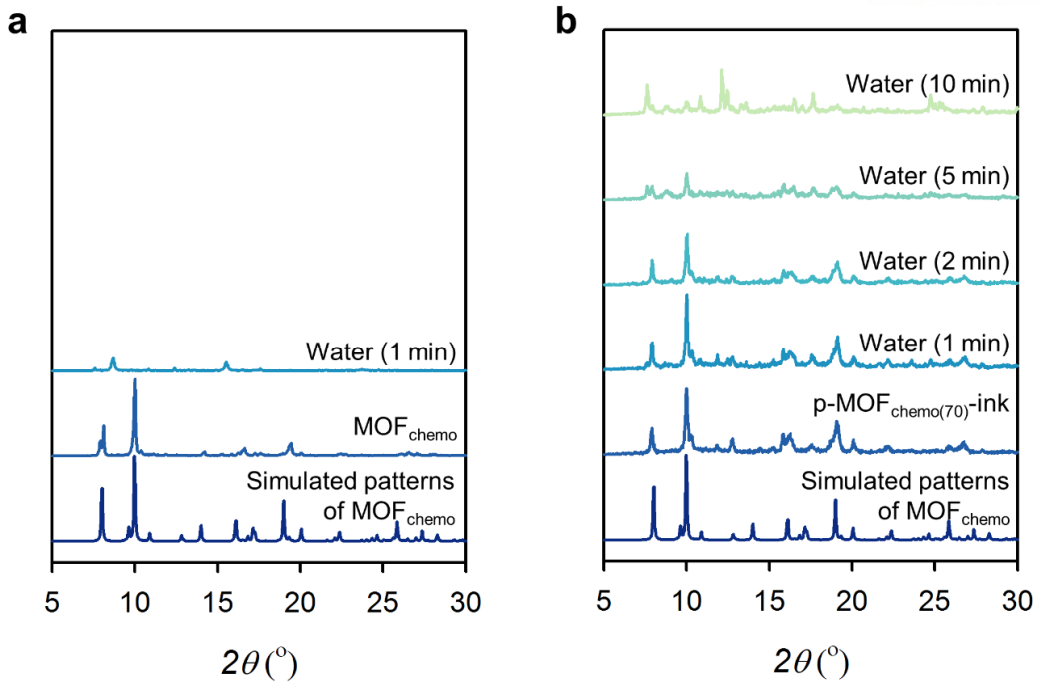

Figure 3.16 PXRD patterns of (a) pristine MOF_{chemo} and (b) p-$MOF_{chemo(70)}$-ink, compared with the simulated pattern from single crystal X-ray diffraction data of MOF_{chemo}[38].

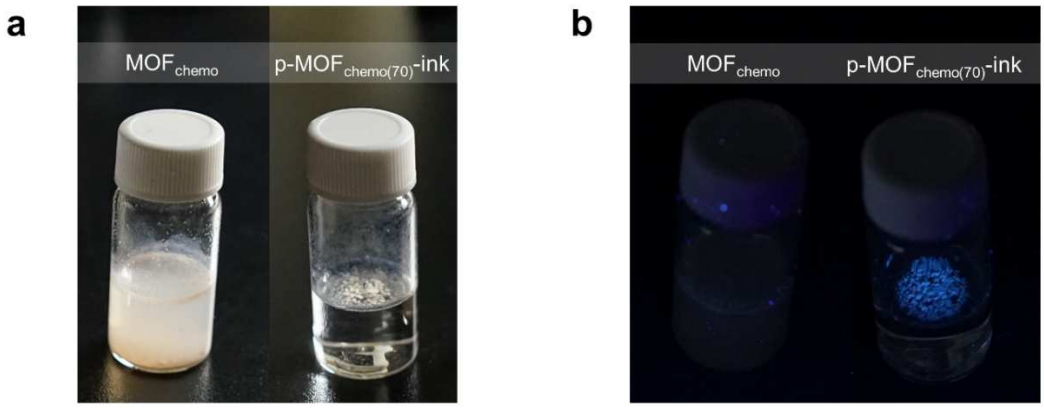

Figure 3.17 Photographs of pristine MOF_{chemo} and p-$MOF_{chemo(70)}$-ink taken after soaking in water for 1 min under (a) room light and (b) UV irradiation at 365 nm.

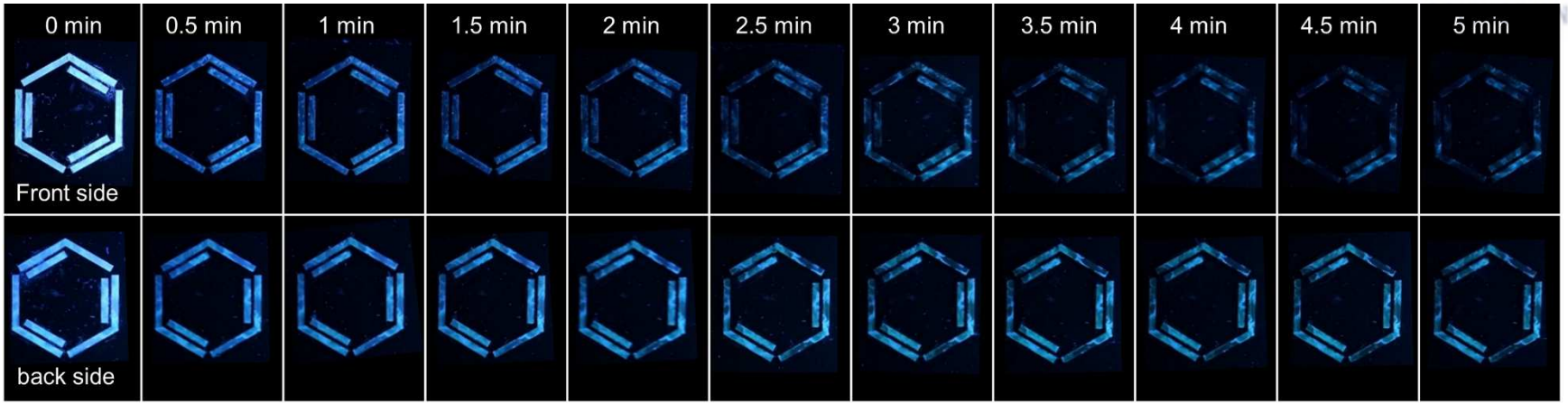

Figure 3.18 A series of photographic images of a VOC-molecule patterned sensor on a slide glass under excitation at 365 nm, after soaking for different times in the emulsion of 0.2 vol% of benzene in water.

The back side of the slide glass (images in the 2nd row) shows a strong emission in a longer lasting manner than the front side (images in the 1st row) due to longer diffusion time of hydrophilic water molecules along hydrophobic PFPE permeation path from the front interface between the MOF-ink and emulsion, while the hydrophobic VOC molecules can diffuse faster.

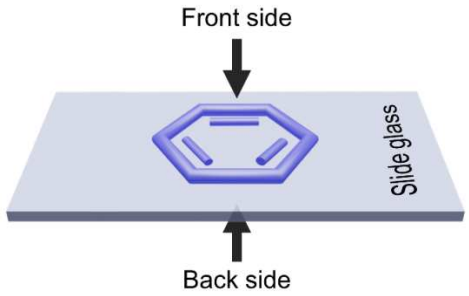

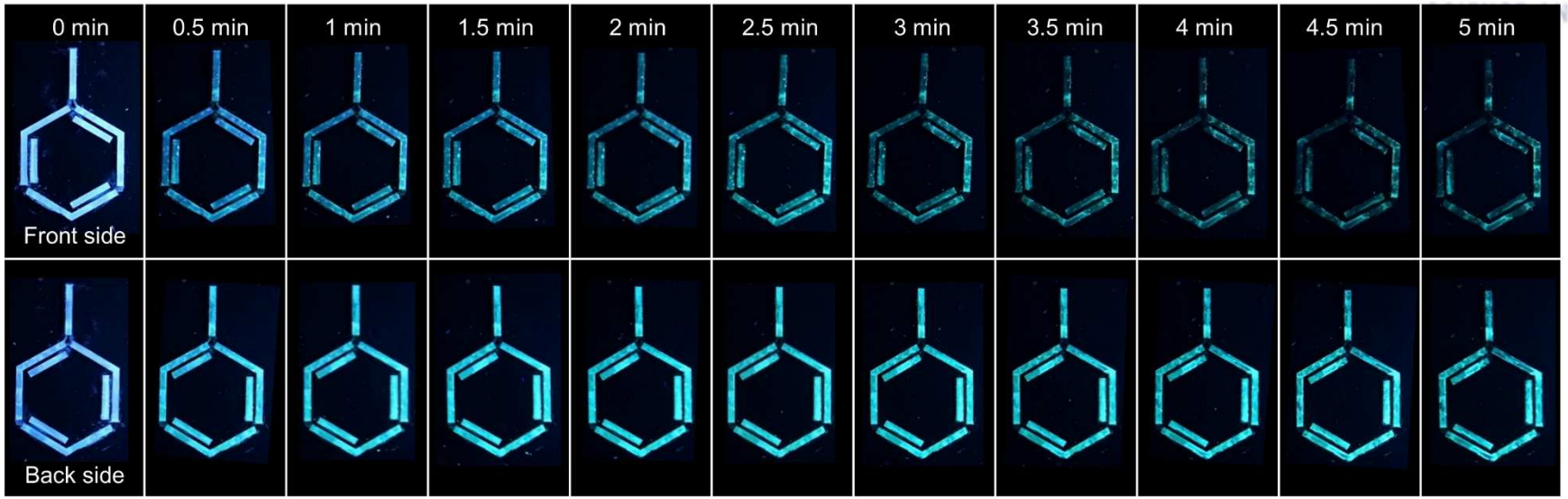

Figure 3.19 A series of photographic images a VOC-molecule patterned sensor on a slide glass under excitation at 365 nm, after soaking in the emulsion of 0.2 vol% of toluene in water.

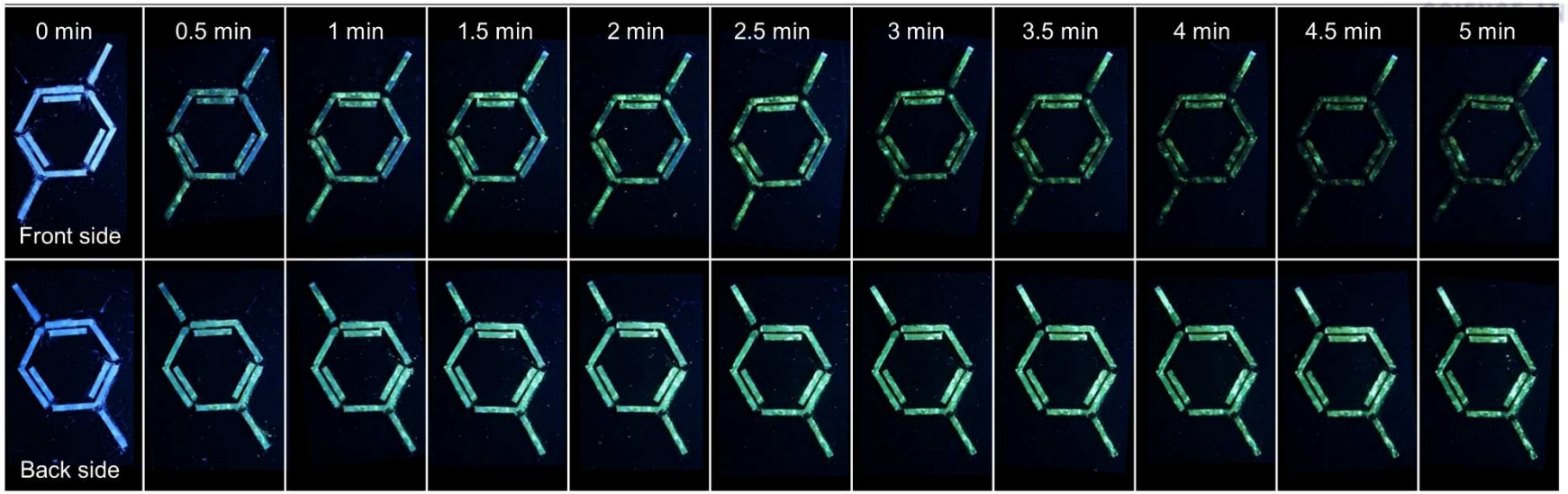

Figure 3.20 A series of photographic images of a VOC-molecule patterned sensor on a slide glass under excitation at 365 nm, after soaking in the emulsion of 0.2 vol% of *p*-xylene in water.

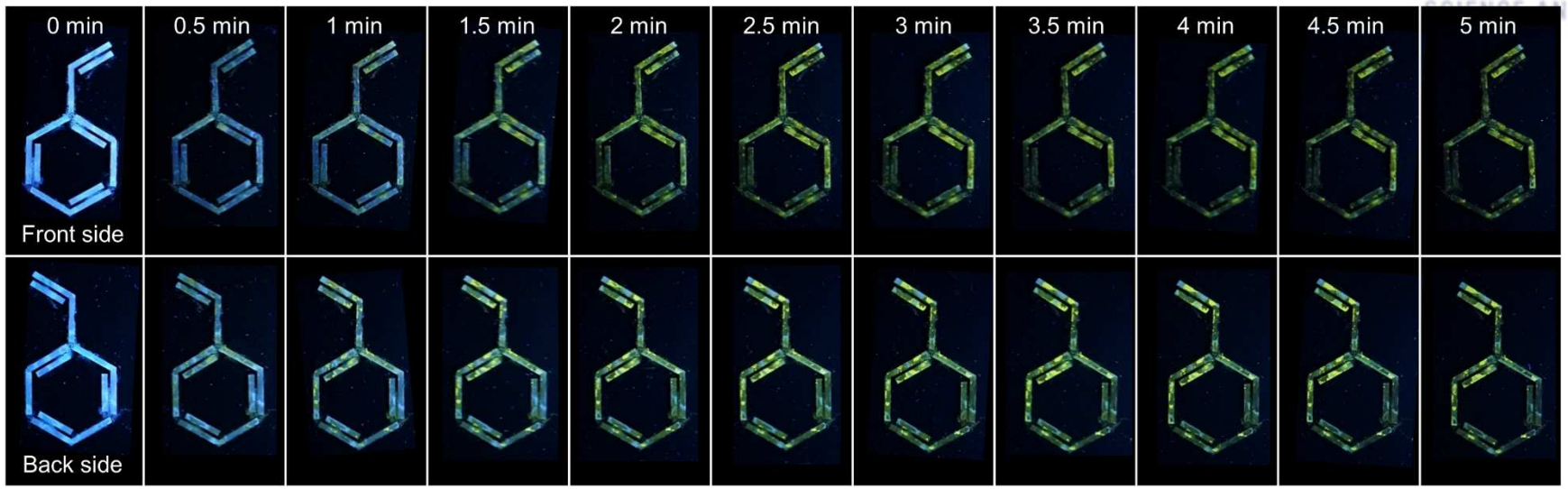

Figure 3.21 A series of photographic images of a VOC-molecule patterned sensor on a slide glass under excitation at 365 nm, after soaking in the emulsion of 0.2 vol% of styrene in water.

Visualization of the temperature of targeted regions of a material surface is critical in aeronautical and environmental engineering. For the purpose, the traditional thermometers are inadequate because they are for single-point detection. It is thus natural that temperature-sensitive luminescent MOFs gained intense attention for heat visualization.[46,47] The actual application of MOFs for the visualization, however, is still in its nascent stage due to the fragile and unprocessable nature of MOF crystals. To address this issue, we applied the MOF ink strategy to create a thermo-sensitive and temperature-visualizable ink, which is easily applicable in various forms. A functional MOF, $Tb_{0.99}Eu_{0.01}(hfa)_3(dpbp)$ (hfa = hexafluoroacetylacetonato; dpbp = 4,4'-bis(diphenylphosphoryl)biphenyl) (designated as MOF_{thermo}) was selected because it can show temperature change through a dynamic shift in luminescent colour from green to red, which has been demonstrated only in powder form.[41,48]

To achieve good processibility and secure its stability, we prepared the $MOF_{thermo(10)}$-ink containing up to 90 wt% PFPE, whose XRPD profile indicates that the framework structure was well retained even after photocuring (Figure 3.22). The processibility of s-$MOF_{thermo(10)}$-ink was examined by coating on highly curved surfaces of a stirring bar and a glass rod, stencilling in desired shapes, and moulding into 3D structures (Figure 3.23). As shown in the SEM and photographic images for the stirring bar (Figures 3.24 and 3.25), the MOF crystals are well embedded in the polymer matrix and the p-$MOF_{thermo(10)}$-ink is well coated on the stir bar which can withstand vigorous stirring for 3 hours. Since high content of

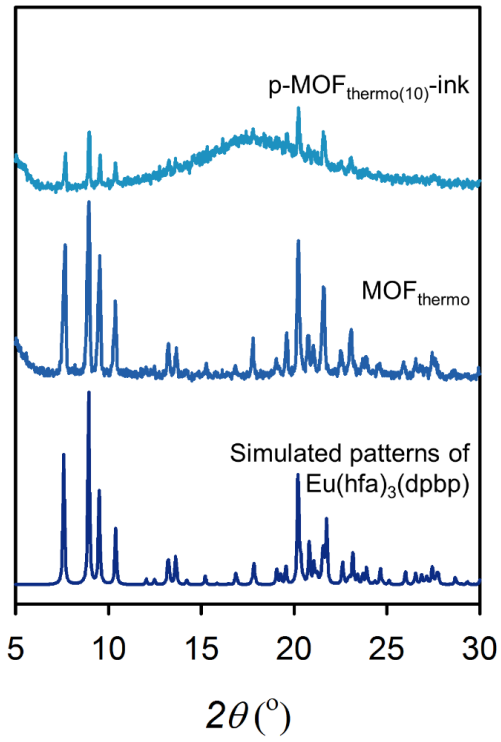

Figure 3.22 XRPD patterns of pristine MOF_{thermo} and p-$MOF_{thermos(10)}$-ink, compared with the simulated pattern from single crystal X-ray diffraction data of $Eu(hfa)_3(dpbp)$[7].

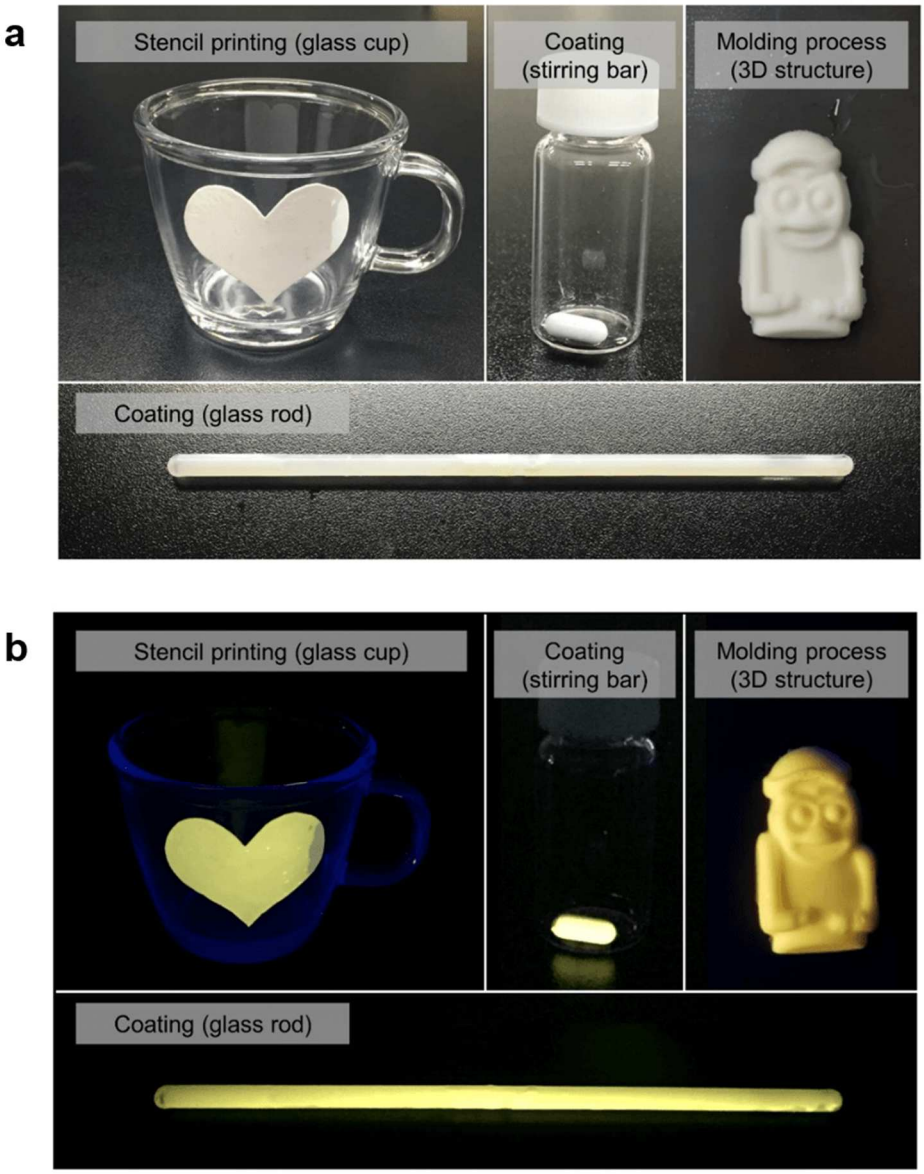

Figure 3.23 Photographic images of various forms of p-$MOF_{thermo(10)}$-ink under (a) room light and (b) excitation at 365 nm.

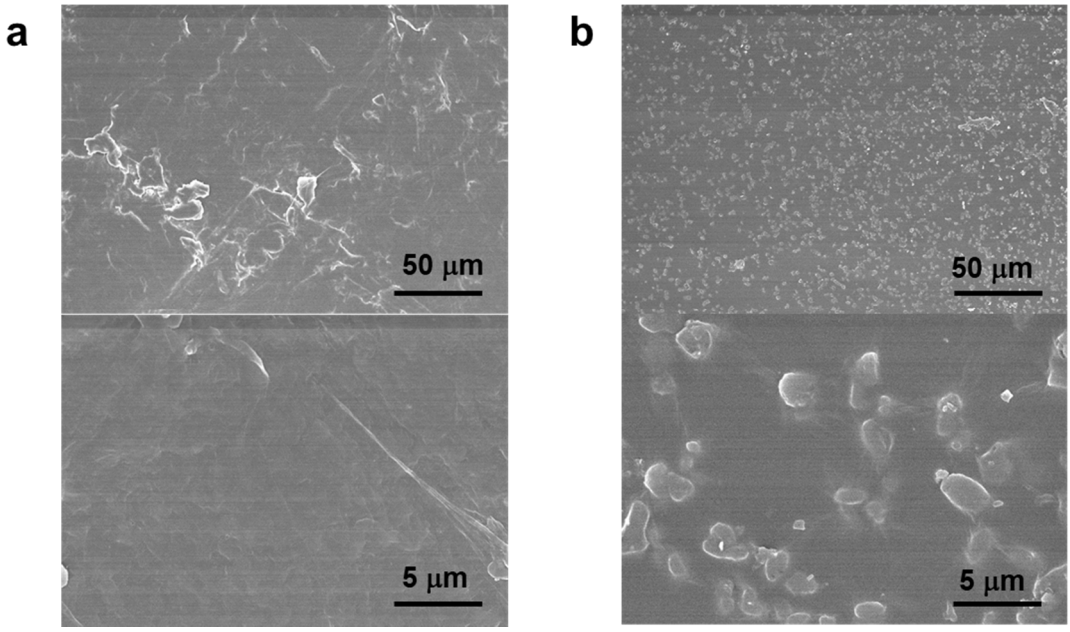

Figure 3.24 SEM images of (a) bare stirring bar and (b) p-MOF$_{thermo(10)}$-ink on the stirring bar.

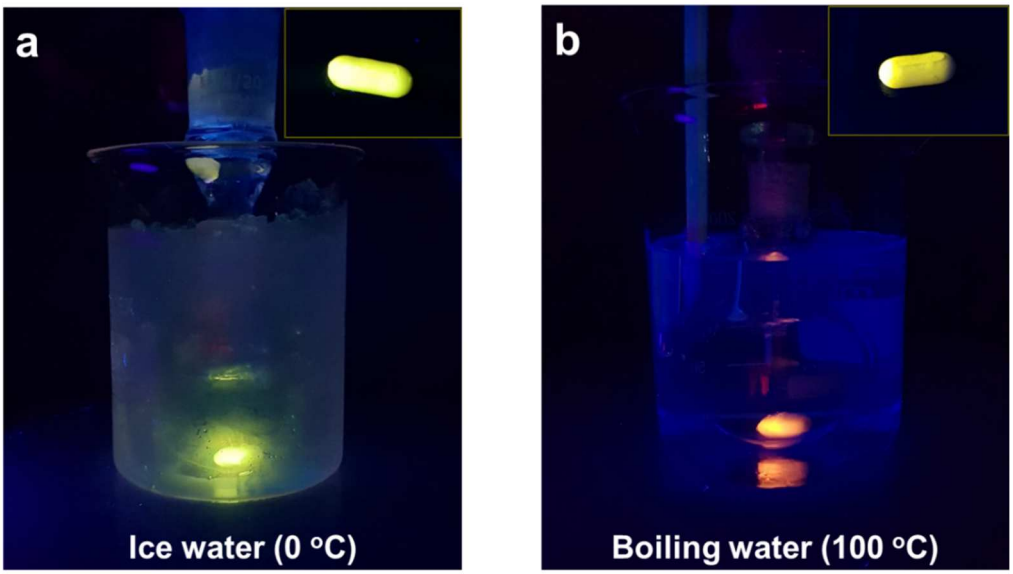

Figure 3.25 Photographic images of the p-MOF$_{thermo(10)}$-ink coated stirring bar stirred in (a) ice water (0 ^{o}C) and (b) boiling water (100 ^{o}C) under excitation at 365 nm. The inserted images of p-MOF$_{thermo(10)}$-ink coated stirring bar were taken after stirring for 3 hr in each bath.

the chemical-resistant PFPE polymer matrix minimized the influence of external environment by nearly completely shielding the molecular access to the MOF, the luminescence of the ink was sustained safely even after immersing in a variety of organic solvents, strong acids, and bases for 5 min (Figure 3.26a and Figure 3.27). In contrast, the MOF powder itself drastically lost its luminescent nature under the same condition. Moreover, a rapid change in luminescence colour of the ink depending on the temperature of water poured into the cup reveals the efficient heat transfer to the MOF_{thermo} crystals embedded in the PFPE matrix (Figure 3.28).

To further demonstrate the visualization capability, a cooling bath (−20 °C) and an oil bath (120 °C) were placed at each ends of a p-$MOF_{thermo(10)}$-ink-coated glass rod. The temperature gradient along the surface is clearly visualized by the gradual colour change from green to red along the rod under UV irradiation at 365 nm (Figure 3.26b). The experiment is perhaps the first demonstration of a thermo-sensitive luminescence MOF ink for visualization of the temperature profile of an entire surface in visible colour. This approach should be useful for fast heat sensing and mapping as for safety warning of overheated electronic devices such as overloaded battery.

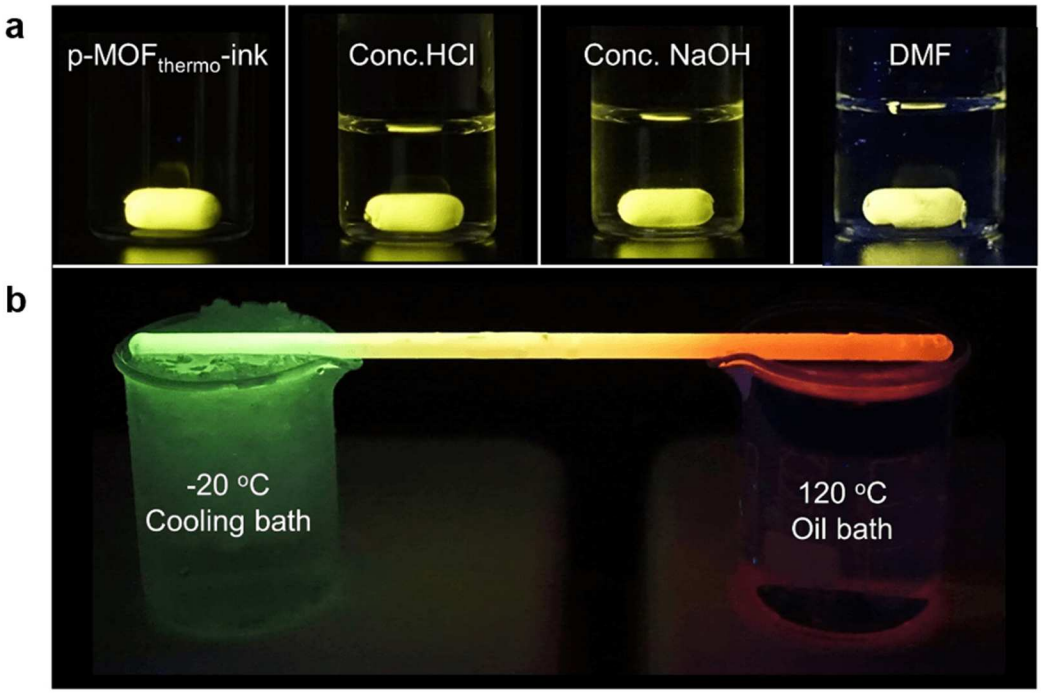

Figure 3.26 Temperature sensing with a p-$MOF_{thermo(10)}$-ink containing $Tb_{0.99}Eu_{0.01}(hfa)_3(dpbp)$. (a) Photographs of a stirring bar coated with p-$MOF_{thermo(10)}$-ink that was placed in concentrated HCl, concentrated NaOH, and DMF for 5 min, respectively, under UV irradiation at 365 nm. (b) Photograph of temperature-visualizable ink-coated glass rod, the ends of which are placed on a cooling bath (−20 °C) and an oil bath (120 °C) under UV irradiation at 365 nm.

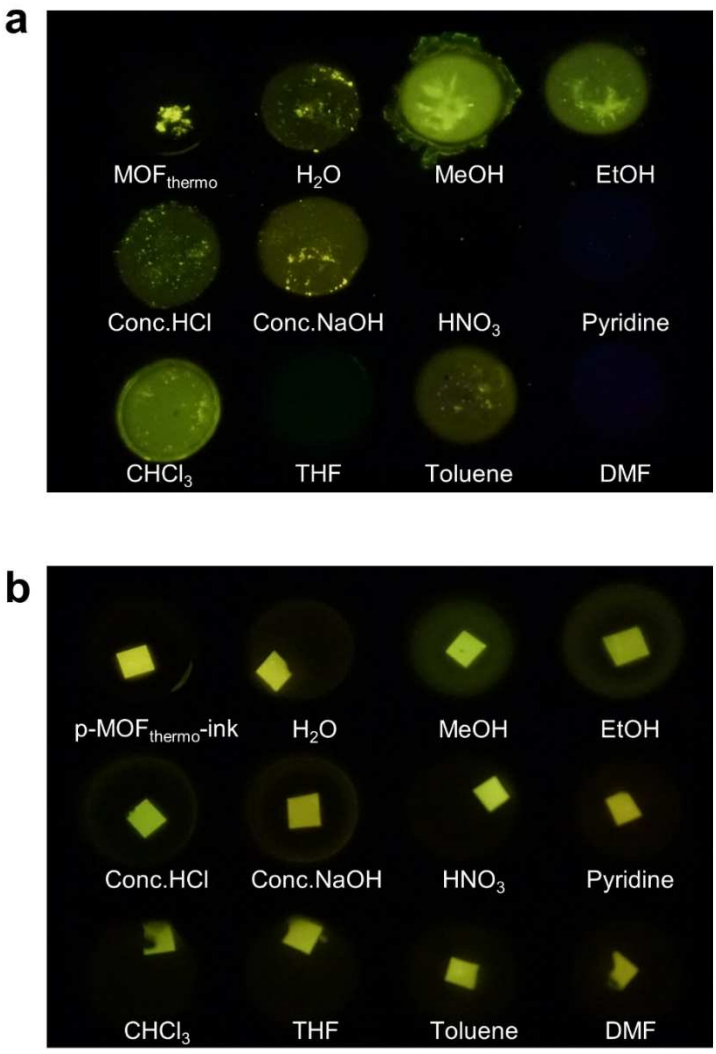

Figure 3.27 Photographic images of (a) pristine MOF_{thermo} powder and (b) square-shaped slices of p-MOF_{thermo}-ink were immersed in 11 different solvents for 5 min under excitation at 365 nm. The free standing p-$MOF_{thermo(10)}$-ink slices were obtained by cutting and detaching from the coated film on a slide glass.

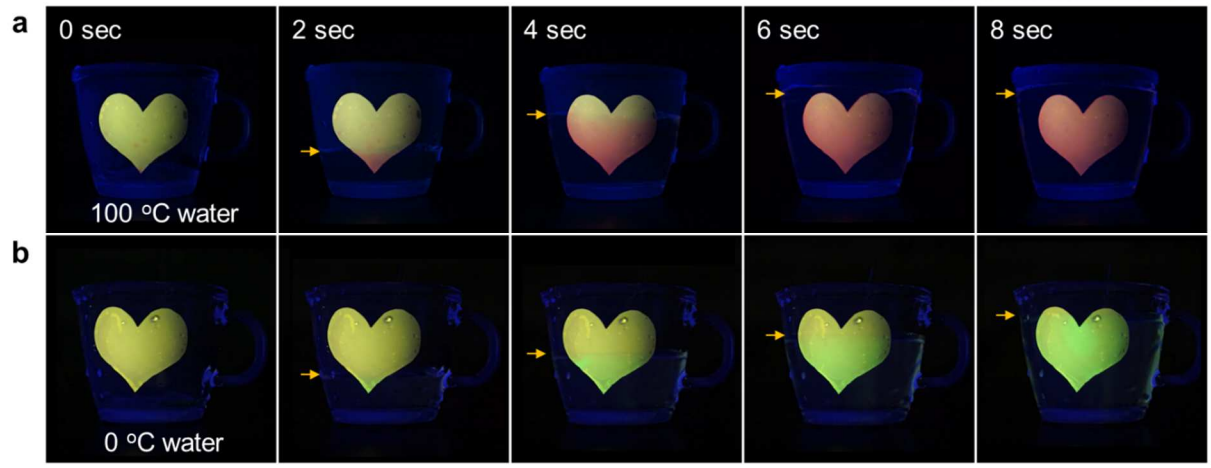

Figure 3.28 Photographic images of rapid change in luminescence color of the p-MOF$_{thermo(10)}$-ink depending on the temperature of water poured into the cup; (a) 100 °C water and (b) 0 °C water. Yellow arrow indicates the surface of water.

3.4 Conclusion

In conclusion, we have advanced a new class of MOF-fluoropolymer composite inks with excellent processability and chemical resistance, including hydrolytic stability, to help resolve the difficulties in utilizing functional MOFs as industrially viable products. This new class of MOF-polymer composite inks has a high loading of MOFs dispersed in a versatile polymer of PFPE that acts as an efficient binder and provides a robust shielding matrix against moisture. Various versatile MOFs (HKUST-1, MIL-101 (Cr), ZIF-67, ZIF-8, and MOF-74 (Ni)) can simply be formulated as an ink with the water repellent and photocurable PFPE in a wide range of mixing ratios. The UV curable MOF inks are readily adaptable to a variety of processing techniques such as spray coating, pen writing, stencil printing, and 3D moulding without complex optimization steps, and are applicable to any substrates and shapes. Furthermore, the excellence of the MOF inks containing $Zn_2(bdc)_2(dpNDI)$ and $Tb_{0.99}Eu_{0.01}(hfa)_3(dpbp)$ crystals was successfully demonstrated as a portable chemical sensor for 0.2 vol% VOC detection in water, and as a thermal sensor for real time visualization of temperature distribution of objects of interest, respectively. We believe that this simple strategy of the MOF-PFPE formulations will open up new avenues to innumerable MOFs, which have remained dormant so far, for a wide variety of novel applications.

3.5 References

1. Li, H.; Eddaoudi, M.; O'Keffe, M.; Yaghi, O. M. *Nature* **1999**, *402*, 276.
2. Lu, W.; Wei, Z.; Gu, Z.; Liu, T.; Park, J.;Park, J.; Tian, J.; Zhang, M.; Zhang, Q.; Gentle, T., III; Bosch, M.; Zhou, H.-C. *Chem. Soc. Rev.* **2014**, *43*,5561.
3. Falcaro, P.; Ricco, R.; Doherty, C. M.; Liang, K.; Hill, A. J.; Styles, M. J. *Chem. Soc. Rev.* **2014**,*43*, 5513.
4. Rowsell, J. L. C.; Yaghi, O. M. *Microporous and Mesoporous Materials* **2004**, *73*, 3.
5. Furukawa, H.; Cordova, K. E.; O'Keeffe, M.; Yaghi, O. M. *Science* **2013**, *341*, 1230444.
6. Yaghi, O. M.; O'Keeffe, M.; Ockwig, N. W.; Chae, H. K.; Eddaoudi, M.; Kim, J. *Nature* **2003**, *423*, 705.
7. Zhao, D.; Timmons, D. J.; Yuan, D.; Zhou, H.-C. *Acc. Chem. Res.* **2001**, *44*, 123-133.
8. Suh, M. P.; Park, H. J.; Prasad, T. K.; Lim, D.-W. *Chem. Rev.* **2012**, *112*, 782.
9. He, Y.; Zhou, W.; Qian, G.; Chen, B. *Chem. Soc. Rev.* **2014**, *43*, 5657.
10. Trickett, C. A.; Helal, A.; Al-Maythalony. B. A.; Yamani, Z. H.; Cordova, K. E.; Yaghi, O. M. *Nat. Rev. Mater.* **2017**, *2*, 17045.
11. Denny, M. S.; Moreton, J. C.; Benz, L.; Cohen, S. M. *Nat. Rev. Mater.* **2016**, *1*, 16078.
12. Huang, Y.-B.; Liang, J.; Wang, X.-S.; Cao, R. *Chem. Soc. Rev.* **2017**, *46*, 126.
13. Wu, M.-X.; Yang, Y.-W. *Adv. Mater.* **2017**, *29*, 1606134.
14. Kreno, L. E.; Leong, K.; Farha, O. K.; Allendorf, M.; Van Duyne, R. P.; Hupp, J. T. *Chem. Rev.* **2012**, *112*, 1105.
15. Yi, F.-Y.; Chen, D.; Wu, M.-K.; Han, L.; Jiang, H.-L. *ChemPlusChem* **2016**, *81*, 675.
16. Decoste, J. B.; Peterson, G. W.; Smith M. W.; Strone, C. A.; Willis, C. R. *J. Am. Chem. Soc.* **2012**, *134*, 1486.
17. Carné-Sánchez, A.; Stylianou, K. C.; Carbonell, C.; Naderi, M.; Imaz, I.; Maspoch, D. *Adv. Mater.* **2015**, *27*, 869.

18. Yuan, S.; Feng, L.; Wang, K.; Pang, J.; Bosch, M.; Lollar, C.; Sun, Y.; Qin, J.; Yang, X.; Zhang, P.; Wang, Q.; Zou, L.; Zhang, Y.; Zhang, L.; Fang, Y.; Li, J.; Zhou, H. –C. *Adv. Mater*. **2018**, 1704303.

19. Burtch, N. C.; Heinen, J.; Bennett, T. D.; Dubbeldam, D.; Allendorf, M. D. *Adv. Mater*. **2017**, 1704124.

20. Howarth, A. J.; Liu, Y., Li, Peng.; Wang, T. C.; Hupp, J. T. *Nat. Rev. Mater*. **2016**, *1*, 15018.

21. Low, J. J.; Benin, A. I.; Jakubczak, P.; Abrahamian, J. F.; Faheem, S. A.; Willis, R. R. *J. Am. Chem. Soc.* **2009**, *131*, 15834.

22. Ameloot, R.; Gobechiya, E.; Uji-i, H.; Martens, J. A.; Hofkens, J.; Alaerts, L.; Sels, B. F.; De Vos, D. E. *Adv. Mater*. **2010**, *22*, 2685.

23. Arslan, H. K.; Shekhah, O.; Wohlgemuth, J.; Franzreb, M.; Fischer, R. A.; Wöll, C. *Adv. Funct. Mater*. **2011**, *21*, 4228.

24. Zhuang, J.-L.; Ar, D.; Yu, X.-J.; Liu, J.-X.; Terfort, A. *Adv. Mater*. **2013**, *25*, 4631.

25. Rodenas, T.; Luz, I.; Prieto, G.; Seoane, B.; Miro, H.; Corma, A.; Kapteijn, F.; Llabrés i Xamena, F. X.;Gascon, J. *Nat. Mater*. **2015**, *14*, 48.

26. DeCoste, J. B.; Denny, M. S., Jr.; Peterson, G. W.; Mahle, J. J.; Cohen, S. M. *Chem. Sci.* **2016**, 7, 2711.

27. Bachman, J. E.; Smith, Z. P.; Li, T.; Xu, T.; Long, J. R. *Nat. Mater*. **2016**, *15*, 845.

28. Bae, T. H.; Lee, J. S.; Qiu, W.; Koros, W. J.; Jones, C. W.; Nair, S. *Angew. Chem., Int. Ed.* **2010**, *49*, 9863-9866; Angew. Chem. **2010**, *122*, 10059.

29. Denny, M. S.; Cohen, S. M. *Angew. Chem., Int. Ed.* **2015**, *54*, 9029.

30. Xiang, L.; Sheng, L.; Wang, C.; Zhang, L.; Pan, Y.; Li, Y. *Adv. Mater*. **2017**, *29*, 1606999.

31. Xie, K.; Fu, Q; Webley, P. A.; Qiao, G. G. *Angew. Chem., Int. Ed.* **2018**, *57*, 8597.

32. Liu, G.; Chernikova, V.; Liu, Y.; Zhang, K.; Belmabkhout, Y.; Shekhah, O.; Zhang, C.; Yi, S.; Eddaoudi, M.; Koros, W. S. *Nat. Mater*. **2018**, *17*, 283.

33. Kim, J.-O.; Kim, H.; Ko, D.-H.; Min, K.-I.; Im, D. J.; Park, S.-Y.; Kim, D.-P. *Lab Chip* **2014**, *14*, 4270.

34. Rolland, J. P.; Van Dam, R. M.; Schorzman, D. A.; Quake, S. R.; DeSimone, J. M. *J. Am. Chem. Soc.* **2004**, *126*, 2322.

35. Zhuang, J.-L.; Ceglarek, D.; Pethuraj, S.; Terfort, A.; *Adv. Funct. Mater.* **2011**, *21*, 1442.

36. Avci, C.; Ariñez-Soriano, J.; Carné-ánchez, A.; Guillerm, V.; Carbonell, C.; Imaz, I.; Maspoch, D. *Angew. Chem., Int. Ed.* **2015**,*54*, 14417.

37. Kim, J. Y.; Balderas-Xicohténcatl, R.; Zhang, L.; Kang, S.G.; Hirscher, M.; Oh, H.; Moon, H.R. *J. Am. Chem. Soc*. **2017**, *139*, 15135.

38. Takashima, Y.; Martínez, V. M.; Furukawa, S.; Kondo, M.; Shimomura, S.; Uehara, H.; Nakahama, M.; Sugimoto, K.; Kitagawa, S. *Nat. Commun.* **2011**, *2*, 168.

39. Buckles, R.E.; Wheeler, N. G. *Org. Synth.* **1951**, *31*, 29.

40. Miyata, K.; Ohba, T.; Kobayashi, A.; Kato, M.; Nakanishi, T.; Fushimi, K.; Hasegawa, Y. *ChemPlusChem* **2012**, 77, 277.

41. Miyata, K.; Konno, Y.; Nakanishi, T.; Kobayashi, A.; Kato, M.; Fushimi, K.; Hasegawa, Y. *Angew. Chem., Int. Ed.* **2013**, *52*, 6413-6416.

42. Semino, R.; Moreton, J. C.; Ramsahye, N. A.; Cohen, S. M.; Maurin, G. *Chem. Sci*. **2018**, *9*, 315.

43. Zhang, W.; Hu, Y.; Jiang, H.-L.; Yu, S.-H. *J. Am. Chem. Soc.* **2014**, *136*, 16978.

44. Myers, M.; Podolska, A.; Heath, C.; Baker, M. V.; Pejcic, B. *Analytica Chimica Acta* **2014**, *819*, 78.

45. Martínez-Martínez, V.; Furukawa, S.; Takashima, Y.; Arbeloa, I. L.; Kitagawa, S. *J. Phys. Chem. C* **2012**, 116, 26084.

46. Wang, X.-D.; Wolfbeis, O. S.; Meier, R. J. *Chem. Soc. Rev.* **2013**, *42*, 7834.

47. Cui, Y.; Zhu, F.; Chen, B.; Qian, G. *Chem. Commun.* **2015**, *51*, 7420.

48. Hatanaka, M.; Hirai, Y.; Kitagawa, Y.; Nakanishi, T.; Hasegawa, Y.; Morokuma, K. *Chem. Sci.* **2017**, *8*, 423.

Appendix I. Hetero Core-Shell Metal-Organic Frameworks

1 Introduction

Metal–organic Frameworks (MOFs), also known as porous coordination polymers (PCPs), are an emerging as a relatively new class of promising crystalline porous material[1]. The key features of MOFs are ultrahigh porosity and structural/functional tunability which captured considerable attention both scientists and engineers in the past two decades[2-5]. A great deal of research efforts have shown that MOFs are promising candidats for numerous applications such as gas storage[6,7], molecular separation[8-10], catalysis[11,12], sensing[13,14], and conduction[15,16]. Nevertheless, commercializing MOF is very difficult because individual MOF is very difficult to satisfy all the requirements for realistic applications, such as multifunction, hydro-stability, chemical stabitliy, reactivity, and working capacity.

Integration of various type of MOFs into one system, such as solid solution[17,18], janus type structure[19-21], and core-shell structure[22-30], can further escalate merits over individual MOF structures and create the new multifunctional composites. Unlike solid solutions or Janus type MOFs, which can usually exhibit the characters of individual MOFs at the same time, the core-shell MOFs have significant merits in synergy due to sequential molecule diffusion, energy transfer, and catalytic reaction, which stimulates various researches to expand scope of realistic applications. Kitagawa group reported the sequantial functianlized porous coordination polymer, $\{Zn_2(bdc)_2(dabco)\}_n@\{Zn_2(adc)_2(dabco)\}_n$ (bdc= 1,4-benzene dicarboxylate, adc=9,10-antracene dicarboxylate, and dabco= 1, 4-diazabicyclo[2.2.2]octane)[22]. $Zn_2(adc)_2(dabco)$ offers the selectivity that extracts the linear petroeum molecules from a mixture with its branched isomer and $Zn_2(bdc)_2(dabco)$ stores large amounts of separated molecules, simultaneously. Further, Rosi group reported bio-MOF-11@bio-MOF-14 for selective CO_2 capture with high water stabiltiy[23]. Small and hydrophobic pores of bio-MOF-14 protect bio-MOF-11 from hydrolysis and selectivly separate the CO_2 from CO_2/N_2 mixture. Further, this core-shell MOF could exhibit the larger CO_2 storage capacity than bio-MOF-14 because of highly porous bio-MOF-11. However, previous studies have been limited that MOF pairs for core-shell structure are usually isostructure having different metal ions or ligands. Very recently, Zhou group reported core-shell MOF with mismatching lattices under the guidance of nucleation kinetic analysis[24]. The shell is composed of polycrystalline MOF instead of single-crystalline MOF because nucleations of shell MOF have occurred in multiple directions on the core MOF surface. In this case, however, there is a problem that shell MOFs grow and merge with the neighboring shell resulting in a large number of defects from grain boundaries. Therfore, in order to maximize the advantages of the core-shell structure and to widen the practical applications through the MOF systems having multifuntional properties, studies on having single crystalline core-shell structure with hetero-structure MOF pairs are highly demanded.

Herein, we reports a single crystalline core-shell MOF composed of hetero-structure MOF pairs. HKUST-1 and MOF-5. Through the collaborative work with simulation team of professor Jihan Kim in KAIST, we have obtained various hetero-MOF pair candidates for core-shell structure by simulation and are proceeding synthesis based on the simulation results. In particular, we successfully synthesized the core-shell structure of HKUST-1 (composed of Cu^{2+} and 1,3,5-benzenetricarboxylate) and MOF-5 (composed of Zn^{2+} and terephthalate), two of the most representative MOFs. In addition, we are studying the key factors for synthesis of single crystalline core-shell MOF composed of hetero-structure MOF pairs based on simulation.

2 Experimental Section

Materials and characterization. All chemicals and solvents were of reagent grade and were used as received without further purification. XRPD patterns were collected on a Bruker D8 advance diffractometer at 40 kV and 40 mA for Cu Kα (λ = 1.54050 Å), with a step size of 0.02° in 2θ. Scanning electron microscope (SEM) images were taken using a Hitach High-Technologies Cold FE-SEM operating at 10 kV. The nitrogen adsorption-desorption isotherms were obtained using a BELSORP-max at 77 K. Prior to the adsorption measurements, all samples (~100 mg) were evacuated (p < 10-5 mbar) at 393 K for 5 h. The specific surface area was obtained by the Brunauer-Emmett-Teller (BET) method. Fourier-transform nuclear magnetic resonance (FT-NMR) spectra were recorded on an Agilent 400 MHz spectrometer.

Synthesis of MOFs

Synthesis of HKUST-1 with the size of ca. 10 um[31] : To an aqueous solution (15 mL) containing $Cu(NO_3)_2 \cdot 2.5H_2O$ (2.08 g, 8.6 mmol), the mixture solution of ethanol/dimethylformamide(1:1, v/v, 30 mL) containing trimesic acid (1.00 g, 4.76 mmol) was added, and stirred for 10 min. The resulting solution was divided into three equal parts and placed in an autoclave, heated to 100 ^oC for 30 min, and maintained for 24 h. The light blue powder was collected by centrifugation, washed 3 times with methanol and dimethylformamide, respectively.

Synthesis of HKUST-1 with the size of ca. 70 um : The aqueous solution (3 mL) containing $Cu(NO_3)_2 \cdot 2.5H_2O$ (0.163 g, 0.70 mmol) and the 3 mL of ethanol solution containing trimesic acid (0.147 g, 0.70 mmol) were sonicated for 20 min, respectively. To an aqueous Cu^{2+} solution, the ethanol solution containing ligand was added, stirred for 10 min, transferred to the autoclave, and kept for 24 h at 100 ^oC oven. The light blue powder was collected by centrifugation, washed 3 times with methanol and dimethylformamide, respectively.

Synthesis of HKUST-1 with the size of ca. 100-300 um : The aqueous solution (3 mL) containing $Cu(NO_3)_2 \cdot 2.5H_2O$ (0.161 g, 0.69 mmol) and the 3 mL of ethanol solution containing trimesic acid (0.105 g, 0.50 mmol) were sonicated for 20 min, respectively. To an aqueous Cu^{2+} solution, the ethanol solution containing ligand was added, stirred for 10 min, transferred to the autoclave, and kept for 24 h at 100 ^oC oven. The light blue powder was collected by centrifugation, washed 3 times with methanol and dimethylformamide, respectively.

Synthesis of HKUST-1@MOF-5 : Target amounts of HKUST-1 crystal were placed in glass jar and MOF-5 precursor solution with desired concentration was added. The mixture was placed at 100 oC

oven for target time. The resulting products was washed with anhydrous diethylformaide and anhydrdous CH_2Cl_2, and kept in anhydrous CH_2Cl_2.

3 Results and Discussions

Prior to the experiment synthesis of MOF pair that could have a hetero core-shell structure, the possible candidate pairs of hetero core-shell structure were selected by simulation from Professor Jihan Kim's group of KAIST. They use CoRE MOF database and selected candidate pairs through the algorism. Among them, HKUST-1 and MOF-5 pair is most fascinated because of small difference of cell parameter, commercially available precursors, and their mild synthetic condition (Figure 1).

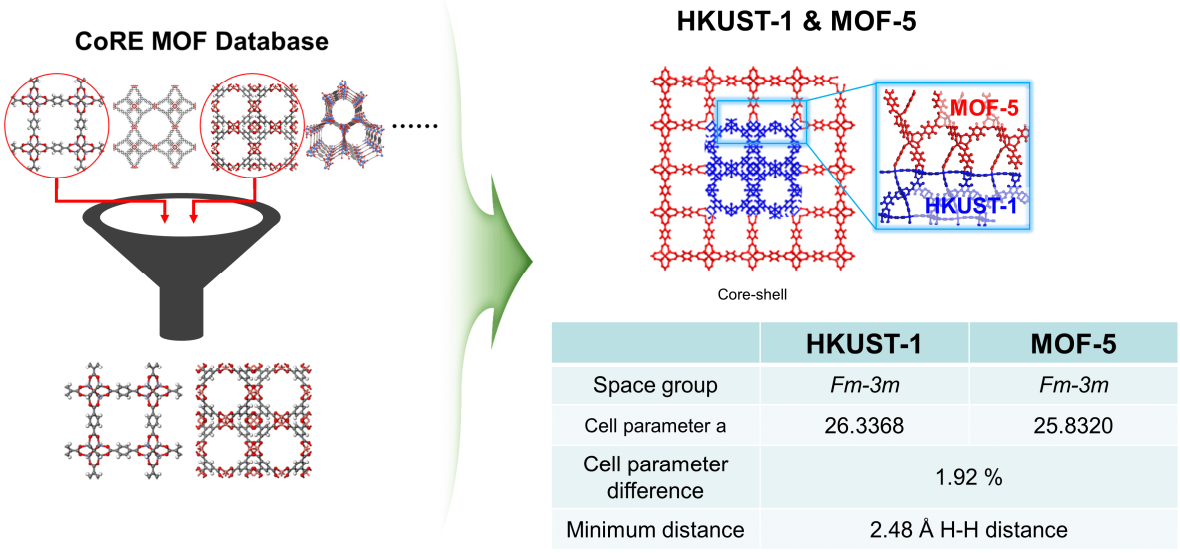

	HKUST-1	MOF-5
Space group	*Fm-3m*	*Fm-3m*
Cell parameter a	26.3368	25.8320
Cell parameter difference	1.92 %	
Minimum distance	2.48 Å H-H distance	

Figure 1 Simulation results of hetero core-shell structures from KAIST and cell parameter difference of HKUST-1 and MOF-5

The synthesis of the hetero core-shell structure of HKUST-1@MOF-5 was tested in various solvent systems, dimethylacetamide (DMA), dimethylformaide (DMF), and diethylformaide (DEF). 77 mg of HKUST-1 as core MOF were placed in the 20 mL MOF-5 precursor solution containing 0.051 M of Zn^{2+} and 0.038 M of BDC dissolved in various type of solvents (DMA, DMF, and DEF) and heated for 24 h at 100 oC. ^{1}H-NMR spectrum of DMA, DMF, and DEF products shows the mole ratios of BDC over BTC are 28%, 50%, and 38%, respectively, which confirmed the existence of BDC in products. The crystal morphology of products revealed by the optical microscopy and scanning electron microscopy images (Figure 2). In DMA, the new plate-like crystals are grown on the HKUST-1 surface. In DMF, transparent crystals estimated as MOF-5 were not seen, and SEM showed HKUST-1 crystals with smooth or small powder phases attached. Interestingly, in the DEF condition, the crystal structure seen as a core-shell in the microscope was occasionally observed, and the HKUST-1 surface on the

SEM image was mostly smooth. Further, PXRD patterns of products from DMA, DMF, and DEF compared with simulated patterns of HKUST-1 revealed that the only products from DEF show pure HKUST-1 and MOF-5 phase (Figure 3). Due to the impurity phases in products from DMA and DMF, they were excluded in further experiments.

Interestingly, in DEF products, only a few crystals of core-shell type were found and mostly greenish blue crystals in the microscope results, although the large amount of BDC (38% of the BTC) were included. This could be attributed to the fact that the thickness of the MOF-5 surrounding the small HKUST-1 crystal is too thin to be observed with a microscope. Therefore, in order to clearly confirm the formation of MOF-5, experiments were conducted to decrease the amount of HKUST-1 and to increase the crystal size of HKUST-1.

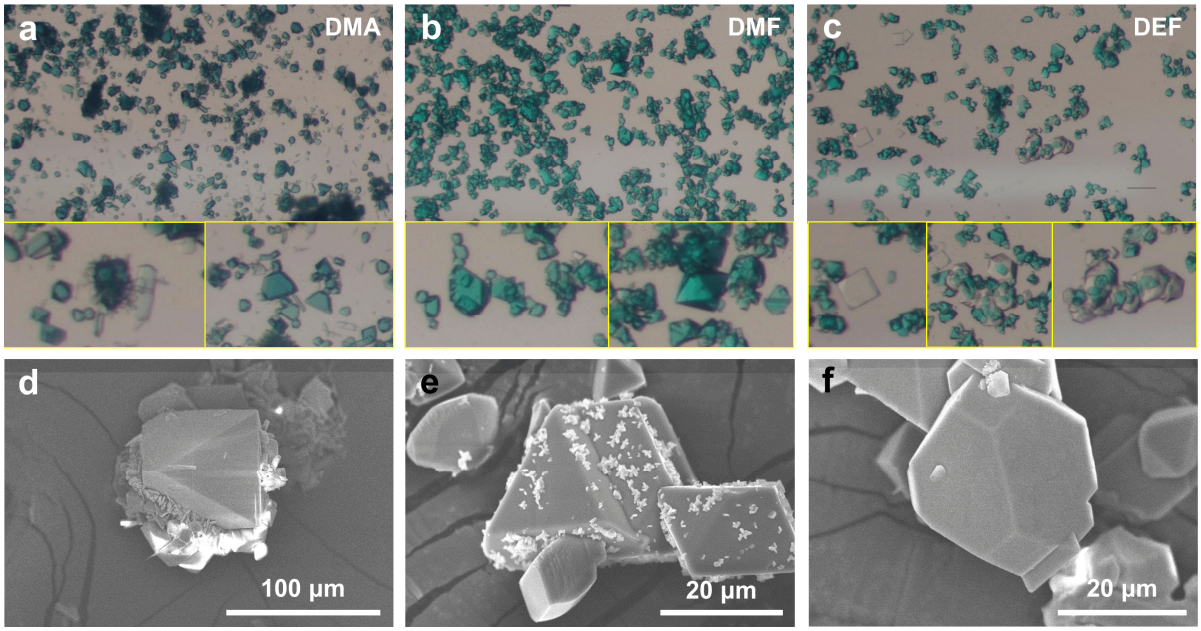

Figure 2 Optical microscope image of products synthesized in (a) DMA, (b) DMF, and (c) DEF. inset images are the enlargement image of products. SEM images of products synthesized in (d) DMA, (e) DMF, and (f) DEF.

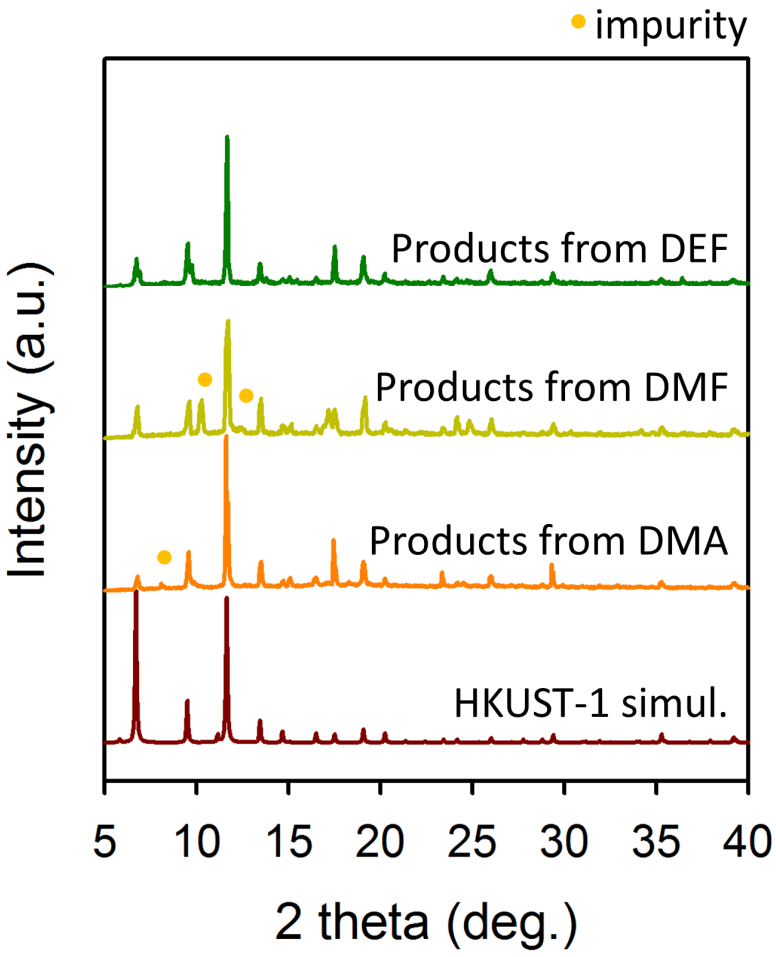

Figure 3 XPRD patterns of products from DMA, DMF, and DEF and compared with simulated patterns of HKUST-1. Yellow circle indicates the unknown crystalline phases.

First, the amount of HKUST-1 used in the core-shell synthesis was reduced from 77 mg to 20 and 2 mg. The optical images of products clearly showed that the ratio of core-shell morphology is increase as the amount of HKUST-1 used decreases (Figure 4). When 77 mg of HKUST-1 is used, most of products is greenish blue crystals and only some of them show a core-shell structure (Figure 4a). This is might be due to the thickness of MOF-5 shell which is too thin to observe in the optical microscope. In case of 20 mg of HKUST-1, the optical images show multi-core-shell structure (Figure 4b). This may be because the MOF-5 shell grows on the HKUST-1 crystal surface, which is densely placed on the bottom of the glass jar, and merges with the neighboring MOF-5 shell. When the amount of HKUST-1 crystals used was reduced to 2 mg which were sufficiently separated from each other, most of products show core-shell structure (Figure 4c).

Therefore, it has been confirmed that the distance between the HKUST-1 crystals is very important to form a core-shell structure.

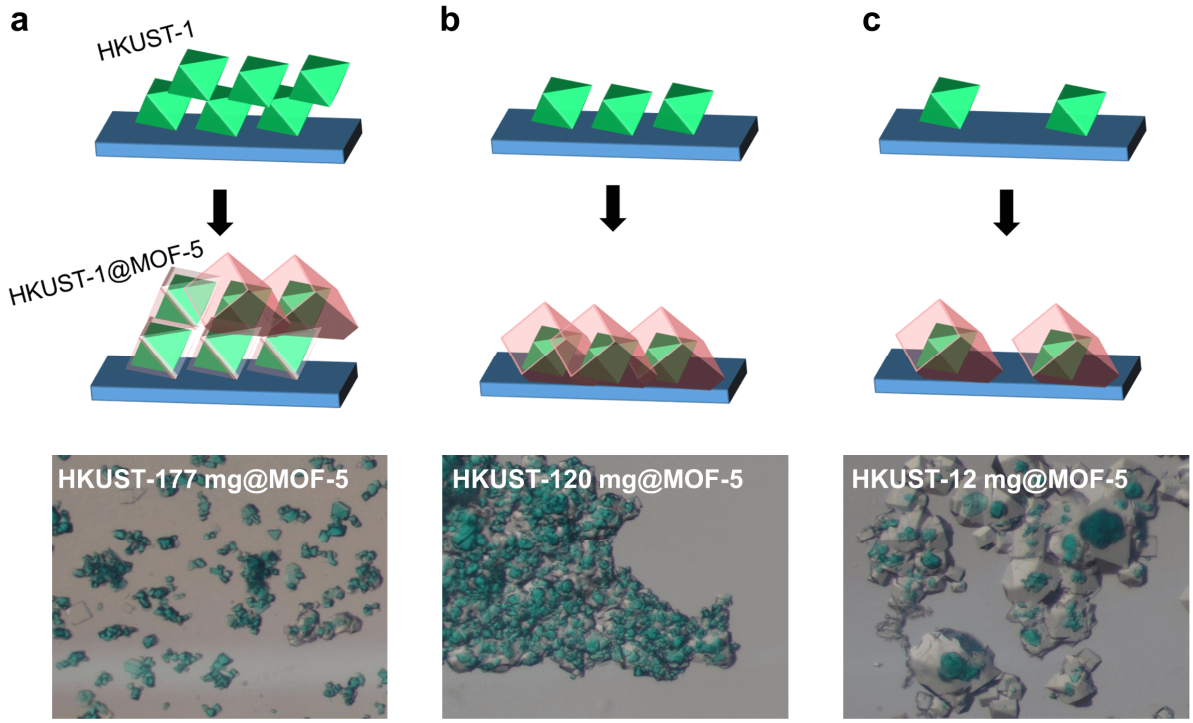

Figure 4 Schematic and optical microscope images of core-shell products synthesized using different amounts of HKUST-1 (core).

Having confirmed the effect of the distance between the HKUST-1 crystals, I then decided to examine the effects of MOF-5 synthetic conditions on the core-shell structure with the fixed amount of HKUST-1 (2 mg). When different amounts of MOF-5 precursor solution were used for core-shell synthesis with a fixed concentration (0.051 M of Zn^{2+} and 0.038 M of BDC), MOF-5 was difficult to grow on HKUST-1 surface in below 5 mL of the precursor solution and was synthesized in powder form (Figure 5a). This is because the smaller the amount of solvent, the faster the nucleation of MOF-5 is due to the faster heat transfer, resulting in the smaller the crystal appears to be. In case of controlling the concentration of precursor with the fixed solution volume of 20 mL, the concentration of Zn^{2+} was decreased from 0.051 M to 0.020 M and 0.0051 M while maintaining the ratio of BDC to Zn^{2+}. As shown in Figure 5b, it was confirmed that the MOF-5 was difficult to grow on the surface of HKUST-1.

In order for MOF-5 to grow on HKUST-1 surface, the precursor concentration and solvent volume of MOF-5 precursor solution are important.

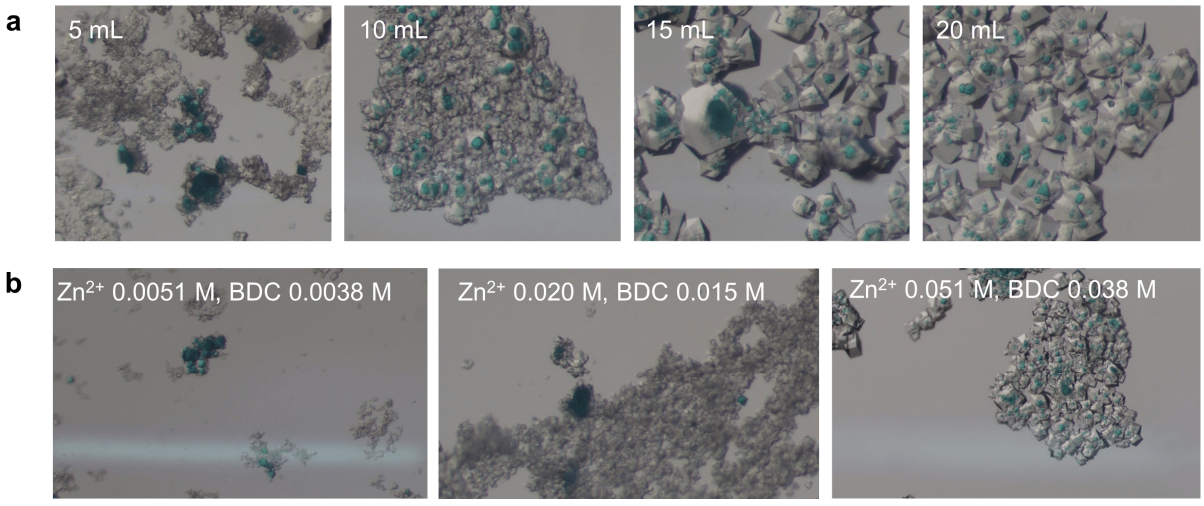

Figure 5 Optical microscope images of core-shell products synthesized from (a) different amount of 2nd MOF precursor solution and (b) different concentration of 20 mL of 2nd MOF precursor solutions.

The core-shell structure can be confirmed more clearly in optical microscope, if the crystal size of HKUST-1 is increased from 10 μm to 70 μm and 100-300 μm (Figure 6). In addition, the process of MOF-5 growth on the surface of HKUST-1 can be confirmed by optical microscopy according to the synthesis time (Figure 7). In microscopic images, the formation of the new crystal was not observed until 4 hours after the start of synthesis, but after 8 hours thin shell crystals were observed to grow following the shape of HKUST-1 surface. At 12 hours, in the case of small HKUST-1 crystals, the shell MOF no longer has the shape of the HKUST-1 crystal and grows into the cubic shape, the inherent crystal morphology of MOF-5. On the other hand, in the case of large HKUST-1 crystals, shell MOF were still growing along the HKUST-1 surface. After 16 hours, the shell MOFs on large HKUST-1 crystals were grown in cubic shape. At this time, MOF-5 crystals formed from homogeneous nucleation were observed, and the amounts of MOF-5 crystals was increased with increasing synthesis time.

In other words, heterogeneous nucleation of MOF-5 on HKUST-1 surface is more favorable than homogeneous nucleation of MOF-5, which is well understood by classical nucleation theory. Therefore, in the case of using HKUST-1 of 100-300 μm size, synthesizing time in the range of 12-16 hours was suitable for obtaining pure core-shell structure by minimizing the MOF-5 crystals grown from homogeneous nucleation. In addition, further investigation of the initial stage of nucleation of MOF-5 on HKUST-1 surface will be conducted through SEM measurement.

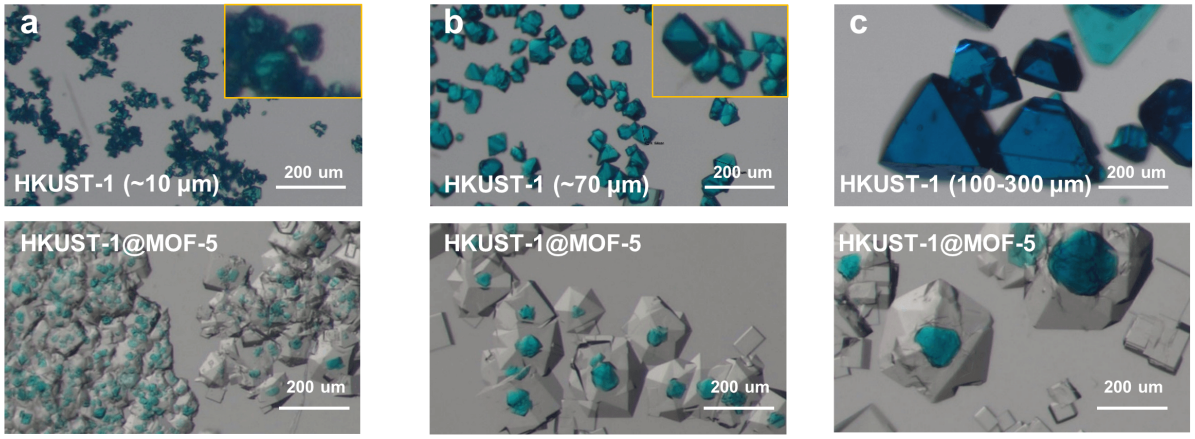

Figure 6 Optical microscope images of HKUST-1 with different size and corresponding core-shell crystals. The crystal sizes of HKUST-1 are (a) ca. 10μm, (b) ca. 70 μm, and (c) ca. 100-300 μm, respectively.

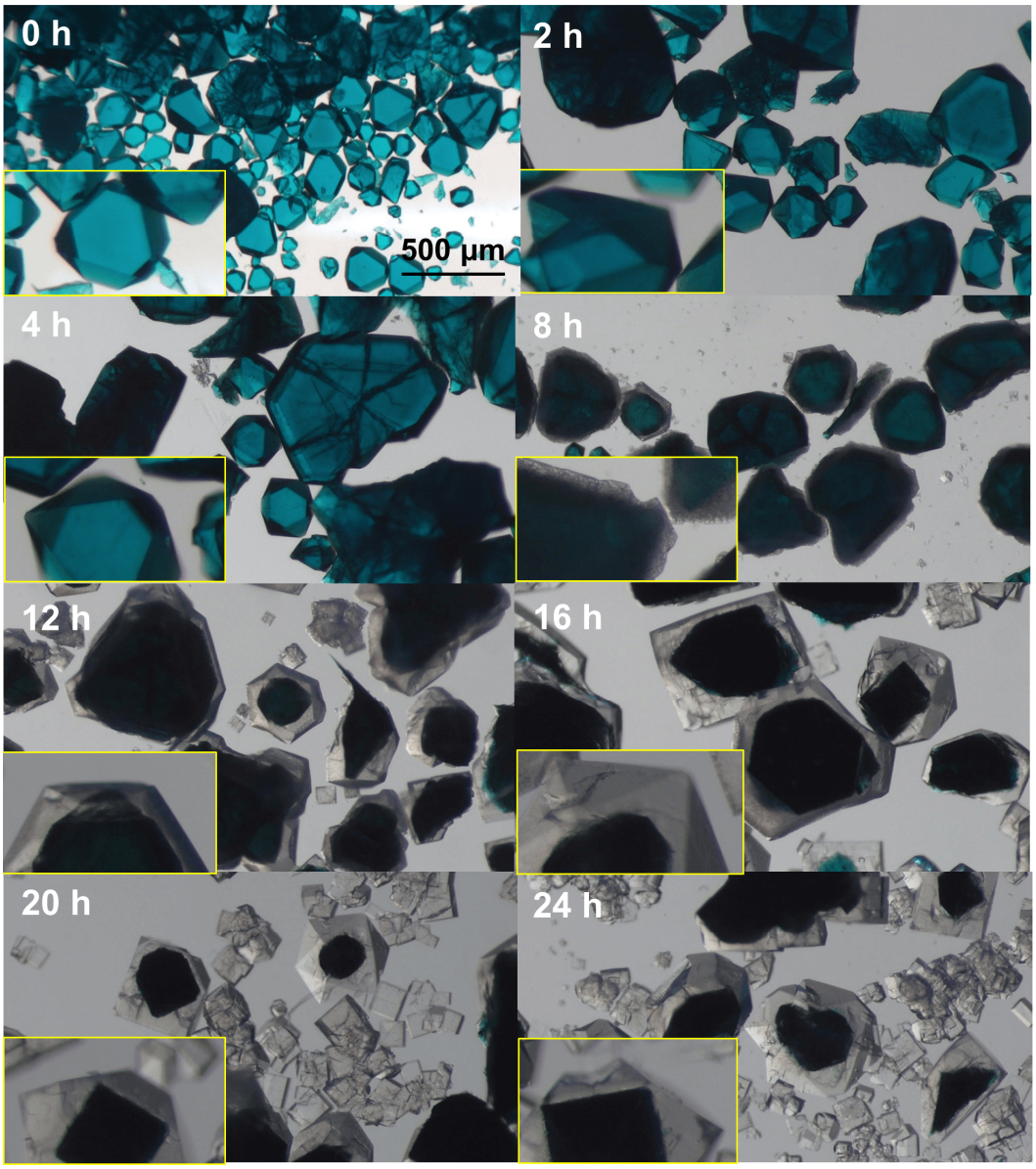

Figure 7 Optical images of HKUST-1@MOF-5 with different synthesis time (from 0 h to 24 h). Inset images are enlargement images of HKUST-1@MOF-5.

Interestingly, most of the synthesized core-shell structures were confirmed to have a single crystal of MOF-5 covering the HKUST-1 surface, with {111} planes of both HKUST-1 and MOF-5 facing up. The mechanism of formation of core-shell structure is suggested as in Figure 8a. First, most HKUST-1 crystals are aligned with the {111} planes being exposed upward due to the inherent characteristics of HKUST-1 crystal morphology. At this time, since the MOF-5 has similar crystal cell parameter with that of HKUST-1, MOF-5 grows epitaxially on the {111} planes HKUST-1 resulting the {111} planes upward. The figure 4.8b shows optical images of the core-shell crystals of HKUST-1@MOF-5 with the {111} and {100} planes facing upward, respectively, which clearly shows the epitaxial growth of MOF-5 on HKUST-1 surface.

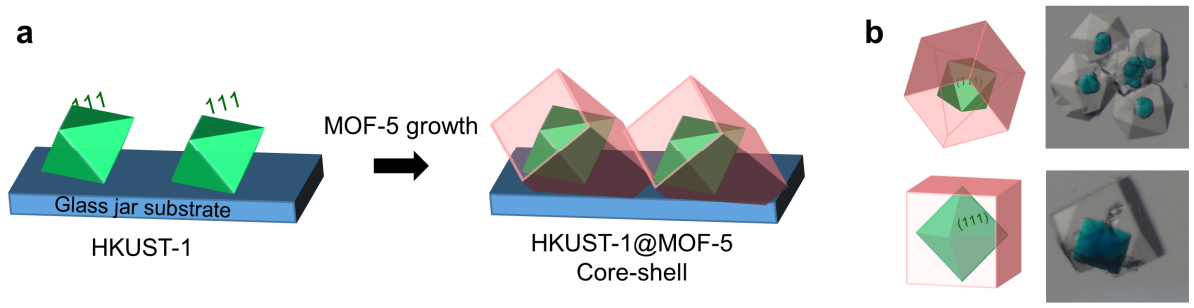

Figure 8 (a) Proposed mechanism in which (111) faces of MOF-5 grow upwards aligned on the surface of HKUST-1. (b) Schematic images of an epitaxially grown core-shell crystal structure and an optical microscope images of the corresponding core-shell crystal.

According to the simulation results of professor Jihan Kim's group in KAIST, there are two cases where MOF-5 can grow only in a specific direction on HKUST-1 surface (Figure 9). One is the case where the frameworks of HKUST-1 and MOF-5 are interpenetrated at the interface, and the other is the epitaxial growth of the MOF-5 framework at the dangling bond of HKUST-1 surface. Considering the crystal structure, diffusion of molecules into HKUST-1 is impossible because of the absence of pores in the case of interpenetration, and diffusion of molecules is possible because the interior pores are still connected when growing epitaxially.

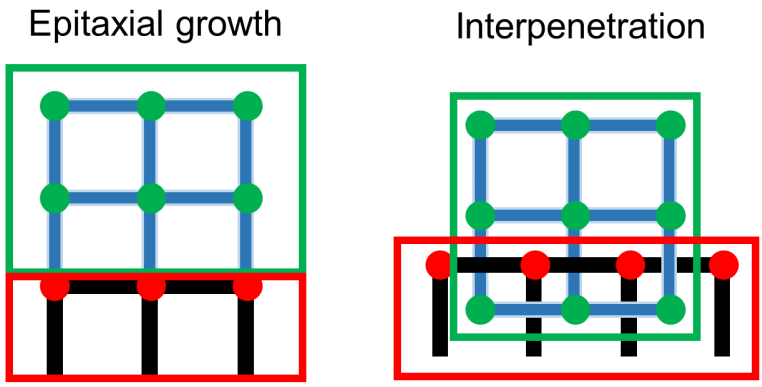

Figure 9 Schematic images of epitaxial growth and interpenetration.

The following series of experiments were conducted to confirm the interface structure between HKUST-1 and MOF-5. In case of DCM exchange test of as-synthesized core-shell crystal filled with DEF, the color of HKUST-1 crystals is clearly changed from greenish blue to dark blue, indicating diffusion of DCM molecules into the HKUST-1 (Figure 10). In the N_2 sorption isotherms, the surface area of the core-shell crystal is 2376 m^2/g which is close to the theoretical surface area (2568 m^2/g) of the epitaxially growing core-shell structure (Figure 11). In addition, when the core-shell structure was ground and the HKUST-1 core was exposed to the outside, the adsorption amount was 1907 m^2/g, which was slightly decreased due to the increase of defect. Thus, there are enough pores in the interface of the core-shell structure so that gas molecules can diffuse into HKUST-1.

The XRPD results and optical microscope images of new core-shell structure, replaced MOF-5 with IRMOF-18, having very similar cell parameter but composed of the ligand with the bulky tetra-methyl functional group, showed the successful synthesis of the HKUST-1@IRMOF-18 structure with covering the single crystal of IRMOF-18 on the whole surface of HKUST-1 (Figures 12 and 13). Due to the nature of the bulky ligand of IRMOF-18, it is impossible to form an interpenetration structure in the narrow HKUST-1 pore, suggesting that the interface structure of the core-shell is epitaxial.

In other words, through DCM exchanging, N_2 gas sorption isotherms, and synthesis of HKUST-1@IRMOF-18, epitaxial growth of MOF-5 on HKUST-1 surface was proved, indicating that there are enough pores to allow the molecule diffuse into HKUST-1.

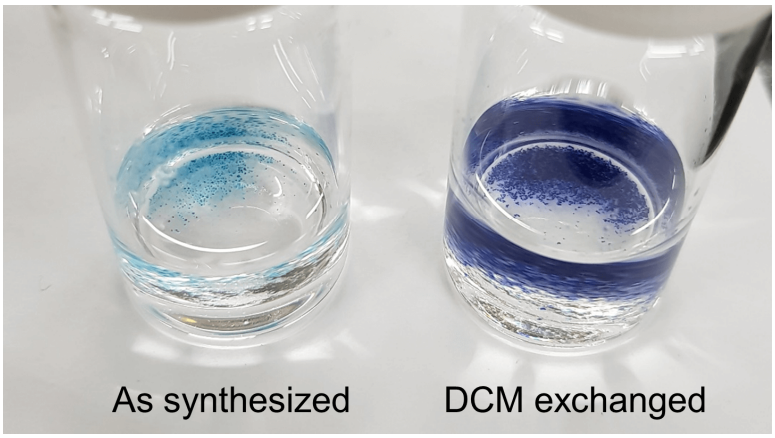

Figure 10 Photo image of as synthesized core-shell and DCM exchanged core-shell.

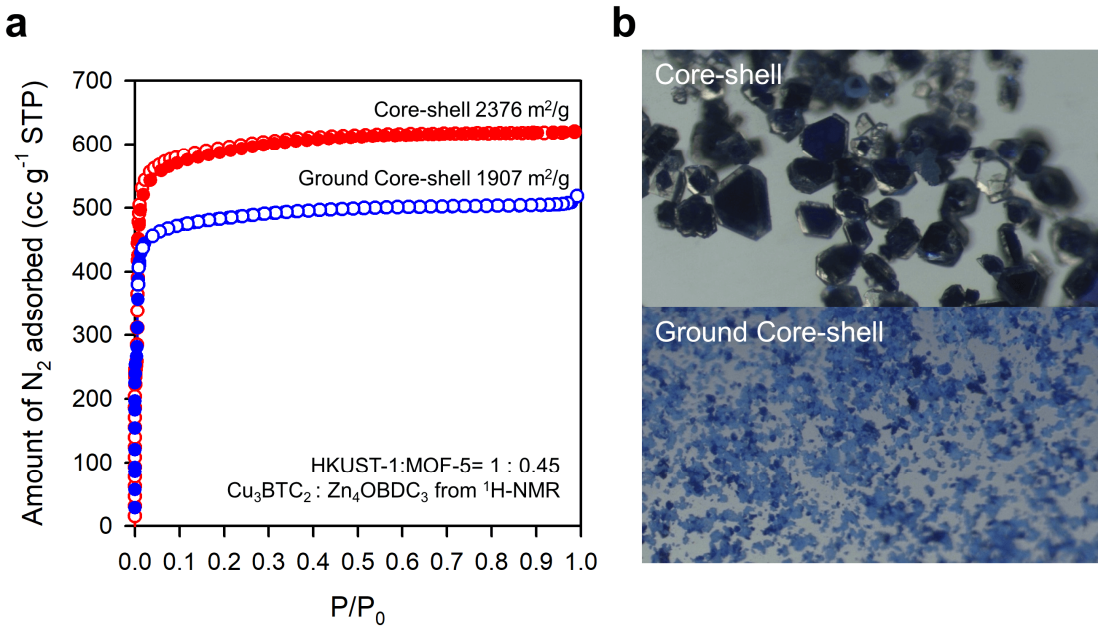

Figure 11 (a) N_2 sorption isotherms of core-shell and ground core-shell. (b) Optical microscope images of core-shell and ground core-shell crystals.

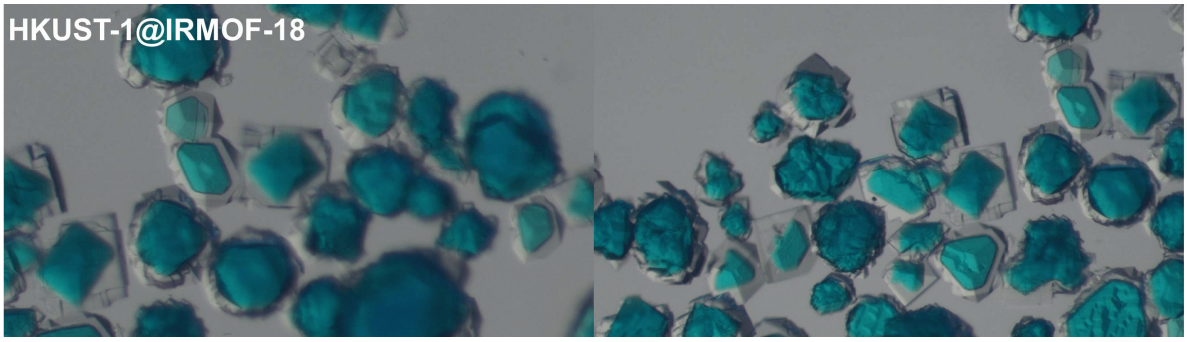

Figure 12 Optical images of HKUST-1@IRMOF-18.

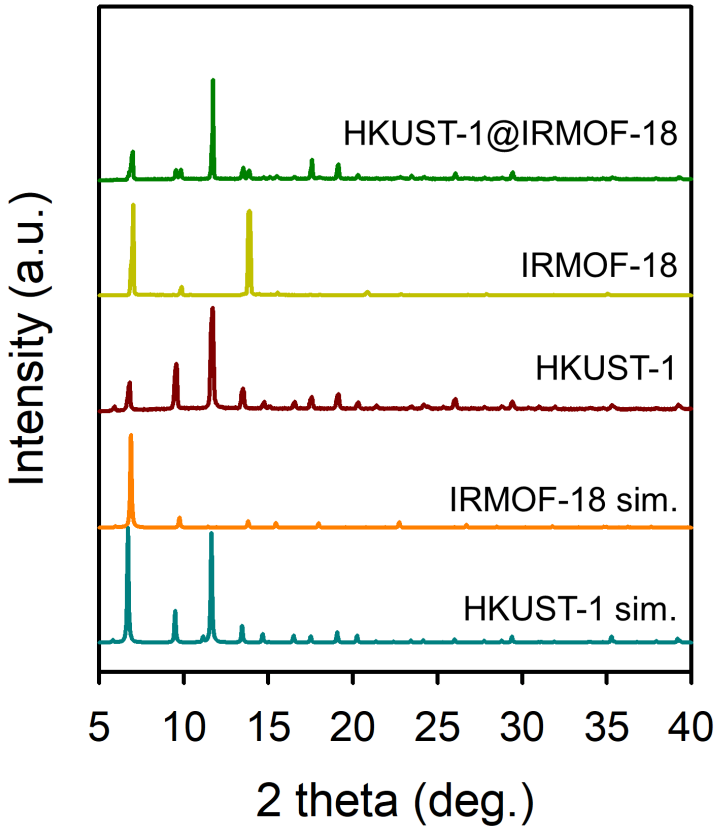

Figure 13 XPRD patterns of HKUST-1, IRMOF-18, HKUST-1@IRMOF-18 and compared with simulated patterns of HKUST-1 and IRMOF-18.

4 Conclusion

Previous core-shell MOF structure usually studied with MOF pairs having isostructure with the different metal ions or different ligands. Our new core-shell structure, HKUST-1@MOF-5, breaks the stereotype of core-shell studies and shows that a MOF pair that is a cell matching without isostructure can be made into a single crystalline core-shell structure. Very recently, Zhou group reported core-shell MOF with mismatching lattices under slow nucleation kinetics of shell MOF. However, the shell is composed of polycrystalline MOF instead of single-crystalline MOF because nucleations of shell MOF have occurred in multiple directions on the core MOF surface. The core-shell structure seems to have been able to be constructed without cell parameter matching, because relatively low-energy heteronucleation is preferred to homonucleation requiring high energy. In case of HKUST-1 @ MOF-5, on the contrary, a single crystalline core-shell structure can be obtained because cell parameter-matching occurs eventhough MOF-5 and HKUST-1 are not isostructure. This result further extends the available MOF pairs for single crystalline core-shell structure and is expected to provide a core-shell system with more functionality. Currently, we are working on the validation of the generalization of the core-shell structure in other MOF pairs and the early stages of shell synthesis.

5 References

1. Zhou, H.-C.; Long, J. R.; Yaghi, O. M. *Chem. Rev.* **2012**, *112*, 673.
2. Furukawa, H.; Cordova, K.; O'Keeffe, M.; Yaghi, O. M. *Science* **2013**, 341, 974.
3. Kitagawa, S.; Matsuda, R. *Coord. Chem. Rev.* **2007**, *251*, 2490.
4. Long, J. R.; Yaghi, O. M. *Chem. Soc. Rev.* **2009**, *38*, 1201.
5. Sanchez, C.; Shea, K. J.; Kitagawa S. *Chem. Soc. Rev.* **2011**, *40*, 453.
6. Suh, M. P.; Park, H. J.; Prasad, T. K.; Lim, D.-W. *Chem. Rev.* **2011**, *112*, 782.
7. He, Y.; Zhou, W.; Qian, G.; Chen, B. *Chem. Soc. Rev.* **2014**, *43*, 5657.
8. Sumida, K.; Rogow, D. L.; Mason, J. A.; McDonald, T. M.; Bloch, E. D.; Herm, Z. R.; Bae, T.-H.; Long, J. R. *Chem. Rev.* **2011**, *112*, 724
9. Li, J.-R.; Sculley, J.; Zhou, H.-C. *Chem. Rev.* **2011**, *112*, 869.
10. Qiu, S.; Xue, M.; Zhu, G. *Chem. Soc. Rev.* **2014**, *43*, 6116.
11. Yang, Q.; Xu, Q.; Jiang, H.-L.; *Chem. Soc. Rev.* **2017**, *46*, 4774.
12. Xiao, J.-D.; Shang, Q.; Xiong, Y.; Zhang, Q.; Luo, Y.; Yu, S.-H.; Jiang, H.-L.; *Angew. Chem., Int. Ed.* **2016**, *55*, 9389.
13. Kreno, L. E.; Leong, K.; Farha, O. K.; Allendorf, M.; Van Duyne, R. P.; Hupp, J. T. *Chem. Rev.* **2012**, *112*, 1105.
14. Yi, F.-Y.; Chen, D.; Wu, M.-K.; Han, L.; Jiang, H.-L. *ChemPlusChem.* **2016**, *81*, 675.
15. Sun, L.; Campbell, M. G.; Dincă, M. *Angew. Chem., Int. Ed.* **2016**, *55*, 3566.
16. Stavila, V.; Talin, A. A.; Allendorf, M. D.*Chem. Soc. Rev.* **2014**, *43*, 5994.
17. Kozachuk, O.; Meilikhov, M.; Yusenko, K.; Schneemann, A.; Jee, B.; Kuttatheyil, A. V.; Bertmer, M.;Sternemann, C.; Pöppl, A.; Fischer, R. A. *Eur. J. Inorg. Chem.* **2013**, 4546.
18. Fukushima, T.; Horike, S.; Kobayashi, H.; Tsujimoto, M.; isoda, S.; Foo, M. L.; Kubota, Y.; Takata, M.; Kitagawa, S. *J. Am. Chem. Soc.* **2012**, *134*, 13341.
19. Tan, T. T. Y.; Cham, J. T. M.; Reithofer, M. R.; Andy Hor, T. S.; Chin, J. M. *Chem. Commun.* **2014**, 50, 15175,

20. Yadnum, S.; Roche, J.; Lebraud, E.; Négrier, P.; Garrigue, P.; Bradshaw, D.; Warakulwit, C.; Limtrakul, J.; Kuhn, A. *Angew. Chem., Int. Ed.* **2014**, *53*, 4001.

21. Ayala, A.; Carbonell, C.; Imaz, I.; Maspoch, D. *Chem. Commun.*, 2016, **52**, 5096

22. Hirai, K.; Furukawa, S.; Kondo, M.; Uehara, H.; Sakata, O.; Kitagawa, S. *Angew. Chem., Int. Ed.* **2011**, 50,8057

23. Li, T.; Sullivan, J. E.; Rosi, N. L. *J. Am. Chem. Soc.* **2013**, 135, 9984.

24. Yang, X.; Yuan, S.; Zou, L.; Drake, H.; Zhang, Y.; Qin, J.; Alsalme, A.; Zhou, H.-C. *Angew. Chem., Int. Ed.* **2018**, *57*, 3927

25. Koh, K.; Wong-Foy, A., G.; Matzger, A. J. *Chem. Commun.*, **2009**, 6162.

26. Heinke, L.; Cakici, M.; Dommaschk, M.; Grosjean, S.; Herges, R.; Bräse, S.; Wöll, C. *ACS Nano* **2014**, *8*, 1463.

27. Furukawa, S.; Hirai, K.; Nakagawa, K.; Takashima, Y.; Matsuda, R.; Tsuruoka, T.; Kondo, M.; Haruki, R.;Tanaka, D.; Sakamoto, H.; Shimomura, S.; Sakata, O.; Kitagawa, S. *Angew. Chem., Int. Ed.* **2009**, *48*, 1766

28. Ji, H.; Lee, S.; Park, J.; Kim T.; Choi, S.; Oh, M. *Inorg. Chem.* **2018**, *57*, 9048.

29. Furukawa, S.; Hirai, K.; Takashima, Y.; Nakagawa, K.; Kondo, M.; Tsuruoka, T.; Sakata, O.; Kitagawa, S.*Chem. Commun.* **2009**, 5097

30. Lee, H. J.; Cho, Y. J.; Cho, W.; Oh, M. *ACS Nano* **2012**, *7*, 491.

31. Yang, Y.; Shukla, P.; Wang, S.; Rudolph, V.; Chen, X.-M.; Zhu, Z. *RSC Adv.* **2013**, 3, 17065.

Acknowledgments

It has been 10 years since I came to UNIST with the dream of being a scientist. The 10-year life at UNIST was a time to be confident that I could do well even if it is difficult to go the way of the scientist because I like doing research. I would not have had such a wonderful experience if there were no thankful people for helping me.

First and foremost, I would like to express the deepest appreciation to my advisor and long time tearcher during my years at UNIST, Prof. Hoi Ri Moon for her constant assistance and enthusiastic encouragement thourghout the my Ph.D research. Without her insightful guidance and constructive comments, this thesis would not have been possible. I could not have imagined having a better advisor and mentor than her for my Ph.D study.

Besides my advisor, I would like to express my sincere appreciation to the rest of my thesis committee: Prof. Hyunchul Oh, Prof. Myoung Soo Lah, Prof. Jong-Beom Baek, and Prof. Nak Cheon Jeong, for their valuable comments and encouragement, but also for the hard question which incented me to widen my research from various perspectives. Specially, I would like to deeply grateful to Prof. Hyunchul Oh, who has given me lots of advice and wonderful collaboration to keep my dreams in difficult times.

I thank my friends and lab mates, especially Kyung Joo Lee, Ji Yun Kim, Sung-min Hyun, Jea Hwa Lee, and Sungeun Jeoung, in for the stimulating discussions, for the sleepless nights we were working together before deadlines, and for all the fun we have had in UNIST life. I would also like to extend my thanks to the wonderful Team leader and Staffs of the UNIST Central Research Facilities (UCRF), in particular Young-ki Kim, Ji-hye Park, Mi sun Cho, and Eun-jung Han, not only for their professional helps as well as warm attention to students. I will never forget their kindness, which has been a great force in overcoming my slump.

Last but not the least, I would like to thank my family and my my soul mate, Moohyeon Nam, for supporting me spiritually throughout writing this thesis and my my life in general.

I would like to thank all of you who have helped me with my research. Lastly, I would like to mention the one Nobel Prize winner’s answer to the motivation for his endless research, which has greatly helped to my graduate life. “Frankly speaking, my research life was not always a golden age, and sometimes I was under tremendous stress. But NEVER BORED.”